UCGE Reports
Number 20218

Department of Geomatics Engineering

The Impact of Future Global Navigation Satellite Systems on Precise Carrier Phase Positioning

(URL: http://www.geomatics.ucalgary.ca/links/GradTheses.html)

by

Todd Richert

May 2005

UNIVERSITY OF CALGARY

The Impact of Future Global Navigation Satellite Systems on Precise Carrier Phase Positioning

by

Todd Richert

A THESIS

SUBMITTED TO THE FACULTY OF GRADUATE STUDIES

IN PARTIAL FULFILMENT OF THE REQUIREMENTS FOR THE

DEGREE OF MASTER OF SCIENCE

GEOMATICS ENGINEERING DEPARTMENT

CALGARY, ALBERTA

MAY, 2005

Abstract

This thesis is an investigation of the performance that can be expected from future global navigation satellite systems (GNSS). The next decade promises drastic improvements and additions to existing satellite navigation infrastructure. Plans for GPS modernization include a civilian code measurement on the L2 frequency and a new L5 signal at 1176.45 MHz. Current speculations indicate that a fully operational constellation with these improvements could be available by 2013 (Hothem, 2004). Simultaneously, the Galileo Joint Undertaking is in the development and validation stages of introducing a parallel GNSS called Galileo. Galileo will also transmit freely available satellite navigation signals on three frequencies and is scheduled to be fully operational as early as 2008 (Wibberley, 2004).

In response to these momentous changes, this research investigates the impact that the new signals will have on precise kinematic positioning. Effective techniques for processing future GNSS measurements are presented and a thorough treatment of the measurement correlations and processing strategies is given. These strategies have been implemented in a newly developed software simulation package that both simulates future GNSS signals and processes these simulated measurements.

The simulation software is used to analyze and demonstrate the ability to estimate ionospheric delays using future GNSS measurements. It is found that the more precise Galileo code measurements and the enhanced geometry of a combined GPS/Galileo

system greatly improve the ability to estimate ionospheric delays quickly and precisely. The improved ability to estimate ionospheric delays is then propagated into an evaluation of ambiguity resolution performance with future GNSS signals. A combined GPS/Galileo system was found to perform significantly better than currently available systems in terms of speed of ambiguity resolution and the ability to successfully validate the correct ambiguity set.

Finally, a survey of the various linear combinations of carrier phase data that will be available with future GNSS signals is carried out. After developing the fundamental theory behind combining GNSS measurements, several combinations are shown to enable superior ambiguity resolution and reduce the effects of thermal noise, multipath and ionospheric errors. It is also demonstrated that an *optimal* choice of linear combinations is highly dependent on the baseline length, observational time span, and requirements of a given mission.

Acknowledgements

I would like to thank my supervisor, Dr. Naser El-Sheimy, for his support and guidance throughout this journey. I have benefited from his exceptional ability to give me the freedom to wander and the guidance to keep me on track. I greatly appreciate the way he has genuinely looked out for my interests.

Thanks go to Dr. Darren Cosandier from Waypoint Consulting Inc. His insight and confidence in me was a source of motivation. I would also like to thank Janet Neumann from NovAtel Inc. for her understanding in giving me the time I needed to finish this thesis.

Financially, I would like to acknowledge the generous support of the Natural Sciences and Engineering Research Council of Canada, the Alberta Ingenuity Fund, Waypoint Consulting Inc., and the University of Calgary Geomatics Engineering Department.

Finally, I thank my friends and family who may not understand what I have been doing, but have nevertheless supported and encouraged me consistently.

Table of Contents

List of Tables

List of Figures and Illustrations

List of Symbols

$\hat{a}, \breve{a}$	vectors of float and fixed untransformed ambiguities
a, b, c	combination coefficients
B	transformation matrix or double differencing matrix
c	speed of light in a vacuum in metres per second (299792458 m/s)
dI_A^i	transmission delay or advance due to the effect of the ionosphere in metres
dT_A^{GPS}, dT_A^{GAL}	clock offset between receiver clock A and GPS Time and GST, respectively in metres
dt_{GPS}^i, dt_{GAL}^i	clock offset between satellite clock, i and GPS Time and GST, respectively in metres
dTr_A^i	transmission delay due to the effect of the neutral atmosphere in metres
$d\rho_A^i$	orbital error projected onto the line of sight between the receiver and satellite in metres
$E(\cdot)$	expectation operator
f	frequency
$F_\alpha(\nu_1, \nu_2)$	Fisher distribution with significance level α and degrees of freedom ν_1 and ν_2
H	design matrix with respect to the unknown parameters
K	potential set of integer ambiguities
m	the number of ambiguities

$m(\cdot)$	mapping function
n	the number of observations
$\mathbf{n}$	normal vector
N_A^i	initial carrier phase ambiguity in cycles
$\hat{N}$	real-valued estimated ambiguity
$\breve{N}$	integer-valued estimated ambiguity
P_A^i	pseudorange measurement received at receiver A from satellite i scaled to metres
$P_{k/k}$	updated state variance-covariance matrix at epoch k
$P_{k/k+1}$	predicted state variance-covariance matrix for epoch k+1
Q_k	process noise matrix
Q_a, Q_z	covariance matrices corresponding to the transformed and untransformed ambiguity vectors
r_{sat}	position vector of a satellite in an Earth-centred, Earth-fixed reference frame
R	measurement variance-covariance matrix
t	the number of non-ambiguity parameters (position states, ionosphere states, etc.)
v	residual vector
x	vector of unknown parameters
z	vector of measurements
$\hat{z}, \breve{z}$	vectors of float and fixed transformed ambiguities

Z	LAMBDA transformation matrix
Δ	single difference operator (between receivers)
Δt	time difference
ε	vector of measurement noise or elevation angle in degrees
λ	wavelength of the carrier signal in metres
ρ_A^i	geometric range from receiver A to satellite i in metres
σ^2, σ	variance and covariance
ϕ_A^i	carrier phase measurement received at receiver A from satellite i in cycles
Φ_A^i	carrier phase measurement received at receiver A from satellite i scaled to metres
Φ_k	state transition matrix at epoch k
ω_k	system noise vector
Ω	the weighted sum of squared residuals
$\nabla\Delta$	double difference operator
$\otimes$	Kroneker product

List of Acronyms

AIUB	Astronomisches Institut der Universität Bern (Astronomical Institute of the Univerisity of Bern)
ARNS	Aeronautical Radio Navigation Service
CIR	Cascade Integer Resolution
CODE	Center for Orbit Determination in Europe
FAA	Federal Aviation Administration
FDMA	Frequency Division Multiple Access
GGTO	GPS-Galileo Time Offset
GLONASS	Global Navigation Satellite System (Russian)
GNSS	Global Navigation Satellite System
GPS	Global Positioning System (USA)
GST	Galileo System Time
GTRF	Galileo Terrestrial Reference Frame
IERS	International Earth Rotation Service
IGS	International GPS Service
ITRS	International Terrestrial Reference System
LAMBDA	Least Squares Ambiguity Decorrelation Adjustment
NAVSTAR	Navigation System with Timing and Ranging
RMS	Root Mean Square
SF	Scale Factor Matrix

SV	Satellite Vehicle
SYM	Symmetrical
TAI	International Atomic Time
TCAR	Triple Carrier Ambiguity Resolution
TEC	Total Electron Content
TECU	Total Electron Content Units (10^{16} electrons per square meter)
USNO	US Naval Observatory
UTC	Universal Time Coordinated
WGS-84	World Geodetic System (1984)

Chapter One: Introduction

Satellite navigation has become commonplace in many aspects of everyday life. It is used for navigation in cellular telephones, cars, boats, and airplanes, for precise positioning in surveying, monitoring structures and the crust of the Earth, and for transferring precise time for banking transactions and a myriad of other scientific applications. The applications seem to be limited only by our imaginations.

The two currently available global navigation satellite systems (GNSS) are the Russian Federation Global Navigation Satellite System (GLONASS) and the United States system, NAVSTAR (Navigation System with Timing and Ranging) Global Positioning System (GPS). GLONASS has been plagued with financial hardships that have prevented it from emerging into a reliable stand-alone system. GPS on the other hand has blossomed into a reliable system for free worldwide navigation and positioning.

The US NAVSTAR Global Positioning System (GPS) was first conceived when the US Department of Defence approved its basic architecture in 1973. The system was declared fully operational in 1995 (Global Positioning System, 2001) and since that time, only minor improvements and maintenance have kept the system in excellent reliable working condition. GPS was originally designed as a military system to give the US an advantage over its adversaries in a theatre of war by enabling only authorized military personnel to

access the full capacity of its services. With the turn of the 21st century, satellite positioning capabilities have become a crucial part of civilian industry and commercial users were apprehensive about relying heavily on a predominantly military system. In response to commercial industrial pressure, GPS has committed to cater more to its growing population of civilian users as evidenced by the recent US presidential directive on satellite-based positioning, navigation and timing policy (OSTP, 2004).

In the meantime, the European satellite navigation system Galileo has also been spawned to reduce the reliance of European industry on a US military system. The next decade promises momentous and exciting changes for developers and users of global navigation satellite system (GNSS) technology.

1.1 Future Plans for GNSS

The NAVSTAR GPS Joint Program Office is modernizing the currently available GPS by launching the first of the Block IIR-M satellites in 2005. This block of satellites will attain full operational capacity by 2010 and will broadcast the new civilian code on the L2 frequency band. In addition, the first of the Block IIF satellites will be launched in 2006 and full operational capacity for this block of satellites is expected by 2013 (Hothem, 2004). The Block IIF satellites will transmit on three frequencies providing

civil users with access to three pseudorange measurements and three distinct carrier signals.

The two new civilian pseudorange measurements will be the L2C code, which is modulated on the L2 carrier signal and the L5 civil code, which will be modulated on the new L5 carrier signal. These two modernized signals will have superior capabilities to the currently available GPS L1 and L2 signals. The primary advantage of the L2C code is that it will enable high precision users to acquire the L2 signal directly rather than performing fragile semi-codeless tracking techniques (Fontana, 2001). This will enable very robust L2 tracking capabilities with a significant improvement in the strength of the acquired signal. In addition, the longer code length of the L2C code will greatly mitigate signal cross-correlation, which will benefit applications in suboptimal environmental conditions such as indoors, under forest canopies, and in urban canyons (Cross, 2003). The civil L5 code will also exhibit these advantages, but will also be within the reserved Aeronautical Radio Navigation Service (ARNS) bandwidth which is advantageous for aeronautical users since it will not be subject to unacceptable interference from other radiolocation services like radar (McDonald, 2002).

In addition to future GPS modernization plans, the Galileo Joint Undertaking, which is a cooperative effort of public and private European investors, has committed to developing a parallel global positioning system called Galileo. Like modernized GPS, Galileo will

also transmit freely available signals on three frequencies with pseudorange codes modulated on each frequency. Galileo will offer five different services to accommodate the needs of various users (Ehm, 2004):

1. **Open Service (OS)** for mass market users such as cellular telephone, personal digital assistants (PDA's) and vehicle and pedestrian navigation
2. **Safety of Life (SoL)** for users requiring guaranteed integrity such as CAT-1 aircraft landing, train guiding and marine applications
3. **Commercial Service (CS)** for professional users who are willing to pay a user fee for access to additional encrypted ranging codes and data
4. **Search and Rescue Service (SAR)** with a capability to relay distress messages to a central processing center
5. **Public Regulated Service (PRS)** for authorized public or strategic applications requiring a high level of continuity such as police, telecommunications networks and emergency services

The signals and services offered by Galileo are shown in Figure 1.1.

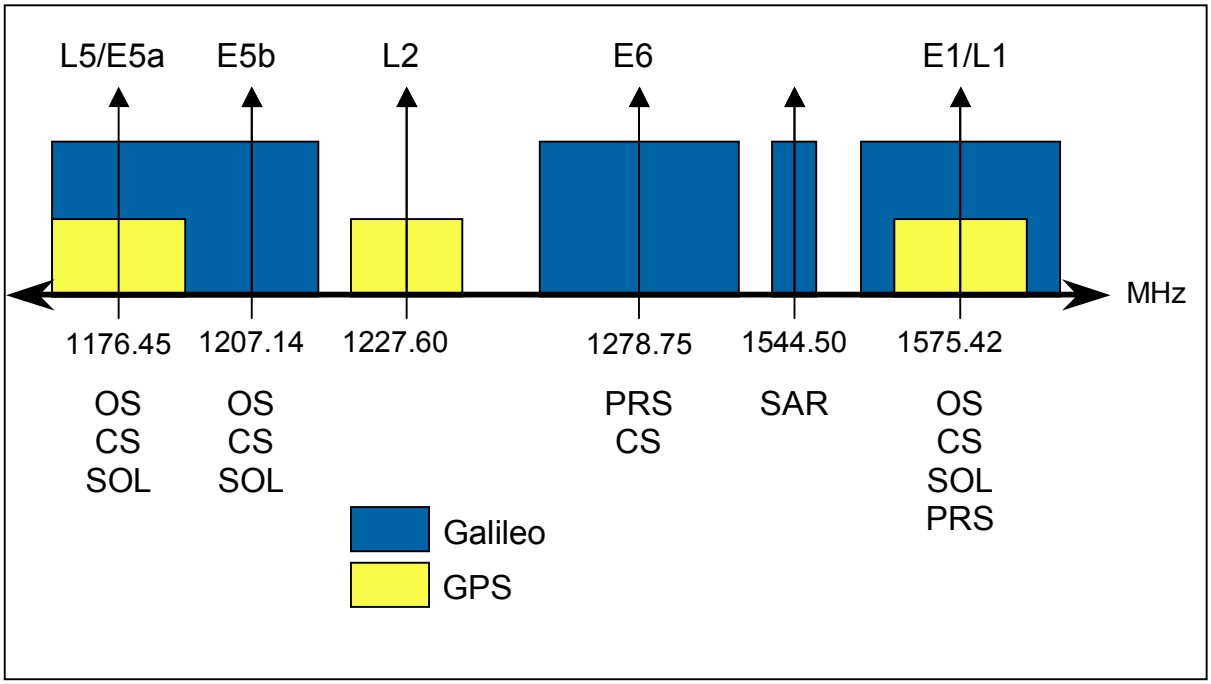

Figure 1.1: Galileo Signal Structure and Services (after Hein et al. 2002)

The Galileo project is currently in the development and in-orbit validation stage and the first launches for in-orbit validation are scheduled for 2005. The deployment stage is expected to commence in 2006 with full operational capacity scheduled for 2008 (Wibberley, 2004).

In light of the plans to modernize GPS and to deploy the Galileo system, there is great interest in using the two systems in an integrated manner. Upon extensive talks and deliberation, developers of GPS and Galileo have made certain strategic decisions that will allow the systems to be used together, but still maintain autonomy (European

Commission, 2004). For example, it was decided that the L1/E1 (1575.42 MHz) and L5/E5a (1176.45 MHz) frequency bands will be shared. This will allow the systems to be used together because receiver manufacturers will be able to use the same receiver front-ends for multiple signals. This will keep the cost of future dual-system receivers economically viable. However, the systems will remain autonomous by keeping the GPS and Galileo control segments completely separate.

Because of the separate system control segments, the coordinate reference frames for GPS and Galileo will be different. GPS uses the WGS-84 (World Geodetic System, 1984) coordinate reference frame and Galileo will use the Galileo Terrestrial Reference Frame (GTRF). While these reference frames are different in practice, they are both realizations of the International Terrestrial Reference System (ITRS) defined by the International Earth Rotation Service (IERS) and are expected to agree at the centimetre level. Consequently, these systems can be used interchangeably for most applications (Hein et al. 2002).

The designers of GPS and Galileo have also adopted different system timing schemes. GPS Time is steered to Universal Time Coordinated as maintained by the US Naval Observatory (UTC(USNO)) and offset by whole seconds; while Galileo System Time (GST) is steered to International Atomic Time (TAI). There will be an offset between these two time scales, which has to be considered when integrating GPS and Galileo.

This offset will be computed in the Galileo ground reference system and broadcast to the user in near real-time. Alternatively, the time offset could be solved for or eliminated by spending one satellite in a dual-system processor (Hein et al. 2002). These techniques will be discussed in further detail in Chapter Two.

For users of GNSS positioning technology, the implications of GPS modernization and the new Galileo system are substantial. Using a combination of the future systems will provide both improved satellite geometry and additional carrier phase measurements.

With full constellations of GPS and Galileo satellites, the total number of navigation satellites orbiting the Earth will effectively double causing enormous geometry improvements for any application. This impact will be most appreciated in those applications where sufficient visible satellites are often lacking such as in pedestrian and vehicle navigation in urban canyons and surveying under tree canopies or near large obstacles. O'Keefe (2001), Lachapelle (2001), and Verhagen (2002) are among some of the researchers that have conducted studies to quantify and simulate the benefits in reliability and availability of these additional satellites.

For precise GNSS positioning applications, there will be significant benefits to having six freely available carrier phase measurements. When used properly, these additional

signals have the potential to improve the speed and reliability of ambiguity resolution (Tiberius, 2002 and Alves, 2001).

The future of satellite navigation is changing rapidly and developers of GNSS equipment and software must keep up with the current changes in infrastructure. Satellite positioning technology is becoming more widespread and indispensable with each passing year. In 2001, the satellite navigation industry had a global turnover of 15 billion Euros (20 billion USD) and it has been predicted that this number will rise to 140 billion Euros (186 billion USD) by 2014 (Directorate-General for Energy and Transport, 2003). These momentous changes in GNSS infrastructure and industry have motivated the development of this thesis.

1.2 Problem Statement

Considering the upcoming major changes in GNSS infrastructure, the stakeholders in the precise GNSS positioning market do not know how reliable or how accurate future satellite-based positioning will be. In addition, developers are unsure of the optimal way to exploit the new signals that will become available in the next several years.

1.3 Major Objectives of the Thesis

The major objective of this thesis is to provide developers of future precise kinematic GNSS positioning systems with a quantitative and realistic analysis of the performance that can be expected when using both modernized GPS and Galileo.

In order to achieve this major objective, the following minor objectives will be accomplished:

1. To describe and demonstrate effective processing techniques for GNSS data from multiple systems and on multiple frequencies;
2. To show the impact that future GNSS signals will have on the ability to estimate ionospheric delays;
3. To provide a realistic and quantitative analysis of the reliability of ambiguity resolution with future GNSS signals;
4. To elucidate the benefits of using linear combinations of GNSS data and to test various optimally chosen combinations;
5. To develop simulation software for generating and processing future GNSS measurements.

1.4 Outline of Thesis

This thesis began with a review of the status of the currently existing global navigation satellite systems and the plans for future development. The background information given in Chapter One provides the foundation upon which the remainder of the thesis has been built.

Chapter Two accomplishes the first minor objective of the thesis by describing the functional and stochastic components of the measurement model and the dynamic model that have been implemented to process future GNSS signals. The observation equations are introduced and the technique used to estimate the unknown parameters is described. In addition, a thorough treatment of the inherent correlations between future GNSS measurements is presented.

Chapter Three describes the simulator and processing software that has been used in this research to generate and process futuristic GNSS measurements. The simulator is shown to generate realistic levels of all relevant error sources and to capture the performance of GNSS pseudorange and carrier phase measurements that will be available under GPS modernization and the development of Galileo. The accomplishment of the fifth minor objective of the thesis is described in Chapter Three.

Chapter Four discusses the effect of ionospheric errors on future GNSS positioning. Estimating the ionospheric errors as states is shown to be an effective technique to mitigate the effect of ionospheric errors. The improvement in the accuracy and convergence time of ionospheric estimation using future measurements is explained and demonstrated. The second minor objective of the thesis is accomplished in Chapter Four.

Chapter Five uses the simulated measurements described in Chapter Two, the mathematical models portrayed in Chapter Three, and the ionospheric estimation techniques of Chapter Four to provide quantitative results of ambiguity resolution with future GNSS signals. The expected success of integer ambiguity searching and ambiguity validation using simulated future GNSS measurements is demonstrated. The third minor objective of the thesis is accomplished in Chapter Five.

Chapter Six describes the mathematical theory involved in using linear combinations of carrier phase data. Linear combinations that mitigate or eliminate the effects of the individual GNSS error sources are explained. Finally, using the simulated measurements described in Chapter Three and the processing techniques of Chapter Two, some optimally chosen combinations of future GNSS signals are tested and analyzed. The fourth minor objective of the thesis is accomplished in Chapter Six.

Chapter Seven draws important conclusions from the preceding chapters and summarizes the findings of the research. Chapter Seven recaps how the objectives of the thesis have been met and gives recommendations for future research in this field.

1.5 Future GNSS Positioning Scenarios

In order to accomplish the objectives of this thesis, it is necessary to establish some assumptions about how the future signals will be used in the future. To this end, four different processing scenarios have been chosen as the most likely scenarios that users of future GNSS technology will have access to. These scenarios, which will be compared throughout the remainder of this research, are described in this section.

While it is difficult to determine which scenarios will gain the most widespread use, the scenarios described below have been chosen because they are the most likely scenarios that will be used for precise kinematic applications in the future (according to Fontana et al., 2001). The first scenario, coined GPS2 is the current dual-frequency GPS case and will be used as a baseline against which the other scenarios will be compared. GPS3 is the processing scenario of modernized GPS where all three carrier phase measurements will be used along with the L2C and L5 civilian pseudorange codes. This scenario will likely be the first commercially available scenario since there are already functioning L5 capable receivers in existence (e.g. the NovAtel WAAS Reference Receiver G-II).

GPS/GAL2 is a scenario using both GPS and Galileo measurements, but only the two shared frequencies of each system (L1/E1 and L5/E5a) are used. This scenario is likely to have applications in the aviation industry because both the L1/E1 and L5/E5a bands lie in the reserved Aeronautical Radio Navigation Service frequency band. Finally, GPS/GAL3 is a dual-system scenario using triple-frequency GPS and triple-frequency Galileo measurements together. Receivers that output all six freely available carrier phase measurements will probably be more expensive due to the complicated RF front-end and the number of correlators required, but they will provide the most redundancy and best accuracy of all the scenarios. The four scenarios are summarized in Table 1.1.

Table 1.1: Positioning Scenarios

Scenario	Scheduled Full Operational Capacity	GNSS Type	Measurements Used	
			Carrier Phase	Code
GPS 2	Present	GPS	L1,L2	C/A, P2
		Galileo	-	-
GPS 3	2013	GPS	L1, L2, L5	L2C, L5
		Galileo	-	-
GPS / GAL 2	2013	GPS	L1, L5	C/A, L5
		Galileo	E1, E5a	E1, E5a
GPS / GAL 3	2013	GPS	L1, L2, L5	L2C, L5
		Galileo	E1, E5a, E5b	E1, E5a

Chapter Two: Functional and Stochastic Positioning Models for Future GNSS

The basic mathematical models that are commonly used with single or dual-frequency GPS processors will also be valid when processing multi-system (GPS and Galileo) and/or triple frequency GNSS measurements. However, there are some implications when combining measurements of GPS of Galileo that must be considered. This chapter will describe the mathematical models used for processing measurements from multiple systems that have been used for the analysis in this thesis. First the functional and stochastic components of the measurement model will be described with an emphasis on the differences that come with future GNSS signals. Next the dynamic model that has been used to describe the time variation of the simulated parameters is explained. Finally, the Kalman filter estimation technique that combines the measurement model and the dynamic model to sequentially estimate the final position solution is shown. Emphasis has been placed on those elements of the mathematical models that will be affected by the inclusion of future GNSS measurements.

2.1 Measurement Model for Future GNSS Positioning

The measurement model is the mathematical model that relates the measurements to the unknown parameters. The measurement model consists of a functional component that deals with the deterministic values, and a stochastic component that describes the

uncertainty of the random variables. The functional part of a generic linear measurement model is given by,

$$z = Hx + v \qquad (2.1)$$

where z is the vector of observations, x is the vector of unknown parameters, v is the vector of measurement residuals and H is the design matrix that relates the unknown parameters to the measurements. The stochastic part of the model is expressed by the variance-covariance matrices of the observations, R, and the parameters, P. The remainder of section 2.1 will discuss the definitions of these vectors and matrices.

2.1.1 Functional Component

The basic observation equations for satellite positioning are well-known and are given in Equations (2.2) through (2.5). Equations (2.2) and (2.3) are the pseudorange and carrier phase measurements from a receiver A, to a GPS satellite i, and Equations (2.4) and (2.5) are the pseudorange and carrier phase measurements from a receiver A to a Galileo satellite m.

$$P_A^i = \rho_A^i + c\left(dT_A^{GPS} - dt_{GPS}^i\right) + dI_A^i + dTr_A^i + d\rho_A^i + \varepsilon \qquad (2.2)$$

$$\Phi_A^i = \rho_A^i + c\left(dT_A^{GPS} - dt_{GPS}^i\right) - dI_A^i + dTr_A^i + d\rho_A^i + \lambda N_A^i + \varepsilon \qquad (2.3)$$

$$P_A^m = \rho_A^m + c\left(dT_A^{GAL} - dt_{GAL}^m\right) + dI_A^m + dTr_A^m + d\rho_A^m + \varepsilon \quad (2.4)$$

$$\Phi_A^m = \rho_A^m + c\left(dT_A^{GAL} - dt_{GAL}^m\right) + dI_A^m + dTr_A^m + d\rho_A^m + \lambda N_A^m + \varepsilon \quad (2.5)$$

The terms in these equations are described in the following list:

Term	Description	Units
P_A^i	Pseudorange measurement received at receiver *A* from satellite *i*	Metres
Φ_A^i	Carrier phase measurement received at receiver *A* from satellite *i*	Metres
ρ_A^i	Geometric range from receiver *A* to satellite *i*	Metres
c	Speed of light in a vacuum	Metres per second
dT_A^{GPS}, dT_A^{GAL}	Clock offset between receiver clock *A* and GPS Time and GST, respectively	Seconds
dt_{GPS}^i, dt_{GAL}^i	Clock offset between satellite clock, *i* and GPS Time and GST, respectively	Seconds
dI_A^i	Transmission delay or advance due to the effect of the ionosphere	Metres
dTr_A^i	Transmission delay due to the effect of the neutral atmosphere	Metres
$d\rho_A^i$	Orbital error projected onto the line of sight	Metres

	between the receiver and satellite	
λ	Wavelength of the carrier signal	Metres
N_A^i	Initial carrier phase ambiguity	Cycles
ε	Random noise and multipath	Metres

2.1.1.1 Double Differencing Measurements in a Combined GPS/Galileo Processor

For precise applications the observation equations are differenced between satellites and between receivers in order to eliminate and/or reduce some of the unknown parameters. In traditional differential GPS positioning, measurements of the same carrier frequency are differenced between satellites in order to eliminate the receiver clock offset and differenced between receivers in order to eliminate the satellite clock offset and reduce the effect of spatially correlated error sources. Using the same double differencing procedure is desirable for combined GPS and Galileo measurements. However, in order to use *heterogeneous* double differences (double differences between satellites from different systems), three considerations must be addressed: the carrier frequency of the measurements, the coordinate reference frame, and the time system.

To allow for integer ambiguity resolution, it is desirable for the double differencing operation to retain the integer nature of the ambiguity term. This condition demands that the underlying carrier frequency be the same between the measurements of the two

systems. To demonstrate this condition, consider a double difference between two receivers, *A* and *B*, and the GPS L1 measurement from satellite *i* and the GPS L2 measurement from satellite *j*. The resulting carrier phase double difference in units of L1 cycles is given by:

$$\Delta\phi_{AB}^{i} - \frac{\lambda_{L2}}{\lambda_{L1}}\Delta\phi_{AB}^{j} = \frac{1}{\lambda_{L1}}\left(\Delta\rho_{AB}^{ij} - \Delta dI_{AB}^{ij} + \Delta dTr_{AB}^{ij} + \Delta d\rho_{AB}^{ij}\right) + \nabla\Delta N_{AB}^{ij} + \overbrace{\frac{\lambda_{L1} - \lambda_{L2}}{\lambda_{L1}}\Delta N_{AB}^{j}}^{\text{non-integer}} + \varepsilon_{\nabla\Delta} \qquad (2.6)$$

where Δ is the single difference between receivers operator, ∇ is the single difference between satellites operator, and $\nabla\Delta$ is the double differencing operator. Clearly, the integer nature of the ambiguity has been lost, making it difficult to take advantage of the integer ambiguity constraint. This is one of the obstacles making integer ambiguity fixing more difficult for systems that use Frequency Division Multiple Access (FDMA) like the Russian Global Navigation Satellite System, GLONASS. When the observations of such systems are double differenced, the initial carrier phase ambiguity consists of both an integer component *and* a non-integer component (Habrich, 1999).

Another condition for double differencing to be beneficial is that the reference coordinate frames must be the same or the transformation between the systems must be known. This condition is necessary because the satellite coordinates are usually considered to be

known in the adjustment. A common reference frame - or a known transformation between frames - is necessary in order for the locations of both satellites to be used. Fortunately, since the coordinate reference frames for GPS and Galileo (WGS-84 and GTRF respectively) are expected to agree at the centimetre level, they can be considered interchangeable. Hence, for precise kinematic applications, the different coordinate reference frames should not affect the double-differencing process when using GPS and Galileo measurements together (Hein et al. 2002).

The last consideration when forming heterogeneous double differences is the time system of the two measurements. In order to better understand the satellite and receiver clock offset terms in Equations (2.2) through (2.5), Figure 2.1 illustrates the GPS and Galileo pseudorange measurements in the absence of all other sources of error.

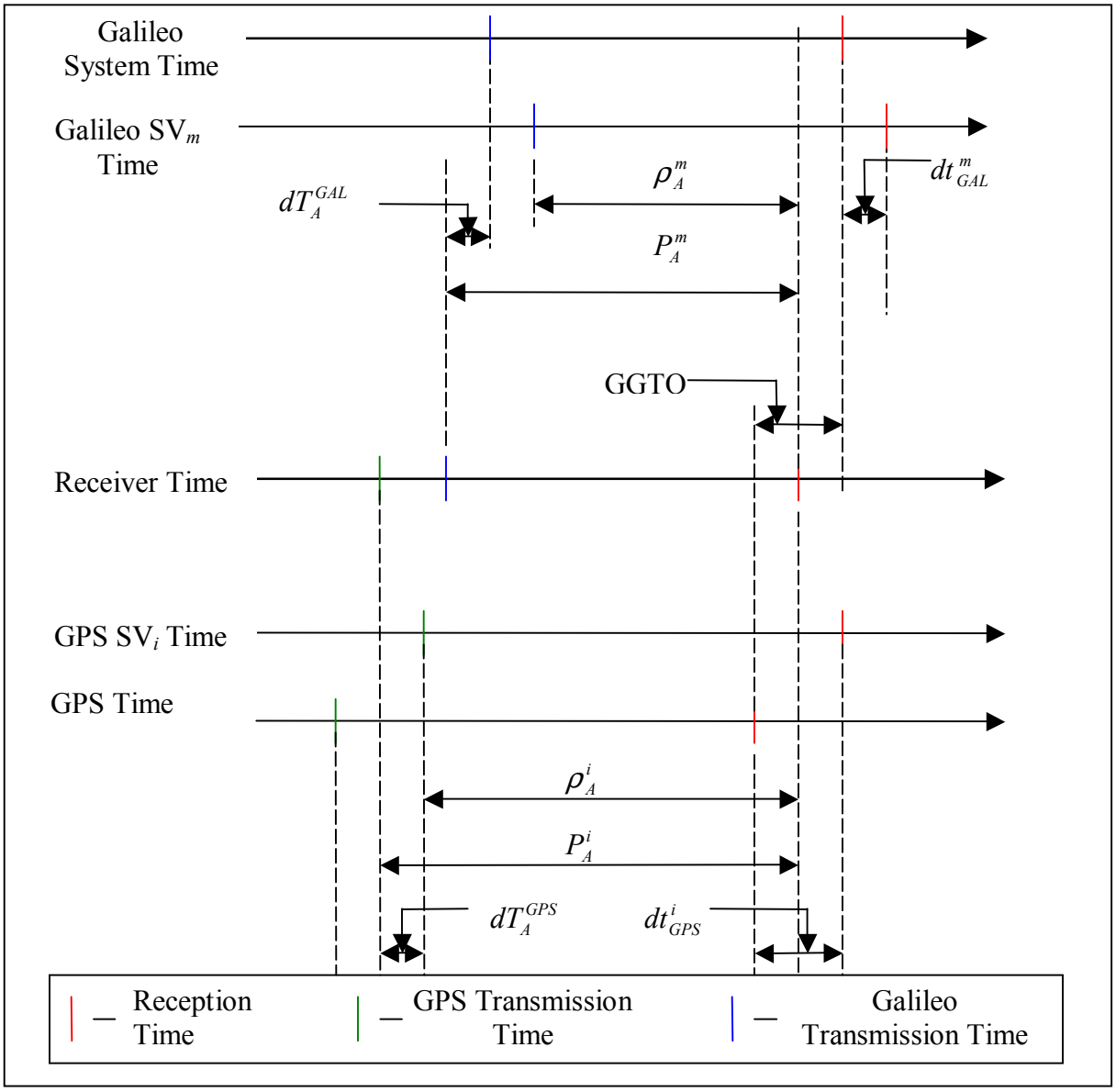

Figure 2.1: Time Scale Illustration

Since the offset between the receiver time and GPS Time and the offset between the receiver time and GST are different, these terms are not eliminated through double

differencing with a GPS and a Galileo satellite. As a result any double differences between GPS and Galileo measurements will have a residual clock offset: the GPS Galileo Time Offset (GGTO). This is shown in the following double difference on the L1/E1 frequency between receivers *A* and *B* and GPS satellite *i* and Galileo satellite *m*.

$$\nabla\Delta\Phi_{AB}^{im} = \nabla\Delta\rho_{AB}^{im} - \nabla\Delta dI_{AB}^{im} + \nabla\Delta dTr_{AB}^{im} + \nabla\Delta d\rho_{AB}^{im} + \lambda_{L1/E1}\nabla\Delta N_{AB}^{im} + \underbrace{c\left[\left(dT_A^{GPS} - dT_B^{GPS}\right) - \left(dT_A^{GAL} - dT_B^{GAL}\right)\right]}_{GPS-GalileoTimeOffset(GGTO)} + \varepsilon_{\nabla\Delta} \qquad (2.7)$$

The GGTO can be dealt with in one of three ways:

1. Removal using the broadcast value that will be available in the Galileo navigation message
2. Estimation as an additional state in the processor
3. Elimination by using both a GPS and a Galileo reference satellite and forming double differences only between measurements from the same system

According to the most recent version of the *Galileo Mission Requirements Document* (Galileo Mission Requirements Document Issue 5.0 – Draft, 2002), the broadcast value of the GGTO will have an accuracy of five nanoseconds at the two-sigma confidence level. This translates into about 1.5 metres and is clearly not accurate enough for precise applications. Therefore, developers of precise GNSS equipment and software will have

to choose between using *heterogeneous* double differences (see Figure 2.2) and estimating the GGTO or using only *homogeneous* double differences (see Figure 2.3) which eliminates the GGTO. Of these two options, the latter is superior because if there are any other unforeseen system biases, these will also be eliminated by using only homogenous double differences. Therefore, using two reference satellites (one for GPS and one for Galileo) can be seen as the safer option for future developers and has been adopted for the remainder of this thesis.

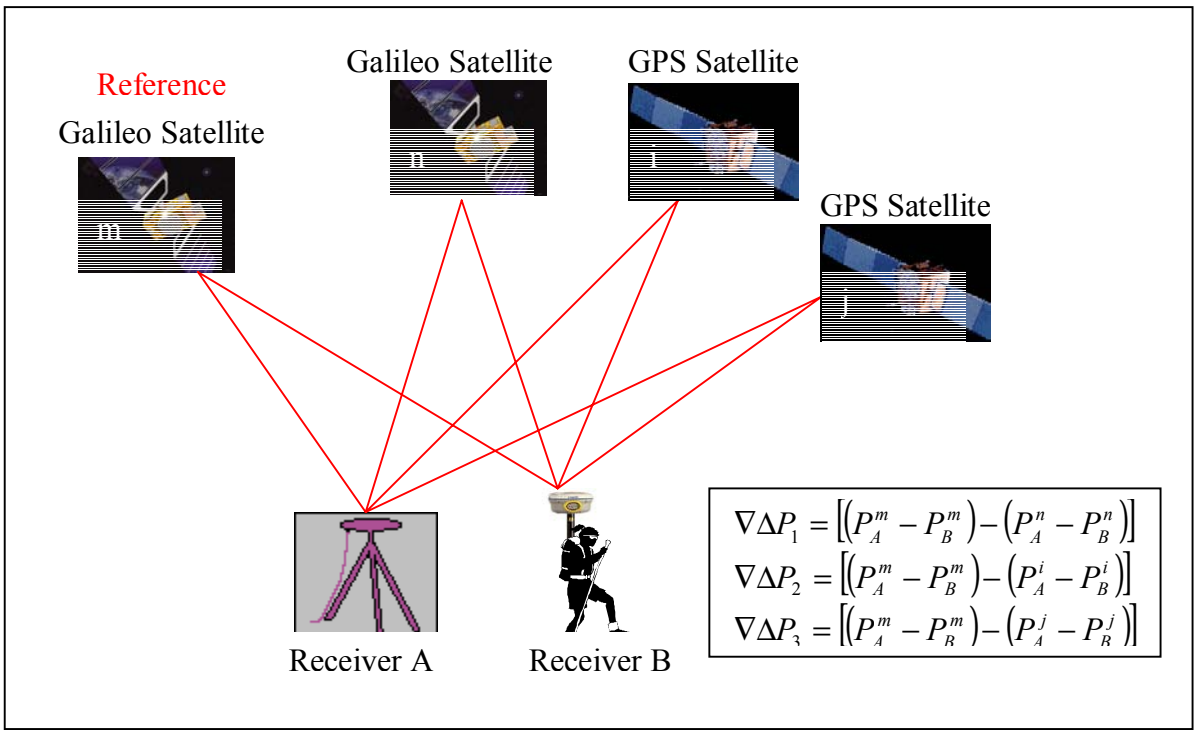

Figure 2.2: Heterogeneous Double Differences

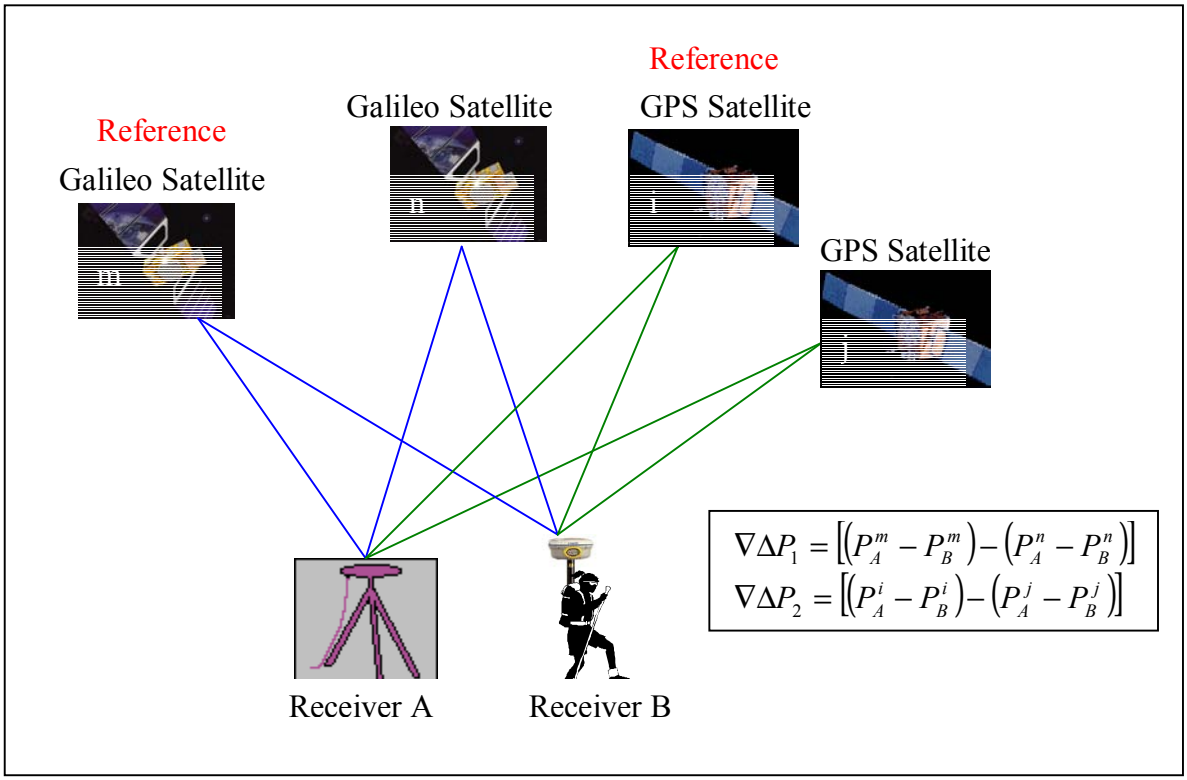

Figure 2.3: Homogeneous Double Differences

After applying double differences between GPS satellites and between Galileo satellites, the final double differenced observation equations become:

$$\begin{bmatrix} \nabla\Delta P_{AB}^{ij}(GPS) \\ \nabla\Delta P_{AB}^{mn}(GAL) \end{bmatrix} = \begin{bmatrix} \nabla\Delta\rho_{AB}^{ij} + \nabla\Delta dI_{AB}^{ij} + \varepsilon_{\nabla\Delta} \\ \nabla\Delta\rho_{AB}^{mn} + \nabla\Delta dI_{AB}^{mn} + \varepsilon_{\nabla\Delta} \end{bmatrix} \qquad (2.8)$$

and

$$\begin{bmatrix} \nabla\Delta\Phi_{AB}^{ij}(GPS) \\ \nabla\Delta\Phi_{AB}^{mn}(GAL) \end{bmatrix} = \begin{bmatrix} \nabla\Delta\rho_{AB}^{ij} + \lambda\nabla\Delta N_{AB}^{ij} - \nabla\Delta dI_{AB}^{ij} + \varepsilon_{\nabla\Delta} \\ \nabla\Delta\rho_{AB}^{mn} + \lambda\nabla\Delta N_{AB}^{mn} - \nabla\Delta dI_{AB}^{mn} + \varepsilon_{\nabla\Delta} \end{bmatrix} \qquad (2.9)$$

where i and m represent the GPS and Galileo reference satellites and j and n represent other GPS and Galileo satellites and $\varepsilon_{\nabla\Delta}$ is the random noise of a double differenced observation.

It should be noted that the tropospheric delay term, dTr and the orbital error term $d\rho$ have been neglected. The tropospheric delay can be ignored because it is assumed that when the tropospheric delay is modeled using an appropriate model and mapping function and then double differenced, the residual error is negligible. According to Parkinson et al. (1995), simple tropospheric models remove about 90% of the tropospheric error on an undifferenced measurement. Of course, the assumption that the residual tropospheric effects can be neglected breaks down when the baseline distance increases, when small scale variations in the tropospheric conditions exist, and especially when the height difference between the two receivers is substantial. Some examples of effective tropospheric models include the Saastamoinen model (Saastamoinen, 1972), the UNB3 model (Collins et al. 1996) and the Modified Hopfield Model (Goad et al. 1974), while mapping function can be found in Neill (1996), Lanyi (1984), and Ifadis (2000) to name a few.

It is commonly assumed that the double differenced orbital errors can be neglected. The positions of the satellites are computed from the broadcast ephemeris, which have a nominal accuracy of about 2.3 metres at the 1σ level (Cannon, 2002). When the

observations are double differenced, the error propagated onto the estimated baseline is approximately 0.125 parts per million. For example, the errors in satellite position projected onto a 50 km baseline would cause 6.25 millimetres of error. An error of this magnitude can safely be neglected as it is well below the level of other dominant error sources like the atmospheric delays, and multipath.

One last step is necessary to make the observation equations (Equations (2.8) and (2.9)) fit the generic functional measurement model from Equation (2.1). Since the desired result is the three dimensional position of the rover receiver, the geometric range term must be linearized through a Taylor series expansion. Equation (2.10) below shows an example of the linearization of the range from satellite *i* to receiver *B*.

$$\begin{aligned}\rho_B^i &= \left(X^i - X_B\right)^2 + \left(Y^i - Y_B\right)^2 + \left(Z^i - Z_B\right)^2 \\ &= \overset{\circ}{\rho}_B^i + \frac{\partial \rho_B^i}{\partial \overset{\circ}{X}_B}\cdot\left(X_B - \overset{\circ}{X}_B\right) + \frac{\partial \rho_B^i}{\partial \overset{\circ}{Y}_B}\cdot\left(Y_B - \overset{\circ}{Y}_B\right) + \frac{\partial \rho_B^i}{\partial \overset{\circ}{Z}_B}\cdot\left(Z_B - \overset{\circ}{Z}_B\right) + \cdots \\ &= \overset{\circ}{\rho}_B^i + \frac{\partial \rho_B^i}{\partial \overset{\circ}{X}_B}\cdot \delta x_B + \frac{\partial \rho_B^i}{\partial \overset{\circ}{Y}_B}\cdot \delta y_B + \frac{\partial \rho_B^i}{\partial \overset{\circ}{Z}_B}\cdot \delta z_B + \cdots\end{aligned} \qquad (2.10)$$

where *X,Y,* and *Z* are the Cartesian coordinates in the appropriate coordinate reference frame and the ∘ symbol indicates an initial approximate. The higher order terms can be ignored assuming that the initial approximate of the rover receiver position is close to the estimated position.

Given the above definitions, and following the structure of equation (2.1), the final linearized double differenced functional component of the measurement model is summarized in the following example of double differenced pseudorange and carrier phase measurements from receivers *A* (reference station) and *B* (rover station) to GPS satellites *i* and *j* and Galileo satellites *m* and *n*.

Measurement Vector:

$$z = \begin{bmatrix} \nabla\Delta P_{AB}^{ij} - \nabla\Delta \overset{\circ}{\rho}{}_{AB}^{ij} - \nabla\Delta \overset{\circ}{dI}{}_{AB}^{ij} \\ \nabla\Delta\Phi_{AB}^{ij} - \nabla\Delta \overset{\circ}{\rho}{}_{AB}^{ij} + \nabla\Delta \overset{\circ}{dI}{}_{AB}^{ij} - \nabla\Delta \overset{\circ}{N}{}_{AB}^{ij} \\ \nabla\Delta P_{AB}^{mn} - \nabla\Delta \overset{\circ}{\rho}{}_{AB}^{mn} - \nabla\Delta \overset{\circ}{dI}{}_{AB}^{mn} \\ \nabla\Delta\Phi_{AB}^{mn} - \nabla\Delta \overset{\circ}{\rho}{}_{AB}^{mn} + \nabla\Delta \overset{\circ}{dI}{}_{AB}^{mn} - \nabla\Delta \overset{\circ}{N}{}_{AB}^{mn} \end{bmatrix} \qquad (2.11)$$

Vector of Unknown Parameters:

$$x = \begin{bmatrix} \delta x_B \\ \delta y_B \\ \delta z_B \\ \delta\nabla\Delta dI_{AB}^{ij} \\ \delta\nabla\Delta N_{AB}^{ij} \\ \delta\nabla\Delta dI_{AB}^{mn} \\ \delta\nabla\Delta N_{AB}^{mn} \end{bmatrix} \qquad (2.12)$$

Design Matrix:

$$H = \begin{bmatrix} \frac{\partial \rho_B^i}{\partial x_B} - \frac{\partial \rho_B^j}{\partial x_B} & \frac{\partial \rho_B^i}{\partial y_B} - \frac{\partial \rho_B^j}{\partial y_B} & \frac{\partial \rho_B^i}{\partial z_B} - \frac{\partial \rho_B^j}{\partial z_B} & 1 & 0 & 0 & 0 \\ \frac{\partial \rho_B^i}{\partial x_B} - \frac{\partial \rho_B^j}{\partial x_B} & \frac{\partial \rho_B^i}{\partial y_B} - \frac{\partial \rho_B^j}{\partial y_B} & \frac{\partial \rho_B^i}{\partial z_B} - \frac{\partial \rho_B^j}{\partial z_B} & -1 & \lambda & 0 & 0 \\ \frac{\partial \rho_B^m}{\partial y_B} - \frac{\partial \rho_B^n}{\partial y_B} & \frac{\partial \rho_B^m}{\partial y_B} - \frac{\partial \rho_B^n}{\partial y_B} & \frac{\partial \rho_B^m}{\partial z_B} - \frac{\partial \rho_B^n}{\partial z_B} & 0 & 0 & 1 & 0 \\ \frac{\partial \rho_B^m}{\partial y_B} - \frac{\partial \rho_B^n}{\partial y_B} & \frac{\partial \rho_B^m}{\partial y_B} - \frac{\partial \rho_B^n}{\partial y_B} & \frac{\partial \rho_B^m}{\partial z_B} - \frac{\partial \rho_B^n}{\partial z_B} & 0 & 0 & -1 & \lambda \end{bmatrix} \quad (2.13)$$

It should be noted that the state vector shown in Equation (2.12) contains *corrections* to the position, *corrections* to the ionospheric delays, and *corrections* to the ambiguity values. This mechanization has been adopted for the processing throughout this thesis.

2.1.1.2 Ionospheric Errors

As shown in Section 2.1.1.1, the ionospheric delay is treated as a state to be estimated. Since the ionospheric delay is highly correlated with the initial carrier phase ambiguity, a pseudo-observation is used to enable the ionospheric delay state to converge. The ionospheric pseudo-observation equation is given by,

$$\nabla \Delta dI_{pseudo-observation} - \nabla \Delta \overset{\circ}{dI} = \delta \nabla \Delta dI_{estimated} \quad (2.14)$$

where $\nabla\Delta dI_{pseudo-observation}$ is an externally determined value of the expected ionospheric delay and $\delta\nabla\Delta dI_{estimated}$ is the ionospheric delay state to be estimated. The pseudo-observation could come from the GPS broadcast ionospheric model, global ionosphere maps, such as those provided by the CODE analysis center ("The AIUB IGS Page": http://www.cx.unibe.ch/aiub/igs.html) or it could simply be set to zero. The weighting of this pseudo-observation in the measurement covariance matrix has a significant impact on ambiguity resolution and the accuracy of the final baseline solution. In Chapter Four, the weighting of the ionospheric pseudo-observable is discussed further and some experimental results showing the impact that future signals will have on the ability to estimate the ionospheric delay are given.

2.1.2 Stochastic Component

In order to capture the correlations between double differenced GNSS observations, the measurement covariance matrix must be derived from the original undifferenced observations and then transformed to the double differenced covariance matrix via the double differencing matrix, B through the equation,

$$R_{\nabla\Delta} = B \cdot R_{undiff} \cdot B^T \qquad (2.15)$$

where $R_{\nabla\Delta}$ denotes the double differenced measurement covariance matrix and R_{undiff} is the undifferenced measurement covariance matrix. The double differencing matrix is populated with 0's, 1's and -1's and simply forms the double differences from the undifferenced observations. When Equation (2.15) is applied to an undifferenced covariance matrix, three different forms of covariance result. In the following equations, $\left(\sigma_A^i\right)^2$ is the variance of a single undifferenced observation from receiver *A* to satellite *i*; σ_{AB}^i is the covariance between observations from receivers *A* and *B* to satellite *i*; σ_A^{ij} is the covariance between two observations from the same receiver, *A*, to different satellites, *i* and *j*; and σ_{AB}^{ij} is the covariance between two observations from different receivers to different satellites. The different forms of covariance are:

1. The covariance between two observations with two common satellites. This is actually the variance of a single double difference observation and is given by:

$$\sigma^2\left(\nabla\Delta_{AB}^{ij}\right) = \left(\sigma_A^i\right)^2 + \left(\sigma_B^i\right)^2 + \left(\sigma_A^j\right)^2 + \left(\sigma_B^j\right)^2 - 2\sigma_A^{ij} - 2\sigma_B^{ij} - 2\sigma_{AB}^i - 2\sigma_{AB}^j + 2\sigma_{AB}^{ij} + 2\sigma_{AB}^{ji} \qquad (2.16)$$

2. The covariance between two observations with one common satellite. This form of covariance describes the correlations between two double differenced observations of the same type (i.e. two GPS observations or two Galileo observations), since they would share the same reference satellite. The equation is:

$$\sigma\left(\nabla\Delta^{ij}_{AB},\nabla\Delta^{ik}_{AB}\right)=\left(\sigma^{i}_{A}\right)^2+\left(\sigma^{i}_{B}\right)^2-\sigma^{ij}_{A}-\sigma^{ij}_{B}-\sigma^{ik}_{A} \\ -\sigma^{ik}_{B}+\sigma^{jk}_{A}+\sigma^{jk}_{B}-2\sigma^{i}_{AB}+\sigma^{ij}_{AB} \\ +\sigma^{ji}_{AB}+\sigma^{ik}_{AB}+\sigma^{ki}_{AB}-\sigma^{jk}_{AB}-\sigma^{kj}_{AB} \qquad (2.17)$$

3. The covariance between two observations with no common satellites. This form of covariance describes the correlation between two double differenced observations that are from different systems (i.e. the correlation between GPS and Galileo double difference observations). The equation is:

$$\sigma\left(\nabla\Delta^{ij}_{AB},\nabla\Delta^{mn}_{AB}\right)=\sigma^{im}_{A}-\sigma^{jm}_{A}-\sigma^{im}_{BA}+\sigma^{jm}_{BA}-\sigma^{in}_{A} \\ +\sigma^{jn}_{A}+\sigma^{in}_{BA}-\sigma^{jn}_{BA}-\sigma^{im}_{AB}+\sigma^{jm}_{AB} \\ +\sigma^{im}_{B}-\sigma^{jm}_{B}+\sigma^{in}_{AB}-\sigma^{jn}_{AB}-\sigma^{in}_{B}+\sigma^{jn}_{B} \qquad (2.18)$$

Consider an example with six satellites: three GPS (*i,j,k*) and three Galileo (*m,n,o*). The double differenced measurement covariance matrix for single frequency carrier phase observations would contain four observations: two GPS double differences and two Galileo double differences. The resulting symmetric covariance matrix is shown below where *SYM* indicates symmetry in the lower left half of the matrix. The diagonal terms follow the first type of covariance (two common satellites), the four terms in the upper right corner follow the third type of covariance (no common satellites) and the remaining terms follow the second type of covariance (one common satellite).

$$R_{\nabla\Delta} = \begin{bmatrix} \sigma^2\left(\nabla\Delta^{ij}_{AB}\right) & \sigma\left(\nabla\Delta^{ij}_{AB}, \nabla\Delta^{ik}_{AB}\right) & \sigma\left(\nabla\Delta^{ij}_{AB}, \nabla\Delta^{mn}_{AB}\right) & \sigma\left(\nabla\Delta^{ij}_{AB}, \nabla\Delta^{mo}_{AB}\right) \\ & \sigma^2\left(\nabla\Delta^{ik}_{AB}\right) & \sigma\left(\nabla\Delta^{ik}_{AB}, \nabla\Delta^{mn}_{AB}\right) & \sigma\left(\nabla\Delta^{ik}_{AB}, \nabla\Delta^{mo}_{AB}\right) \\ & & \sigma^2\left(\nabla\Delta^{mn}_{AB}\right) & \sigma\left(\nabla\Delta^{mn}_{AB}, \nabla\Delta^{mo}_{AB}\right) \\ & SYM & & \sigma^2\left(\nabla\Delta^{mo}_{AB}\right) \end{bmatrix} \quad (2.19)$$

In order to implement this covariance model, the undifferenced covariance terms found on the right hand sides of Equations (2.16), (2.17), and (2.18) must be defined. According to the law of propagation of errors, the individual error sources can be separated and summed to arrive at the final covariance terms. Therefore, the necessary task is to create undifferenced covariance matrices corresponding to each individual error source (ionosphere, troposphere, multipath, thermal noise, orbital, receiver clock, satellite clock, etc.) and sum them as in Equation (2.20).

$$R_{\nabla\Delta} = B \cdot \left(R^{undiff}_{iono} + R^{undiff}_{tropo} + R^{undiff}_{mult} + R^{undiff}_{noise} + R^{undiff}_{orbit} + R^{undiff}_{rec.clk} + R^{undiff}_{sat.clk} + \cdots\right) \cdot B^T \quad (2.20)$$

Defining these matrices is a topic of research that has received increasing attention in the past several years. This task is beyond the scope of this thesis, but the reader is referred to Radovanovic (2002) and El-Rabbany (1994) for a thorough treatment of the physical and temporal correlations between undifferenced observations. The model used in this research is the one described by Radovanovic (2002). This model represents each error

source with a constant zenith delay and an elevation angle dependent mapping function. The general form is

$$\sigma^2 = m(\varepsilon) \cdot \sigma^2_{zenith} \qquad (2.21)$$

where σ^2 is the final variance, $m(\varepsilon)$ is the elevation dependent mapping function, and σ^2_{zenith} is the measurement variance for a satellite at zenith. In order to model the decorrelation of error sources as distance between the receivers and/or satellites increases, exponential decay functions are used. The details and derivation of this error model are beyond the scope of this thesis, but the relevant equations that were used for the subsequent experiments can be found in Radovanovic (2002).

While all of the error sources listed in Equation (2.20) exist to some extent, the remainder of this thesis will focus only on the ionospheric, tropospheric and the lumped thermal noise/multipath errors because these are the dominant error sources. The other sources of error are either eliminated (receiver and satellite clock errors) or mitigated enough to be ignored (orbital errors) through the double differencing process.

2.1.2.1 Correlations between Observation Types

The total observation vector contains three distinct types of observations: pseudorange observations, ionospheric pseudo-observations, and carrier phase observations. By definition, there are no correlations between the ionospheric pseudo-observable and any other type of observation since it comes from an external source.

Liu (2001) conducted zero-baseline tests on a network of ASHTECH Z-XII dual-frequency GPS receivers and found that all the correlations between different observations types (C1, reconstructed P1, reconstructed P2, L1, and L2) were insignificant except for the correlation between the L1 and L2 carrier phase observations. These findings have been applied in this work so that the elements in the total double differenced design matrix corresponding to correlations between pseudorange observations and any other type of observation were set to zero. Correlations between carrier phase observations are not neglected and are discussed in Section 2.1.2.2. How to treat correlations between ionospheric pseudo-observations depends on where the ionospheric pseudo-observations come from. If the GPS broadcast ionospheric model or a global ionospheric map is used to generate the external ionospheric pseudo-observations, then the observations would be correlated because all the pseudo-observations are derived from the same model. However, in this research, the external

ionospheric observation is simply set to zero. Consequently, there are no correlations between the ionospheric pseudo-observations themselves or between ionospheric pseudo-observations and any other type of data and the covariance matrix of ionospheric pseudo-observations is diagonal.

A symbolic representation of a typical double differenced measurement covariance matrix is shown below:

$$R_{\nabla\Delta} = \begin{bmatrix} [\sigma^2(P)] & 0 & 0 \\ 0 & [\sigma^2(dI)] & 0 \\ 0 & 0 & [\sigma^2(\Phi)] \end{bmatrix} \qquad (2.22)$$

where, $[\sigma^2(P)]$ is the covariance matrix corresponding to the code observations, $[\sigma^2(dI)]$ is the covariance matrix corresponding to the ionospheric pseudo-observations, and $[\sigma^2(\Phi)]$ is the covariance matrix corresponding to the carrier phase observations. Each of these covariance matrices is defined in the following equations where the subscripts, 1 and 2 refer to different frequencies.

$$[\sigma^2(P)] = \begin{bmatrix} (\sigma_{GPS}^{P_1})^2 & 0 & 0 & 0 \\ 0 & (\sigma_{GPS}^{P_2})^2 & 0 & 0 \\ 0 & 0 & (\sigma_{GAL}^{P_1})^2 & 0 \\ 0 & 0 & 0 & (\sigma_{GAL}^{P_2})^2 \end{bmatrix} \qquad (2.23)$$

$$\left[\sigma^2(dI)\right] = \begin{bmatrix} \left(\sigma_{GPS}^{dI}\right)^2 & 0 \\ 0 & \left(\sigma_{GAL}^{dI}\right)^2 \end{bmatrix} \quad (2.24)$$

$$\left[\sigma^2(\Phi)\right] = \begin{bmatrix} \left(\sigma_{GPS}^{\Phi_1}\right)^2 & \sigma_{GPS}^{\Phi_1,\Phi_2} & \sigma_{GPS,GAL}^{\Phi_1} & \sigma_{GPS,GAL}^{\Phi_1,\Phi_2} \\ \sigma_{GPS}^{\Phi_2,\Phi_1} & \left(\sigma_{GPS}^{\Phi_2}\right)^2 & \sigma_{GPS,GAL}^{\Phi_2,\Phi_1} & \sigma_{GPS,GAL}^{\Phi_2} \\ \sigma_{GAL,GPS}^{\Phi_1} & \sigma_{GAL,GPS}^{\Phi_1,\Phi_2} & \left(\sigma_{GAL}^{\Phi_1}\right)^2 & \sigma_{GAL}^{\Phi_1,\Phi_2} \\ \sigma_{GAL,GPS}^{\Phi_2,\Phi_1} & \sigma_{GAL,GPS}^{\Phi_2} & \sigma_{GAL}^{\Phi_2,\Phi_1} & \left(\sigma_{GAL}^{\Phi_2}\right) \end{bmatrix} \quad (2.25)$$

2.1.2.2 Inter-Frequency Correlations

The ionosphere is a dispersive medium so it affects each carrier frequency differently; resulting in highly correlated ionospheric errors between the carrier frequencies. These correlations must be incorporated into the GNSS stochastic model.

The ionospheric effects (in metres) on the three future GPS signals are given by the well-known equation (Hofmann-Wellenhof, 2000):

$$\begin{bmatrix} \delta I_{L1} \\ \delta I_{L2} \\ \delta I_{L5} \end{bmatrix} = 40.3 \cdot \begin{bmatrix} f_{L1}^{-2} \\ f_{L2}^{-2} \\ f_{L5}^{-2} \end{bmatrix} \cdot TEC \quad (2.26)$$

where δI_{Li} are the ionospheric errors in metres for each carrier frequency, f_{Li}^2 are the squares of the carrier frequencies in Hz, and TEC is the total electron content along the path between the receiver and the satellite in TECU (10^{16} electrons per square meter).

This error has the same magnitude, but opposite sign for pseudorange measurements and the corresponding carrier phase measurements; it delays the pseudorange and advances the carrier phase. It is not intuitive to work with quantities of TECU, so Equation (2.26) is often reparameterized in terms of the ionospheric error in units of metres on the L1 frequency. This different parameterization results in,

$$\begin{bmatrix} \delta I_{L1} \\ \delta I_{L2} \\ \delta I_{L5} \end{bmatrix} = \begin{bmatrix} 1 \\ f_{L1}^2 / f_{L2}^2 \\ f_{L1}^2 / f_{L5}^2 \end{bmatrix} \cdot \delta I_{L1} \qquad (2.27)$$

Applying the law of propagation of errors to Equation (2.27), we get,

$$\begin{bmatrix} \sigma_{I_{L1}}^2 & \sigma_{I_{L1,L2}} & \sigma_{I_{L1,L5}} \\ \sigma_{I_{L2,L1}} & \sigma_{I_{L2}}^2 & \sigma_{I_{L2,L5}} \\ \sigma_{I_{L5,L1}} & \sigma_{I_{L5,L2}} & \sigma_{I_{L5}}^2 \end{bmatrix} = \sigma_{I_{L1}}^2 \cdot \begin{bmatrix} 1 \\ f_{L1}^2 / f_{L2}^2 \\ f_{L1}^2 / f_{L5}^2 \end{bmatrix} \begin{bmatrix} 1 & f_{L1}^2 / f_{L2}^2 & f_{L1}^2 / f_{L5}^2 \end{bmatrix} \qquad (2.28)$$

where σ_{Li}^2 represents the variance in square metres.

The tropospheric delay is completely correlated because the troposphere is a non-dispersive medium affecting all L-Band frequencies in the same way. Mathematically, we have,

$$\begin{bmatrix} \delta T_{L1} \\ \delta T_{L2} \\ \delta T_{L5} \end{bmatrix} = \begin{bmatrix} 1 \\ 1 \\ 1 \end{bmatrix} \cdot \delta T \qquad (2.29)$$

where δT is the tropospheric delay in metres. Again, applying the law of propagation of errors, we get,

$$\begin{bmatrix} \sigma^2_{T_{L1}} & \sigma_{T_{L1,L2}} & \sigma_{T_{L1,L5}} \\ \sigma_{T_{L2,L1}} & \sigma^2_{T_{L2}} & \sigma_{T_{L2,L5}} \\ \sigma_{T_{L5,L1}} & \sigma_{T_{L5,L2}} & \sigma^2_{T_{L5}} \end{bmatrix} = \sigma^2_T \begin{bmatrix} 1 \\ 1 \\ 1 \end{bmatrix} \begin{bmatrix} 1 & 1 & 1 \end{bmatrix} \qquad (2.30)$$

The thermal noise and multipath are lumped together because they are uncorrelated between signals of different frequencies. The functional model is simply,

$$\begin{bmatrix} \delta n_{L1} \\ \delta n_{L2} \\ \delta n_{L5} \end{bmatrix} = \begin{bmatrix} \delta n_{L1} \\ \delta n_{L2} \\ \delta n_{L5} \end{bmatrix} \qquad (2.31)$$

where δn_{Li} is the error due to noise and/or multipath in metres.

Since the noise and multipath errors are uncorrelated between measurements of different frequencies, applying the law of error propagation of errors yields,

$$\begin{bmatrix} \sigma_{n_{L1}}^2 & 0 & 0 \\ 0 & \sigma_{n_{L2}}^2 & 0 \\ 0 & 0 & \sigma_{n_{L5}}^2 \end{bmatrix} = \begin{bmatrix} \sigma_{n_{L1}}^2 & 0 & 0 \\ 0 & \sigma_{n_{L2}}^2 & 0 \\ 0 & 0 & \sigma_{n_{L5}}^2 \end{bmatrix} \quad (2.32)$$

where $\sigma_{n_{Li}}^2$ is the variance due to noise and multipath in units of metres. The precision of the thermal noise and multipath is often assumed to be the same for each frequency when expressed in units of cycles of the respective signal. Therefore, Equation (2.32) can be reparameterized to,

$$\begin{bmatrix} \sigma_{n_{L1}}^2 & 0 & 0 \\ 0 & \sigma_{n_{L2}}^2 & 0 \\ 0 & 0 & \sigma_{n_{L5}}^2 \end{bmatrix} = \sigma_{n_{L1}}^2 \begin{bmatrix} 1 & 0 & 0 \\ 0 & f_{L1}^2 / f_{L2}^2 & 0 \\ 0 & 0 & f_{L1}^2 / f_{L5}^2 \end{bmatrix} \quad (2.33)$$

Given the preceding definitions of the individual correlations between carrier frequencies, the total covariance matrix describing the correlations among the carrier frequencies in square metres is:

$$\begin{bmatrix} \sigma_{L1}^2 & \sigma_{L1,L2} & \sigma_{L1,L5} \\ \sigma_{L2,L1} & \sigma_{L2}^2 & \sigma_{L2,L5} \\ \sigma_{L5,L1} & \sigma_{L5,L2} & \sigma_{L5}^2 \end{bmatrix} = \sigma_{I_{L1}}^2 \cdot \begin{bmatrix} 1 \\ f_{L1}^2 / f_{L2}^2 \\ f_{L1}^2 / f_{L5}^2 \end{bmatrix} \begin{bmatrix} 1 & f_{L1}^2 / f_{L2}^2 & f_{L1}^2 / f_{L5}^2 \end{bmatrix} + \sigma_T^2 \begin{bmatrix} 1 \\ 1 \\ 1 \end{bmatrix} \begin{bmatrix} 1 & 1 & 1 \end{bmatrix} + \sigma_{n_{L1}}^2 \begin{bmatrix} 1 & 0 & 0 \\ 0 & f_{L1}^2 / f_{L2}^2 & 0 \\ 0 & 0 & f_{L1}^2 / f_{L5}^2 \end{bmatrix} \quad (2.34)$$

where $\sigma^2_{I_{L1}}$, σ^2_T, $\sigma^2_{n_{L1}}$ are the variances of the ionosphere, troposphere, and noise/multipath on the L1 frequency in units of metres^2.

To relate these inter-frequency correlations back to the development of Section 2.1.2, let us rewrite Equation (2.34) as,

$$\begin{bmatrix} \sigma^2_{L1} & \sigma_{L1,L2} & \sigma_{L1,L5} \\ \sigma_{L2,L1} & \sigma^2_{L2} & \sigma_{L2,L5} \\ \sigma_{L5,L1} & \sigma_{L5,L2} & \sigma^2_{L5} \end{bmatrix} = \sigma^2_{I_{L1}} \cdot SF_{Iono} + \sigma^2_T \cdot SF_{Tropo} + \sigma^2_{n_{L1}} \cdot SF_{noise} \qquad (2.35)$$

where *SF* refers to the scale factors of the ionospheric, tropospheric and noise/multipath error source variances, respectively. Referring back to Equation (2.20), we can write a final expression for the entire double differenced measurement covariance matrix using the Kroneker product as follows:

$$R_{\nabla\Delta} = \left(B \cdot R^{undiff}_{Iono} \cdot B^T\right) \otimes SF_{Iono} + \left(B \cdot R^{undiff}_{Tropo} \cdot B^T\right) \otimes SF_{Tropo} + \left(B \cdot R^{undiff}_{Noise} \cdot B^T\right) \otimes SF_{Noise} \qquad (2.36)$$

An example of a total covariance matrix is given below for a scenario with triple frequency GPS and Galileo data over a five kilometre baseline. In this example, the following data types were used:

- GPS L2C and L5 codes
- Galileo E5a and E5b codes
- GPS L1, L2, and L5 carriers
- Galileo E1, E5a and E5b carriers

Figure 2.4 and Figure 2.5 show the pseudorange and carrier phase blocks of the measurement covariance matrix. In these two figures, the brightness value of the pixel indicates the magnitude of the variance or covariance. The lighter coloured pixels represent larger magnitude covariances and the darker pixels represent smaller magnitude covariances. The ionospheric pseudo-observation block is not shown because it is simply a diagonal matrix.

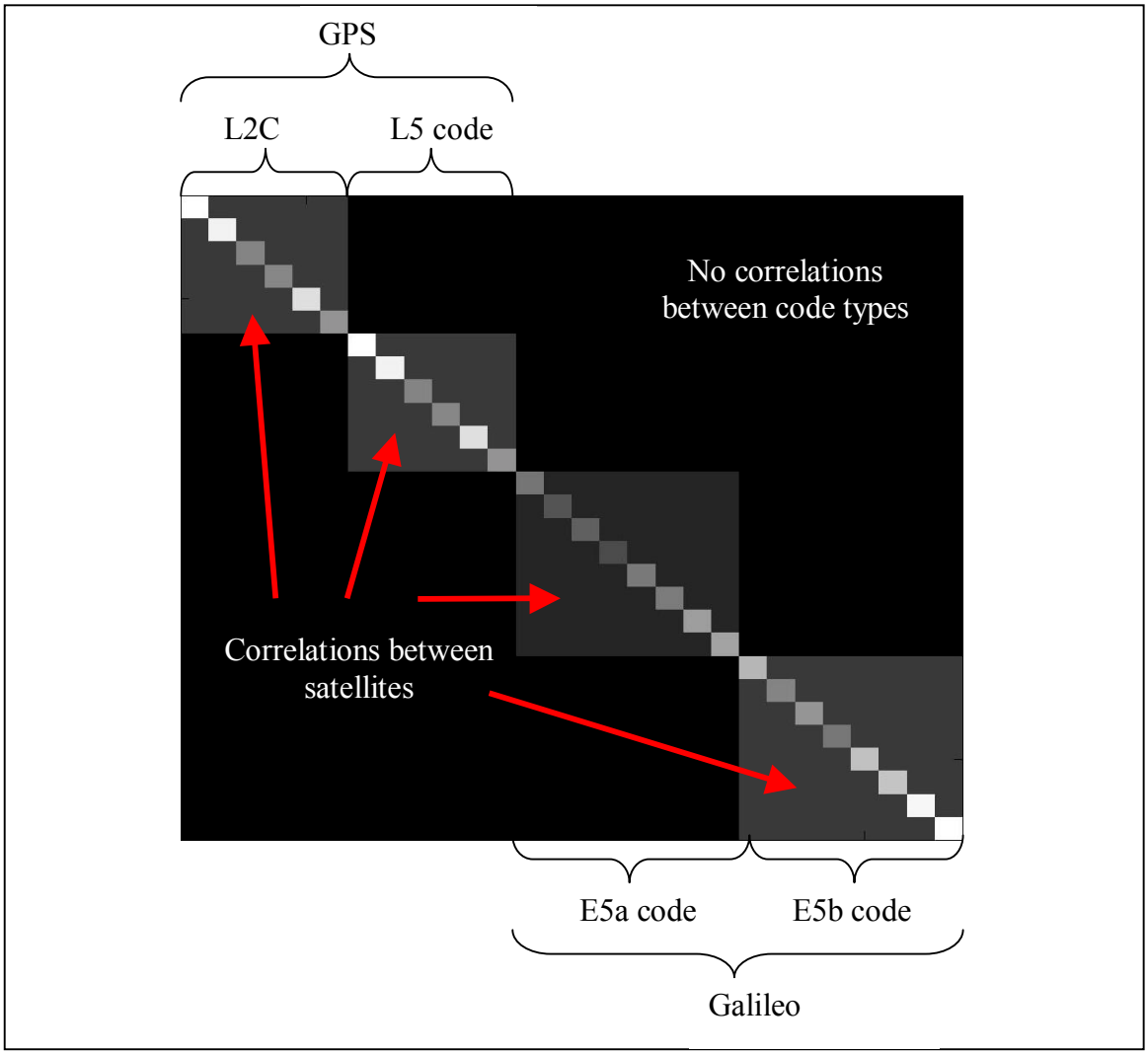

Figure 2.4: Pseudorange Measurement Covariance Matrix for GPS/Galileo Triple-Frequency Data

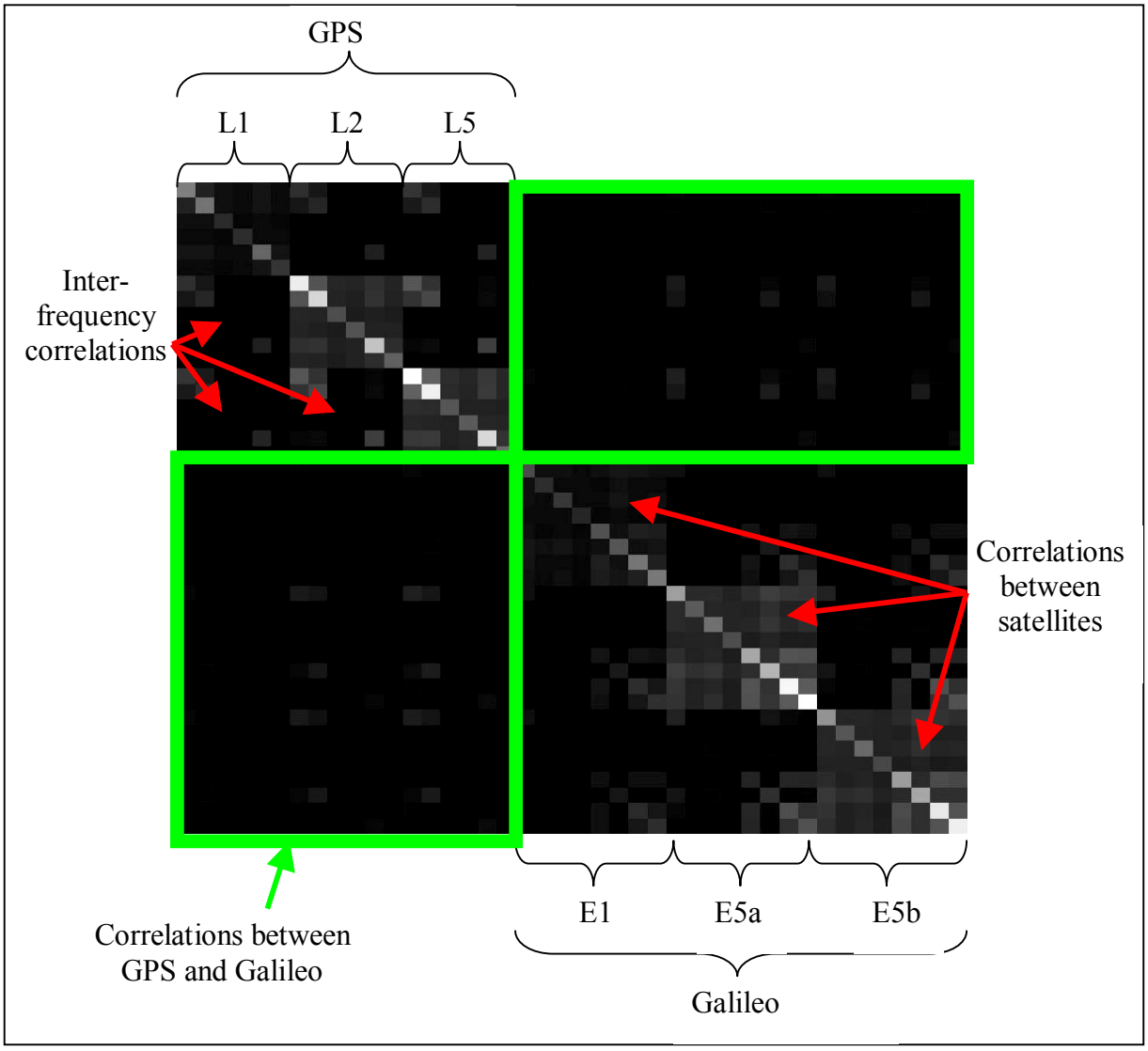

Figure 2.5: Carrier Phase Measurement Covariance Matrix for GPS/Galileo Triple-Frequency Data

Visual inspection of the covariance matrices pictured above reveal that the diagonal contains the largest values and the correlations between satellites have the second largest

values. The correlations between frequencies are less significant and the correlations between GPS and Galileo measurements are the least significant. This is why these latter two types of correlations are often ignored in commercial GNSS processing software.

2.1.2.3 Temporal Correlations

An unresolved problem in GNSS processing is how to model the temporal correlation of the measurements. One of the basic assumptions in using a Kalman filter is that the measurements should not be correlated in time (Brown et al. 1992). As a result, the temporal correlations are commonly ignored, which is why the state covariance matrix becomes grossly optimistic in most commercial GPS processing software systems. Several researchers have proposed approaches for dealing with the temporal correlations in static GPS positioning including Wang et al. (2002), El-Rabbany (1994), and Radovanovic (2002). However, in kinematic applications using a Kalman filter, the temporal correlations must be removed from the measurements by including time varying parameters in the functional model. This is rarely done in practice because the disadvantages (the increase in dimension of the state vector and the decrease in the speed of convergence) outweigh the advantages (a more accurate state covariance matrix). As a result the temporal correlations are generally neglected. El-Rabbany (1994) found that the effect of temporal correlations is essentially a scaling of the state covariance matrix

and according to Han et al. (1995), the state estimation results are not significantly affected by the scale of the covariance matrix. Based on these studies, the temporal correlations of the GNSS observations have been neglected in this thesis, which is consistent with most other academic and commercial GNSS processing algorithms.

2.2 Dynamic Model for Simulated GNSS Positioning

The dynamic model is the model that propagates the unknown parameters and the associated covariance matrices from one epoch to the next. The generic functional part of the dynamic model is given by,

$$x_{k+1/k} = \Phi_k x_{k/k} + \omega_k \qquad (2.37)$$

where $x_{k+1/k}$ is the predicted state vector at epoch $k+1$, $x_{k/k}$ is the updated state vector from epoch k, Φ_k is the state transition matrix that relates these two vectors, and ω_k is a random white noise sequence whose mean is zero and is approximated with a Gaussian distribution.

The stochastic part of the dynamic model is derived by applying the error propagation law to Equation (2.37) to produce,

$$P_{k+1/k} = \Phi_k P_{k/k} \Phi_k^T + Q_k \qquad (2.38)$$

where $P_{k/k+1}$ is the covariance matrix of the predicted state vector, $P_{k/k}$ is the covariance matrix of the updated state vector from epoch *k*, and Q_k is the process noise covariance matrix that describes the uncertainty in the dynamic model. For further details, the reader is referred to Brown et al., 1992.

2.2.1 State Transition for Simulated Measurements

The state transition employed for the mechanization that is used in this thesis is somewhat trivial. Since the state vector contains *corrections* to the position, ionospheric delays and ambiguities, rather than the actual position, ionospheric delays and ambiguities, and since a zero velocity model is assumed, the predicted state vector is simply the appropriately dimensioned null vector. At the end of each cycle of the Kalman filter, the corrections contained in the state vector are applied to the positions, ionospheric delays, and ambiguities. Since the velocity of each of the states is assumed to be zero, the predicted corrections for the next epoch are simply zero. Mathematically, this is represented by:

$$\delta x_{k/k} = 0 \qquad (2.39)$$
$$\delta \dot{x}_{k/k} = 0$$
$$\delta x_{k+1/k} = \delta x_{k/k} + \delta \dot{x}_{k/k} \Delta t + \omega_k = 0$$

The difference between kinematic and static positioning is expressed in the variance of the white noise sequence, ω_k, which is discussed in Section 2.2.2.1.

2.2.2 Process Noise

The uncertainty of the state propagation is described by the process noise matrix, which will be discussed in the following sections for each type of state.

2.2.2.1 Position States

The focus of this research is on kinematic positioning, so the simulated data used in the experiments is treated as if it were from a kinematic user. This is done by adding uncertainty to the predicted position states, which is the same as increasing the variance of the random noise sequence, ω_k. A process noise of 0.5 metres/second (1σ) is used because this is the approximate position accuracy that could be obtained from a typical differential code solution. In other words, at each epoch, the estimate of the position resembles the accuracy that would be obtained using only the code observations for that

epoch. This is a good approximation of a real system that uses a fast code-based solution as an initial approximate for the carrier phase processing.

2.2.2.2 Ambiguity States

The carrier phase ambiguities are constant with time, so no process noise is added to the dynamic model for these states. The uncertainty in the ambiguity states originates from the measurement noise.

2.2.2.3 Ionospheric Delay States

The ionospheric delay states change slowly over time so there is some uncertainty in the dynamic model. In this research, the ionospheric states have been modeled as random walk processes after Odijk (2001) and Julien (2004). Julien (2004) suggests a process noise variance of $Q_{iono} = \left[\left(2 \cdot 10^{-7}\right) \cdot \left(BaselineLength\right)\right]^2 \otimes I$ metres^2 where I is an appropriately dimensioned identity matrix. In this research, the same strategy has been used to model the ionospheric delays.

2.3 Estimation Technique

A Kalman filter estimation algorithm has been used to estimate the unknown states in a sequential fashion. This technique combines the measurement model of Section 2.1 with the dynamic model of Section 2.2 to generate optimal estimates of the state vector at each epoch. Like standard least squares estimation, the Kalman filter is based on an optimality criterion of minimizing the squared estimation residuals. The state vector for the current epoch is predicted based on the dynamic model and the previously estimated state vector. It is then updated using the measurement model and the satellite measurements. As time and data accumulates, the covariance of the estimated state vector converges to the steady state precision of the system. For a more detailed discussion of Kalman filtering, the reader is referred to Brown et al. 1992. The basic Kalman filter equations are well known and are included below in Figure 2.6 for completeness.

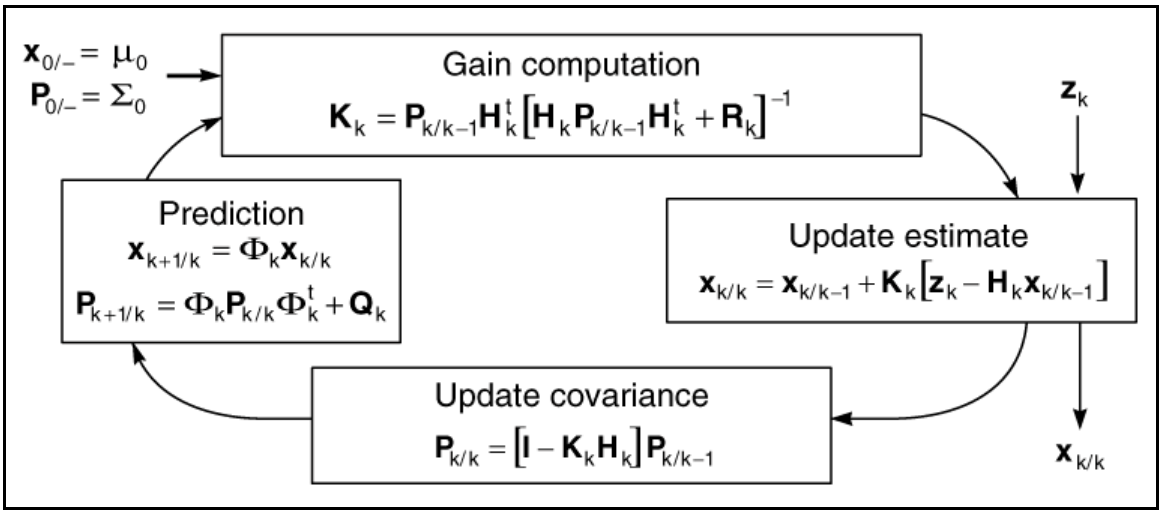

Figure 2.6: Kalman Filter Equations (from Brown et al. 1992)

The Kalman filter estimation technique considers all the unknown parameters in the state vector to be real numbers and is useful for solving the float-valued solution. With carrier phase GNSS data, the initial ambiguity biases are integers by definition and this information can be used to constrain the ambiguities, which improves the precision of the remaining parameters. The process of determining the correct integer values for the ambiguity parameters is called ambiguity resolution and is the topic of Chapter Five.

2.4 Summary

This chapter has described the details of the functional and stochastic components of the measurement and dynamic math models to be used with future global navigation satellite systems, which is a fulfillment of the first minor objective of the thesis. The heterogeneous and homogeneous double differencing schemes for GPS and Galileo measurements were explained and the treatment of ionospheric delays as estimable states was described. In addition, the correlations between future observation types, between future frequencies, and between epochs in time were addressed. The equations and algorithms developed in this chapter have been implemented in newly developed software and will be used in the remainder of the thesis to process simulated future measurements.

Chapter Three: GNSS Simulation and Processing Software

This chapter endeavours to describe the software that was developed to generate and process simulated future GNSS measurements. The software consists of two major components as shown in Figure 3.1.

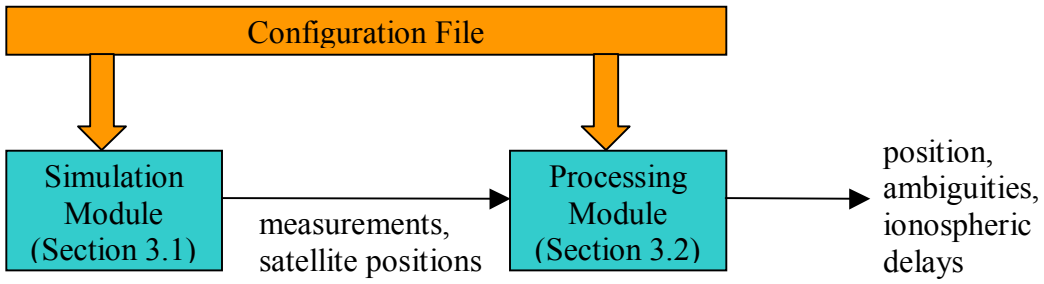

Figure 3.1: General Schematic of Developed Software

First is the simulation module, which is based on a commercially available software simulator. The simulation module is described in detail in Section 3.1. The second major component is the processing module. The mathematical theory behind the processing module was explained in Chapter Two and a schematic diagram and description of the processing module is given in Section 3.2. Both of these modules are controlled by a configuration file in which the user specifies the details of the simulated positioning campaign. The configuration file includes commands to control:

- the location of the base and rover receivers
- the start and end times of the campaign
- the levels of the error sources (low, moderate, high)
- the dynamics mode of the receivers (static or kinematic)
- standard deviations and correlation lengths for the measurement covariance model
- the type of tropospheric model
- the types of observations to use
- the combination coefficients for creating linear combinations of carrier phase data
- the standard deviation of the ionospheric pseudo-observation
- the measurement sampling interval
- the critical value for the ambiguity discrimination test
- the types of output to be recorded in the output files

3.1 Future GNSS Measurement Simulation

The simulator used for the tests described in this research is derived from the Satellite Navigation TOOLBOX 3.0 For MATLAB® developed by GPSoft®. The simulator is able to emulate both GPS and the predicted Galileo orbits. For GPS satellites, there are six orbital planes with four satellites on each plane; for Galileo, there are three orbital planes with 10 satellites equally spaced on each plane, three of which act as spares. The measurements from GPS and Galileo are transmitted on a total of four frequencies as

summarized in Table 3.1. This corresponds to the current plans for the Galileo constellation according to the Galileo Mission High Level Document (2002).

Table 3.1: Carrier Frequencies used for Future Global Navigation Satellite Systems

Carrier Signal	Frequency (MHz)
GPS L1	1575.45
GPS L2	1227.60
GPS L5	1176.45
Galileo E1	1575.42
Galileo E5a	1176.45
Galileo E5b	1207.14

As shown in Figure 3.2, the satellite signals are simulated as perfect geometric ranges corrupted by the ionospheric delay, tropospheric delay, multipath, thermal noise, and an integer number of cycles for the carrier phase measurements. All other sources of error that exist in the GNSS positioning environment have been neglected because the magnitudes of these error sources after double differencing are insignificant. Each of the included error sources are described in more detail in the following sections.

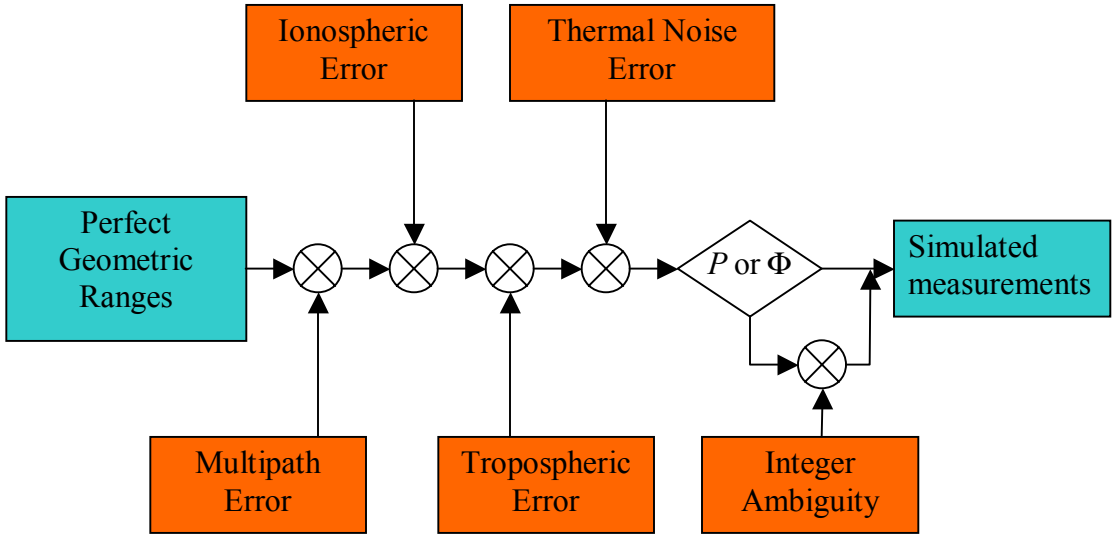

Figure 3.2: Measurement Simulation Diagram

3.1.1 Ionosphere

The ionosphere is modeled using "the traditional raised half-cosine profile for zenith delay" and "scaled by the FAA [Federal Aviation Administration] Wide Area Augmentation System obliquity factor." (Satellite Navigation TOOLBOX User's Guide). The raised half-cosine profile for zenith delay is described in Klobuchar (1996) and is the same model that is used for the broadcast ionospheric correction transmitted by GPS satellites. The obliquity factor scales the ionospheric errors according to elevation angle and is described in Kaplan (1996). The resulting ionospheric delay over the period of one day for a medium level of ionosphere is shown in Figure 3.3. In this figure, each curve represents a satellite pass.

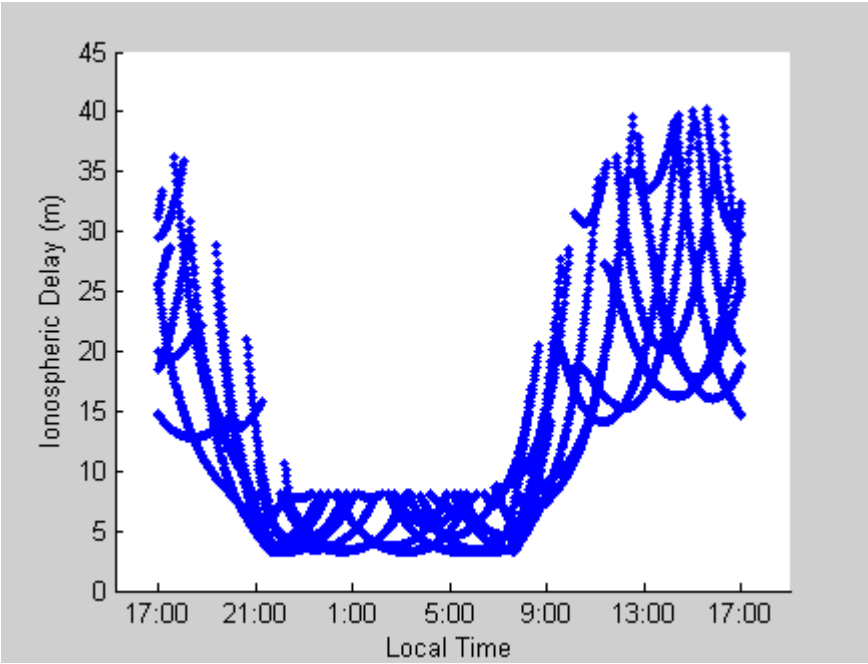

Figure 3.3: Medium Level Ionospheric Delay for 24 Hour Period

The ionospheric delay also varies with elevation angle between the user and satellite. This variation is shown in Figure 3.4 where the magnitude of the ionospheric correction is plotted against elevation angle for a variety of times of the day.

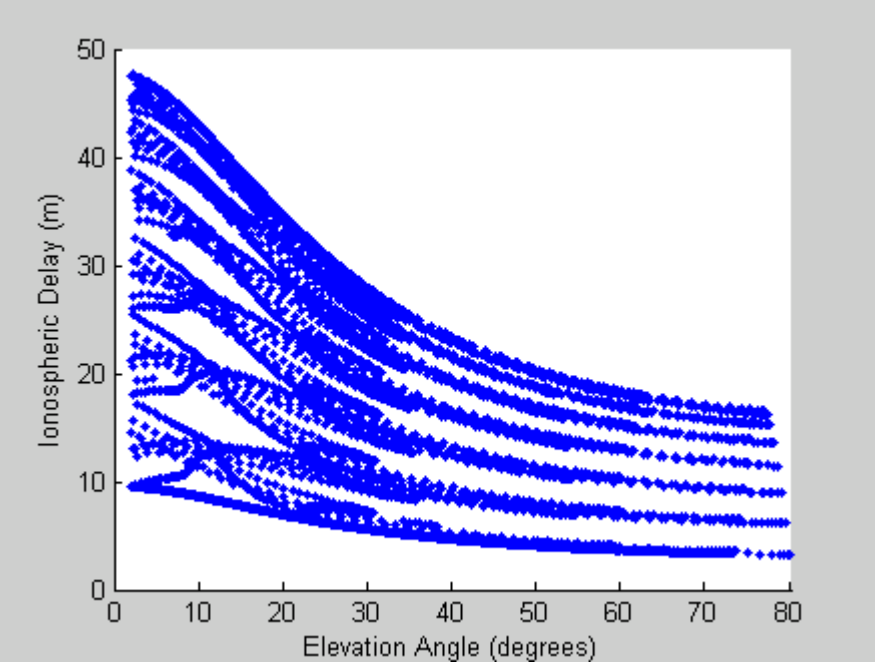

Figure 3.4: Medium Level Ionospheric Delay versus Elevation Angle

The errors shown in Figure 3.3 and Figure 3.4 are the errors applied to a single range measurement. For the experiments conducted in this investigation, the double differencing process was employed. Therefore, the effect of the error sources on the double-differenced measurement is of prime importance. Figure 3.5 shows the resulting double-differenced ionospheric error versus baseline length for a north-south oriented baseline. Since the zenith ionospheric delay has a high degree of spatial correlation, the main effect of the double-difference ionospheric error comes from the difference in mapping function between the two receivers.

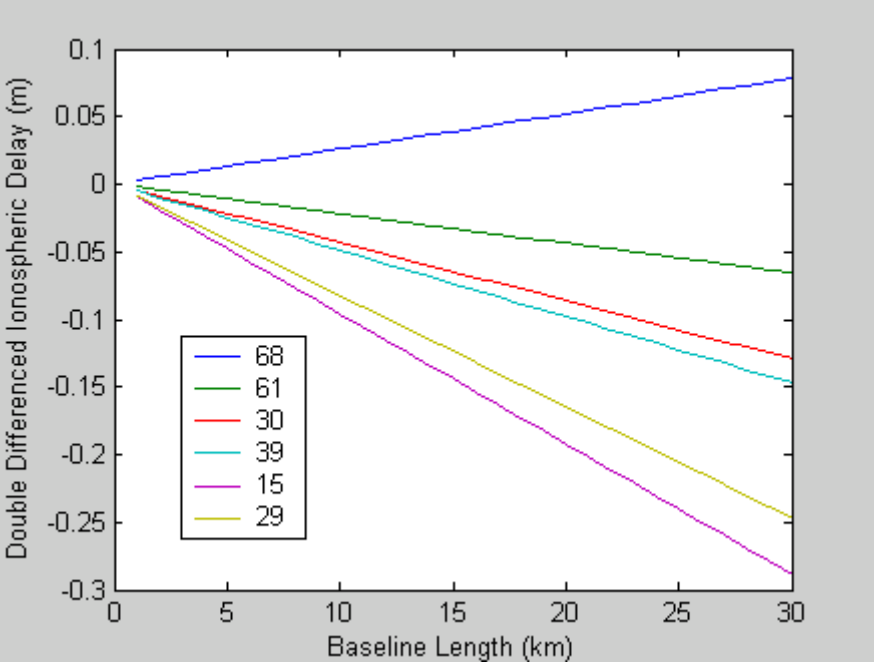

Figure 3.5: Medium Level of Double-Differenced Ionospheric Delay versus Baseline Length

3.1.2 Troposphere

The tropospheric error model uses the modified Hopfield model which is given in Goad et al. 1974. This error is not dependent on time of day, but rather on the percent humidity in the atmosphere and the elevation angle of the satellite. Figure 3.6 shows the resulting tropospheric delay versus humidity for a low elevation and a high elevation angle satellite.

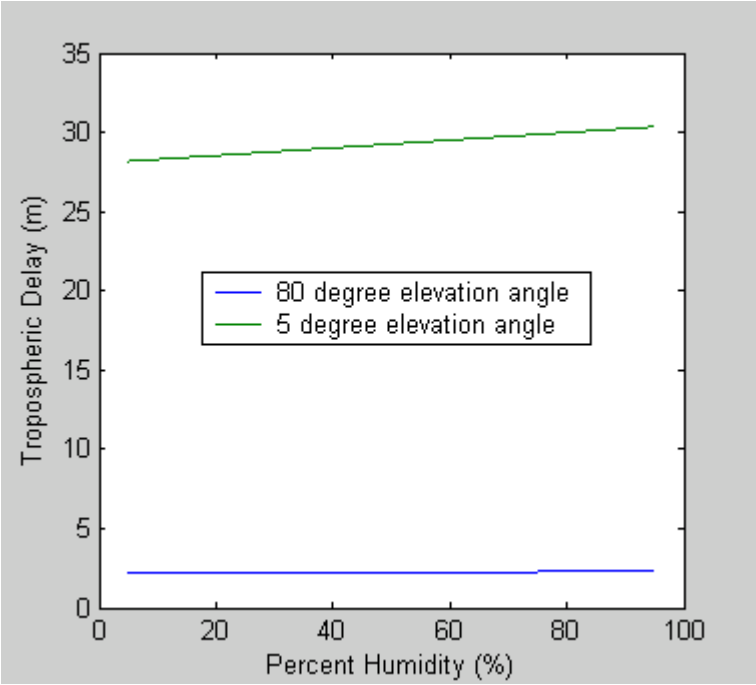

Figure 3.6: Tropospheric Delay versus Humidity for Satellites with 5 and 80 Degree Elevation Angles

According to Parkinson et al. (1995) simple tropospheric models can typically remove 90% of the undifferenced tropospheric delay. Therefore, in this research, the applied tropospheric delay is scaled by a factor of 0.1 and no tropospheric correction is applied. This technique simulates a typical residual tropospheric delay that would remain after applying a standard tropospheric correction model.

For the experiments performed in this research, the humidity was fixed at the typical value of 50%. Similar to the ionospheric error, the double-differenced tropospheric error

is mostly dependent on elevation mapping function. The double-differenced tropospheric error for a north-south oriented baseline is shown in Figure 5.

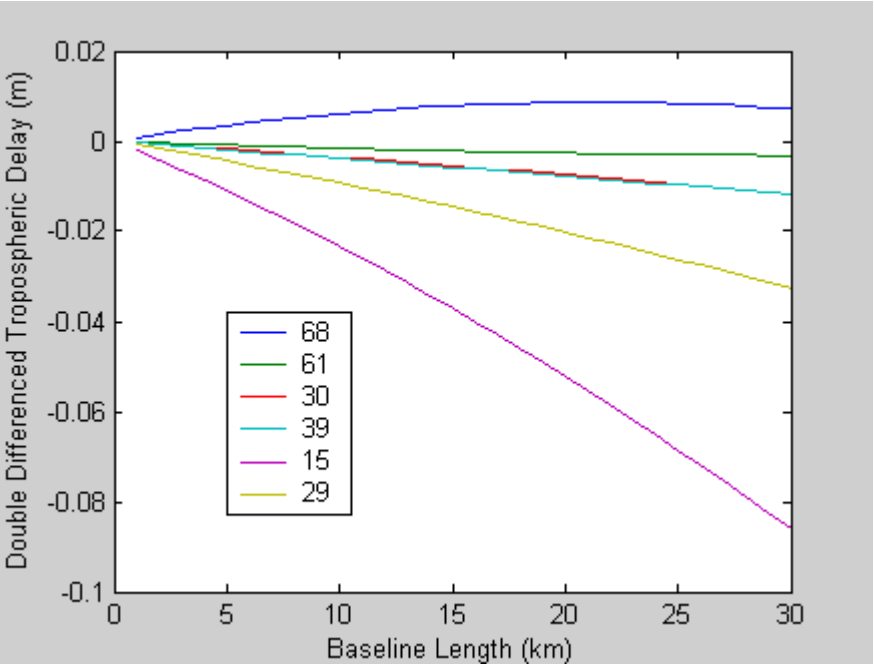

Figure 3.7: Medium Level of Double-Differenced Tropospheric Delay versus Baseline Length (Elevation angle shown in legend box)

3.1.3 Thermal Noise

The thermal noise component of the ranging error is modeled a random white noise sequence with mean zero and standard deviation depending on the type of measurement being simulated. In reality, the precision of the measurements depends on the bandwidth and quality of the receiver used; however, in this simulation, a high quality receiver has

been assumed because the focus of this research is on precise carrier phase positioning. The following table describes the thermal noise characteristics of the various signals used. The values chosen are in the same range as other simulations and predictions of future receiver noise precision (e.g. Alves 2001 and Hein et al. 2002).

Table 3.2: Thermal Noise Standard Deviations for Various Measurement Types

Measurement Type	Standard Deviation (m)
GPS C/A code	0.40
GPS L2C code	0.10
GPS L5 code	0.10
Galileo E5a code	0.08
Galileo E5b code	0.10
All Carrier Phase Measurements	0.01*Wavelength

3.1.4 Multipath

The effect of multipath signals is modeled by adding random time correlated noise. The zero-elevation angle multipath error is generated using a digital filter described by Equation (3.1). This multipath error is then scaled according to the elevation angle of the satellite so that lower elevation angle satellites have a greater multipath effect.

$$y(n) = \sum_{i=0}^{N} a_i x(n-i) - \sum_{i=1}^{N} b_i y(n-i) \qquad (3.1)$$

where y is the output sequence, x is an input Gaussian white noise sequence (mean zero and standard deviation σ_e) and a and b are the feed-forward and feed-back filter coefficients respectively. Two different filter models were chosen to represent different multipath signals: a short-time constant model and a long time constant model. Given the representation in Equation (3.1), the two models are implemented with the coefficients outlined in Table 3.3.

Table 3.3: Multipath short and long time constant coefficients

	N	σ_e (m)	b(0)	b(1)	a(0)	a(1)
Short-time constant	1	2	1.0000	-0.9244	0.0378	0.0378
Long-time constant	1	15	1.0000	-0.9782	0.0109	0.0109

For both models, the order of the filter is one, which means that the multipath errors are correlated in time. A different uncorrelated multipath error is generated for each measurement to ensure that the multipath errors will not cancel in the double differencing process. The multipath error for carrier phase observations was generated in the same way as the code multipath and then multiplied by a factor of $0.005 \cdot \lambda$, where λ is the

wavelength of the signal. The filter coefficients shown in Table 3.3 come from the Satellite Navigation TOOLBOX 3.0 For MATLAB® where they were chosen empirically according to realistic levels of resultant multipath errors. Figure 3.8 and Figure 3.9 show the pseudorange multipath error for a low elevation angle satellite and a high elevation angle satellite respectively.

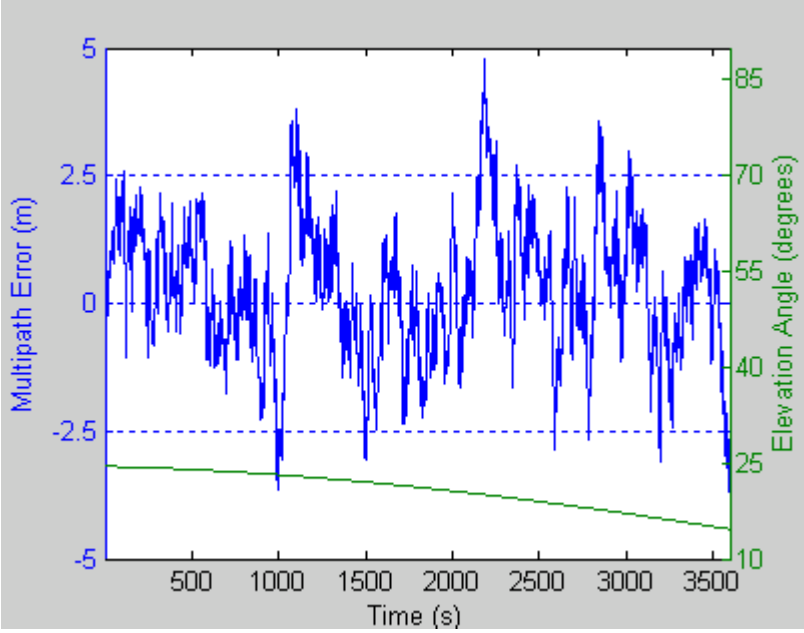

Figure 3.8: Pseudorange Multipath Error for a Low Elevation Satellite

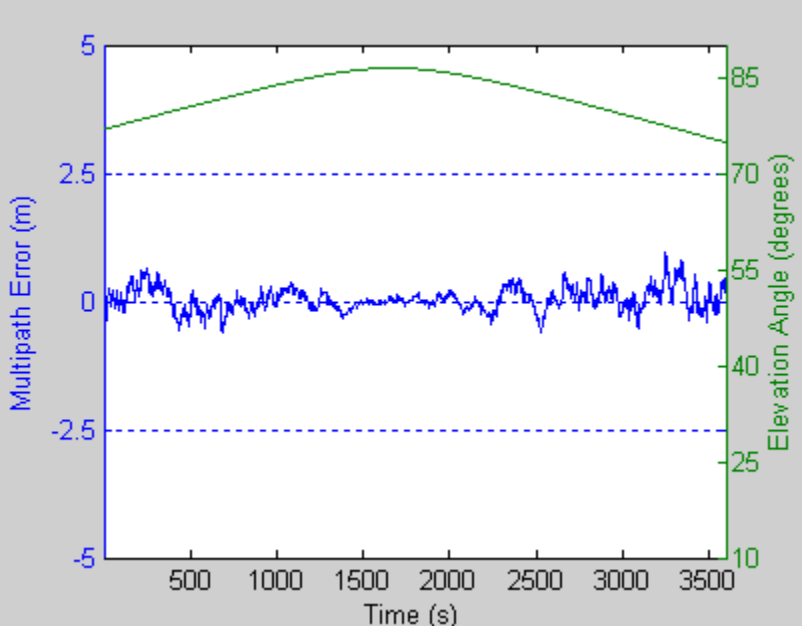

Figure 3.9: Pseudorange Multipath Error for a High Elevation Satellite

3.2 Processing Software

The mathematical theory used in processing future GNSS measurements was described in Chapter Two. This section describes the architecture of the processing software that is used to process the simulated futuristic measurements. A general schematic diagram of the processing module is provided in Figure 3.10.

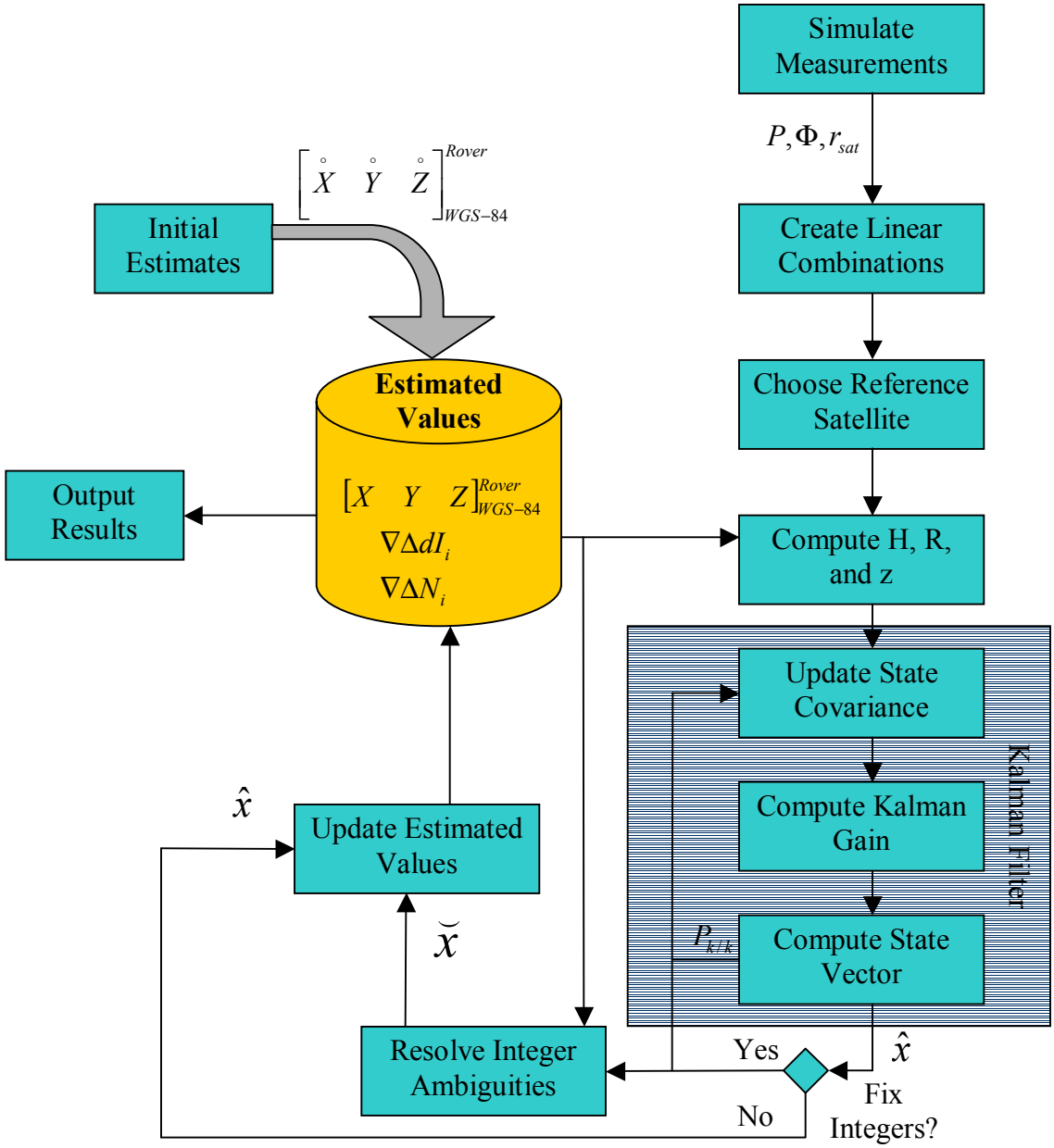

Figure 3.10: GNSS Simulation and Processing Software

Figure 3.10 shows that there is a storage container that holds the estimated values. These values are initialized by the "initial estimates" task, and then updated at each epoch with one of two state vectors from the Kalman filter. If the user desires to fix the ambiguities to integer values, the fixed state vector ($\breve{x}$) is applied to the estimated values; otherwise, the float state vector ($\hat{x}$) is applied to the estimated values. Each of the specific tasks illustrated in the figure are described in more detail below.

Initial Estimates

This task is performed only once at the beginning of a data set. The initial estimates of the rover's position are provided by the user. The initial estimates for the carrier phase ambiguities and the ionospheric delays are simply set to zero.

Simulate Measurements

This task uses the simulated orbital parameters and the locations of the receivers to compute simulated pseudorange and carrier phase measurements and the coordinates of the satellites in the WGS-84 reference frame. The user has control over the level of the various error sources that are applied to the measurements and the measurement sampling rate. The details of this process are given in Section 3.1.

Create Linear Combinations

This task takes the raw measurements from the simulator module and forms user specified linear combinations of the original observations. The linear combinations are formed with the following equation:

$$\phi_* = B\phi \qquad (3.2)$$

where ϕ_* is the vector of transformed observations, ϕ is the original vector of observations, and B is the transformation matrix. The user defines the transformation matrix, B, in the configuration file. A detailed discussion of linear combinations of signals is given in Chapter Six.

Choose Reference Satellite

Since the quality of the measurements from the reference satellite contributes to the overall quality of each double difference, it is desirable to select a reference satellite with measurements that are the least corrupted by errors. To this end, the satellite with the highest elevation is selected as the reference satellite since its transmission path through the ionosphere and troposphere will be a minimum of all the satellites.

Compute H, R, and z

In this task, the matrices required in the Kalman filter algorithm are computed. The design matrix, H, is shown in Equation (2.13), the measurement covariance matrix, R, is

shown in Equation (2.36), and the measurement or misclosure vector, *z*, is shown in Equation (2.11). These matrices are computed using the most current estimates of the estimated values. This technique is called extended Kalman filtering since the point of linearization for each epoch is the most recent estimate of the estimated values. Because of this mechanization, the state vector of corrections is set to the null vector at the beginning of each epoch.

Update State Covariance

This task implements the time propagation of the state covariance matrix. The equation that is computed is given as Equation (2.38) and is repeated here for clarity:

$$P_{k+1/k} = \Phi_k P_{k/k} \Phi_k^T + Q_k \qquad (2.38)$$

The user is able to control whether the processing should be done in static or kinematic mode. In static mode, there is no process noise for the position states; whereas, in kinematic mode, the process noise for the position states are set to 0.5 metres/second as explained in Section 2.2.2.1. Regardless of the mode selected for the user dynamics, the process noise for the ambiguities is set to zero and the process noise for the ionospheric delay states are set to $Q_{iono} = \left[\left(2 \cdot 10^{-7}\right) \cdot \left(BaselineLength\right)\right]^2 \otimes I$ as described in Sections 2.2.2.2 and 2.2.2.3.

Compute Kalman Gain

In this task, the updated state covariance matrix, the current measurement covariance matrix, and the current design matrix are used to compute the Kalman gain. This is accomplished using the standard Kalman gain equation, which is found in Figure 2.6 and repeated here for clarity:

$$K_k = P_{k/k-1} H_k^T \left[H_k P_{k/k-1} H_k^T + R_k \right]^{-1} \qquad (3.3)$$

where the subscript k refers to the epoch.

Compute State Vector

In this task, the state vector of corrections is computed using the misclosure (or measurement vector), the Kalman gain matrix, and the design matrix. Again, the equation is found in Figure 2.6 and repeated here for clarity:

$$x_{k/k} = x_{k/k-1} + K_k \left[z_k - H_k x_{k/k-1} \right] \qquad (3.4)$$

However, since the extended Kalman filter algorithm is used, the state vector of corrections is reset to the null vector at the beginning of every epoch. Therefore, $x_{k/k-1}$ is null and Equation (3.4) is simplified to

$$x_{k/k} = K_k \cdot z_k \qquad (3.5)$$

At this point, there is no consideration of the integer nature of the ambiguity states and the state vector contains corrections for real-valued carrier phase ambiguities.

Resolve Ambiguities

This task attempts to apply an integer constraint to the carrier phase ambiguities. The float valued state vector and its associated covariance matrix are passed into the task along with the most recent estimated values. If integer ambiguities can be found and validated with a user-defined level of confidence, the state vector is modified to reflect the integer nature of the ambiguities. The details of finding and validating integer ambiguities are provided in extensive detail in Chapter Five.

Update Estimated Values

In this task, the estimated values are updated with the new state vector. If integer ambiguities were found, the estimated values are updated with the fixed state vector; otherwise, the float state vector is used. This is described by the following equation where subscript, $i = 1...n$, indicates the satellite pair.

$$\begin{bmatrix} X_{WGS-84}^{Rover} \\ Y_{WGS-84}^{Rover} \\ Z_{WGS-84}^{Rover} \\ \nabla\Delta dI_i \\ \nabla\Delta N_i \end{bmatrix}_k = \begin{bmatrix} X_{WGS-84}^{Rover} \\ Y_{WGS-84}^{Rover} \\ Z_{WGS-84}^{Rover} \\ \nabla\Delta dI_i \\ \nabla\Delta N_i \end{bmatrix}_{k-1} + \begin{bmatrix} \delta x \\ \delta y \\ \delta z \\ \delta\nabla\Delta dI_i \\ \delta\nabla\Delta N_i \end{bmatrix}_{\substack{\text{float or} \\ \text{fixed}}} \quad (3.6)$$

Output Results

This task handles the output of various user-requested results. Each requested type of output is stored in a different file with the same prefix, but different file extensions. The available output files are listed in Table 3.4.

Table 3.4: Output File Types

File Extension	File Description
.fwd	Rover position and the associated variance in the WGS-84 reference frame.
.fml	Any output messages for the user. For example, notifications when the reference satellite is changed, details of the ambiguity resolution process, warnings when filter resets occur, etc.
.amb	The estimated double differenced ambiguities for each satellite pair.
.ion	The estimated double differenced ionospheric delays for each satellite pair.

.res	The measurement residuals.
.kmo	The Kalman matrices computed at each epoch.

3.3 Summary

Chapter Three has described the commercially available simulator that has been used in this thesis to generate simulated future GNSS measurements. The theory used in generating the error sources has been explained and examples of the error sources under typical conditions have been given. In addition, the software that has been developed for processing the future GNSS signals was explained. This chapter has described the accomplishment of the fifth objective of the thesis and the software portrayed herein has been used to fulfil the remaining objectives of the thesis.

Chapter Four: The Effect of Future Signals on Ionospheric Delay Estimation

One of the major obstacles in resolving ambiguities for longer baselines is the presence of unmodeled ionospheric delays. With baselines that are longer than 10 kilometres, the ionospheric transmission delays become a major source of error that will prevent reliable ambiguity resolution, which ultimately results in poorer baseline precision.

Traditionally, the ionosphere has been dealt with in one of three ways: it can be ignored, it can be eliminated using dual-frequency measurements, and it can be modeled as a state.

When the ionospheric delay is ignored, the double difference carrier phase observation becomes

$$\nabla\Delta\Phi_{Li} = \nabla\Delta\rho + \lambda_{Li}\nabla\Delta N_{Li} \qquad (4.1)$$

where the notation of Chapter Two has been used and subscript *Li* refers to the carrier frequency. Ignoring the ionospheric delay is a reasonable assumption for short baselines where the effect of the ionosphere is effectively eliminated through the process of double differencing. In this case, even when the ionospheric activity is high, the impact of this unmodeled error can be compensated for by increasing the noise in the measurement covariance matrix. However, the ionosphere can only be ignored to an extent. For

baselines longer than a few kilometres, this source of error causes too much disturbance to be ignored.

The second technique that is commonly used with longer baselines is to eliminate the ionosphere through ionosphere-free combinations of data. It is known that the effect of the ionosphere is inversely proportional to the square of the carrier frequency (Hofmann-Wellenhof et al. 2000) as shown in Equation (2.26). Therefore there are linear combinations of data that can completely eliminate the ionospheric delay. The observation equation for an ionosphere-free combination of dual-frequency GPS carrier phase data is given by (Collins, 1999):

$$\begin{aligned} \nabla\Delta\Phi_{IF} = \lambda_{IF}\nabla\Delta\phi_{IF} &= \lambda_{IF}\left(77\cdot\nabla\Delta\phi_{L1} - 60\cdot\nabla\Delta\phi_{L2}\right) \\ &= \nabla\Delta\rho + \lambda_{IF}\left(77\cdot\nabla\Delta N_{L1} - 60\cdot\nabla\Delta N_{L2}\right) \end{aligned} \qquad (4.2)$$

where

$$\lambda_{IF} = \left(\frac{77}{\lambda_{L1}} - \frac{60}{\lambda_{L2}}\right)^{-1} \approx 6.3 \quad mm \qquad (4.3)$$

Unfortunately, when ionosphere-free combinations of data are used, the measurement noise is greatly increased, which can degrade the baseline precision. In addition, the wavelength of the resulting carrier beat signal is so short that resolving integer ambiguities becomes all but impossible for short observation time spans. Ionosphere-free combinations are discussed in further detail in Chapter Six.

The third way to deal with the ionosphere is to model the ionospheric delay as an estimable state as shown in the mathematical models of Chapter Two. This third technique is more versatile in the sense that it works well for both short and long baselines and it improves the ability to resolve integer ambiguities. Ionospheric modeling in light of future GNSS signals is the topic of this chapter.

Section 4.1 will explain the three available weighting schemes when using the ionosphere weighted model. In order to emphasize the effects of the various weighting schemes, the type of measurements used is kept constant. Simulated triple frequency GPS data is used to provide test results using the different weighting schemes. After demonstrating the nuances of ionospheric weighting on the triple frequency GPS case, the discussion can be generalized to include other positioning scenarios. Section 4.2 shows how future GNSS measurements will impact the ability to estimate the ionospheric delay states.

4.1 Weighting of the Ionospheric Pseudo-Observation

There are generally three choices of how to weight the ionospheric pseudo-observation: ionosphere-fixed, ionosphere-weighted and ionosphere float (Odijk, 2002). These three categories are summarized in Table 4.1.

Table 4.1: Weighting Schemes for the Ionospheric Pseudo-Observable

Variance of Ionospheric Pseudo-Observable	Model Description
$\sigma^2_{pseudo-observable} = 0$	Ionosphere-Fixed
$0 < \sigma^2_{pseudo-observable} < \infty$	Ionosphere-Weighted
$\sigma^2_{pseudo-observable} \to \infty$	Ionosphere-Float

According to the ranges of the ionospheric pseudo-observation variances shown in Table 4.1, the fixed and float ionosphere models are special cases of the more general ionosphere weighted model. The ionosphere-fixed model constrains the ionospheric state to a constant value. In many dual-frequency GPS applications, particularly short baseline applications, the ionospheric delay is not estimated as a state, but is neglected. In these cases, the ionosphere-fixed model is used implicitly. The advantages of the ionosphere-fixed model are that it is simple to implement, the dimension of the state vector is reduced, and there is no risk of the ionospheric state diverging. The disadvantage is that the model will not fit the observations for long baselines and/or high levels of ionospheric activity. The ionosphere-float model performs well when long observational time spans are used, but without an external observation, the ionospheric state is highly correlated with the carrier phase ambiguities causing slow convergence or in some cases divergence

of the state vector. The ionosphere-weighted model converges more quickly than the float model because it is initially constrained by the ionospheric pseudo-observation. After convergence, the ionospheric states are allowed to change with the changing level of ionospheric activity, which allows the model to fit the observations more accurately. However, the weighted model has the disadvantage of requiring a suitable variance for the pseudo-observable. Alves (2002) found that choosing a suitable value for the variance of the pseudo-observation in the ionosphere-weighted model is crucial for reliable ambiguity resolution.

For a more thorough explanation of the treatment of ionospheric delays in GPS processing, the reader is referred to Odijk (2002). The remainder of this section demonstrates the difference between the float, fixed and weighted ionosphere models for a short and a long baseline using triple frequency GPS data.

4.1.1 Ionospheric Weighting Schemes for Short Baselines

One hour of triple frequency simulated GPS data from a one kilometre baseline was processed with a sampling interval of five seconds. The same baseline was processed using the float, fixed and weighted ionosphere models. For the weighted model, a zenith standard deviation of 0.7 metres was used for the ionospheric pseudo-observation, while the code observations (L2C and the L5 civil code) were given standard deviations of 0.1

metres. Figure 4.1 shows the resulting carrier phase residual RMS when using the three ionosphere models. For a short baseline, there is little difference in the resulting carrier phase residuals because the spatial correlation of the ionosphere at this baseline length is high. Consequently, the effect of the ionosphere is mostly eliminated through the process of double differencing.

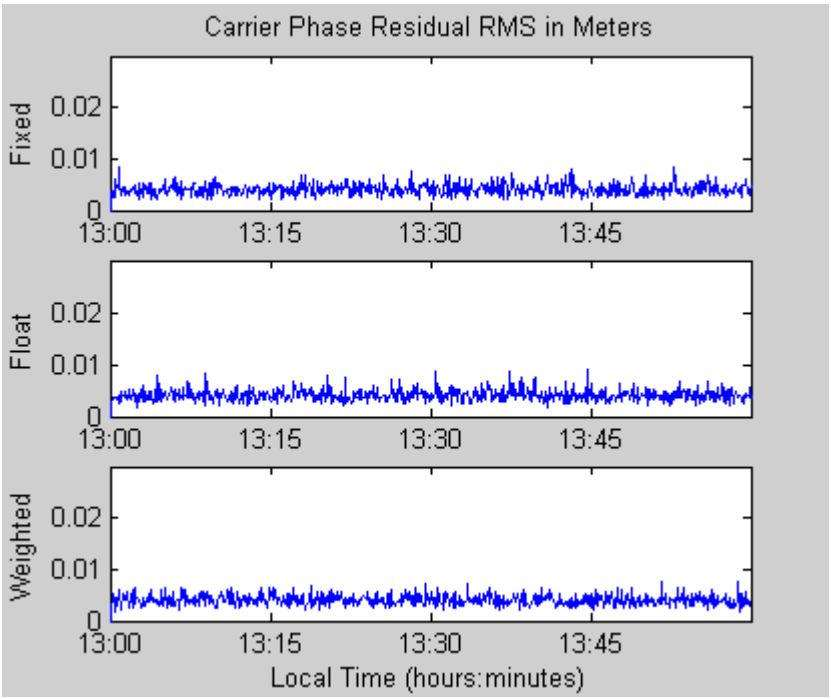

Figure 4.1: Carrier Phase Residual RMS Using the Fixed (top), Float (middle), and Weighted (bottom) Ionosphere Models for a 1 km Baseline

Figure 4.2 presents the root-mean-square estimation error for the ionospheric states. The float ionosphere model has large estimation errors at the beginning of the data set because

there is no prior information about the ionospheric states. Therefore, about 10 minutes of data is required before the ionospheric states are able to converge to an accurate value of the true ionospheric delay. A small spike is seen in the float model ionosphere estimation error at 13:47. This is an epoch where a new satellite came into view. Since the new satellite has no prior information about the ionospheric delay, the ionospheric estimation for that satellite will be poor until enough data has been accumulated to allow the state to converge.

The fixed and weighted ionosphere models both produce very accurate estimates for the ionospheric states because both of these models rely on the ionospheric constraint to estimate the ionospheric state. Since the ionospheric effect is spatially correlated, double differencing over a short baseline almost completely eliminates the ionospheric effect. As a result, the true value of the ionospheric delay state is close to zero. Since the ionospheric constraint equation constrains the ionospheric delay states to zero, the models that rely on this constraint will produce better results than the float model which relies more heavily on the noisy pseudorange measurements to estimate the ionospheric delays.

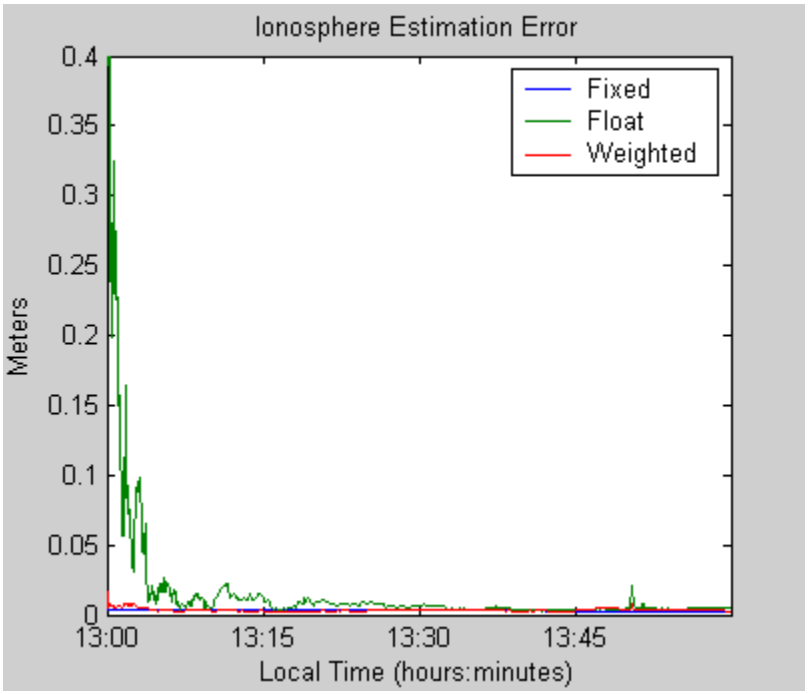

Figure 4.2: Ionospheric Estimation Error RMS for the Fixed, Float, and Weighted Ionospheric Models for a 1 km Baseline

Figure 4.3 shows the baseline errors when processing the short baseline with the three different ionosphere models. Clearly, the float ionosphere model is least precise at the beginning of the data set. Once again, this is because there is no prior information about the ionospheric states in the float model and a certain amount of data must be accumulated before they are able to converge. After convergence, all three of the models have comparable precision for the short baseline. The small spike seen in the ionospheric estimation RMS plot (Figure 4.2) is not seen in the position estimates (Figure 4.3) because the new satellite that became visible and caused the spike is sufficiently

deweighted in the parameter estimation procedure so that it does not negatively affect the state estimation.

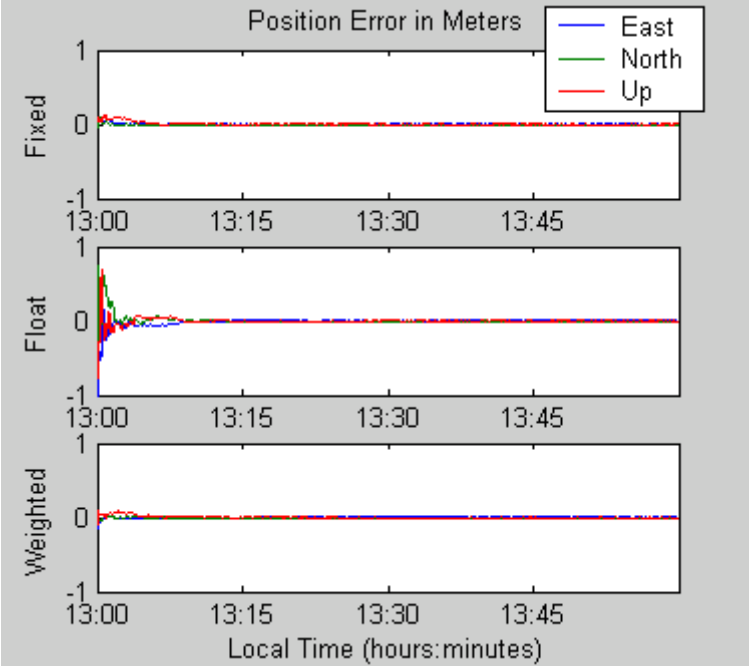

Figure 4.3: Baseline Error Using the Float (top), Fixed (middle), and Weighted (bottom) Ionosphere Models for a 1 km Baseline

In summary, for a short baseline where the ionospheric delay is mostly eliminated through double differencing, the best weighting scheme to use is the ionosphere fixed model. As the standard deviation of the ionospheric pseudo-observation increases, the ability to estimate the ionospheric delay worsens. In the next section, a similar analysis is performed for a longer baseline.

4.1.2 Ionospheric Weighting Schemes for Long Baselines

Using the same processing parameters as those used for the short baseline, a 30 kilometre baseline was processed. Unlike the short baseline results, the fixed model does not provide the best ionospheric estimation. Instead, the ionospheric estimation converges more accurately and quickly with an ionospheric pseudo-observation standard deviation that is greater than zero. Of course, this situation begs the question of what value to assign to the ionospheric pseudo-observation standard deviation. The smaller the value of the standard deviation, the more tightly the ionospheric states will be constrained to zero. The larger the standard deviation, the less the ionospheric states will rely on the constraint.

To demonstrate the effect of the standard deviation of the ionospheric pseudo-observable, the simulated 30 km baseline was processed using different values for the zenith standard deviation of the ionospheric pseudo-observation. Figure 4.4 shows the ionospheric estimation error root-mean-square results for various values of the ionospheric pseudo-observation standard deviation.

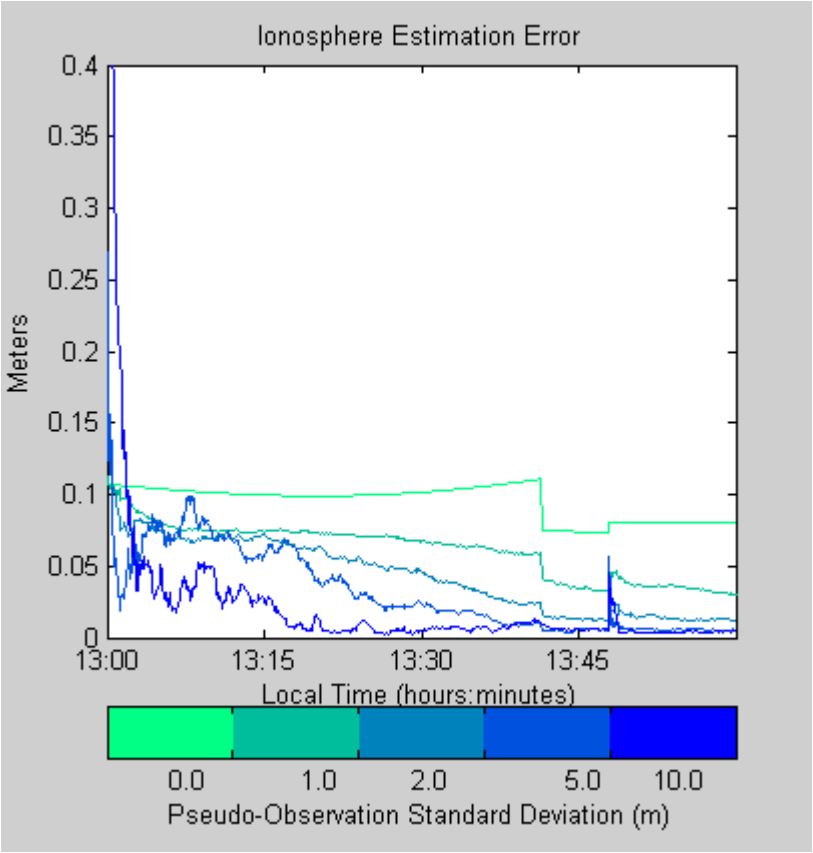

Figure 4.4: Ionospheric Estimation Error RMS Using Various Pseudo-Observation Standard Deviations for a 30 km Baseline (GPS3 Scenario)

The preceding plot clearly shows how the choice of weighting parameter for the ionospheric constraint affects the ionospheric estimation. The line with the largest standard deviation (darkest blue), which is very close to the float ionosphere model, achieves very poor ionospheric estimation at the beginning of the data set because it is relying solely on the noisy pseudorange measurements to observe the ionospheric delay. As more data is accumulated, the noisy code measurements are filtered and the satellite

geometry changes, which allows the ionospheric delays to decorrelate from the carrier phase ambiguities. Consequently, after a period of convergence, the float model relies almost exclusively on the more precise carrier phase data to observe the ionospheric delays, which results in very good ionospheric estimation. On the other end of the spectrum, the bright green line represents the ionosphere-fixed model. In this model, the initial ionosphere estimates are better than the initial ionosphere estimates of the float model because the estimates are constrained to zero, which is closer to the true value than the estimate from the noisy code data. However, as more data is accumulated, the ionospheric estimates are not allowed to converge according to the carrier phase data because of the constraint. This results in the poorest ionospheric estimation at the end of the hour-long data set. The lines that represent ionospheric standard deviations in between zero and 10 encapsulate the advantages of the fixed and float models to varying degrees.

The distinctive step seen in Figure 4.4 at 13:42 is the result of switching the reference satellite from a lower to a higher elevation satellite. The ionospheric delay in measurements from a satellite with a lower elevation angle is greater than the ionospheric delay in measurements from a satellite with a higher elevation angle. Since the measurements from the reference satellite are used in each of the double differences, the true values of the double differenced ionospheric delays are all larger when the reference satellite has a low elevation angle. As a result, constraining the ionospheric delays to

zero impairs the ionospheric delay estimation. When the reference satellite is switched to a satellite with a higher elevation angle, all the double differenced ionospheric delays are reduced in magnitude and the ionospheric constraint is more appropriate. This produces a marked improvement in the ionospheric delay estimation.

There is also an anomaly at 13:47 that is particularly accentuated for the lines with larger ionospheric pseudo-observation standard deviations. This event is the result of a new satellite coming into view. For the cases with the larger standard deviations, the new satellite has more erratic initial estimates; whereas, with the fixed and tightly constrained weighted ionosphere model, the initial ionospheric estimation for the new satellite is better.

Figure 4.5 shows the carrier phase measurement residual RMS for the 30 kilometre baseline. For this plot, the standard deviation of the ionospheric pseudo-observation was chosen to be 0.7. Unlike the short baseline, with a longer baseline, there is a significant difference in the measurement residual RMS when using the fixed ionosphere model versus the float and weighted models. With the fixed ionosphere model, the measurement residuals grow with time because the ionospheric states are tightly constrained to zero. As a result, the error in estimating the ionospheric states is propagated into the ambiguity estimation. Initially, this does not negatively affect the measurement residuals because the error in ionosphere and ambiguity estimates

compensate for one another to produce reasonable measurement residuals. However, as the ionospheric states change with time, they decorrelate from the ambiguities, which are constant over time. Therefore the errors in the ionosphere and ambiguity estimation cease to compensate for each other and the measurement residuals grow.

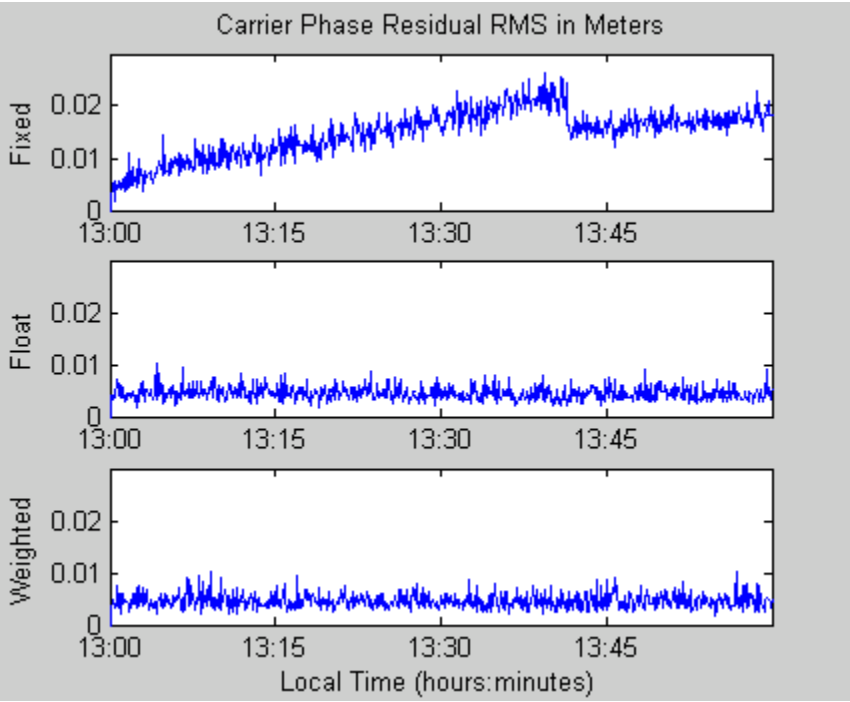

Figure 4.5: Carrier Phase Residuals Using the Float (top), Fixed (middle), and Weighted (bottom) Ionosphere Models for a 30 km Baseline

Figure 4.6 shows the position error using the fixed, float and weighted ionosphere models. Again, the standard deviation of the ionospheric pseudo-observation was set to

0.7. Neither the step at 13:41 from the reference satellite switch nor the step at 13:47 from the newly visible satellite is seen in the position estimates. This is because the stochastic component of the measurement model applies an appropriately reduced weight for lower elevation satellites so that the baseline estimates are not negatively affected by poorer quality measurements. Once again, in the position error plots, similar trends to the ones already discussed are apparent; namely, the erratic behaviour of the float model at the beginning of the data set, the poor estimation of the fixed model at the end of the data set, and the compromise of the weighted model.

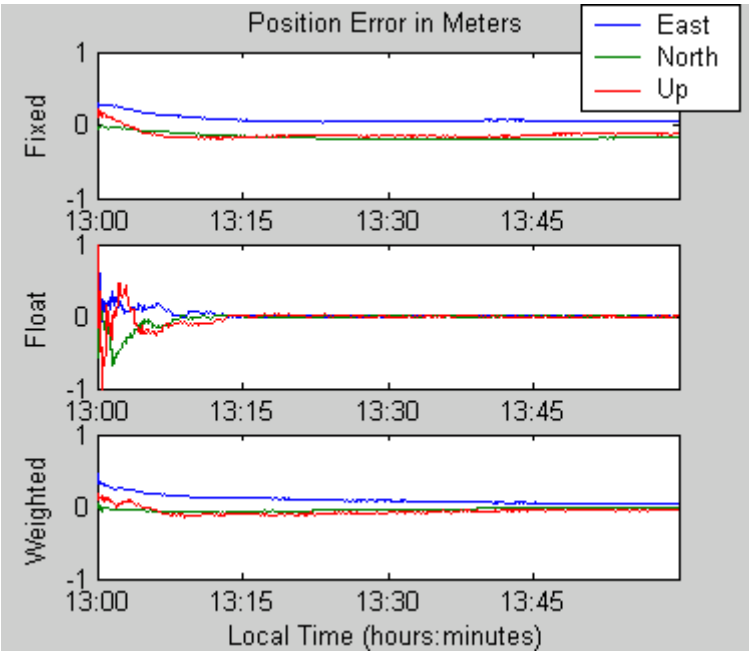

Figure 4.6: Baseline Error Using the Float (top), Fixed (middle), and Weighted (bottom) Ionosphere Models for a 30 km Baseline

The effect of using the fixed, float, and weighted ionospheric weighting schemes have been illustrated for a short and long baseline using simulated triple frequency GPS data. The next section will expand this analysis to investigate the impact that future GNSS measurements will have on the ability to estimate the ionosphere.

4.2 The Impact of Future GNSS Measurements on Ionosphere Estimation

Future GNSS signals will allow improved ionospheric estimation in three ways. First, there will be three frequencies transmitted from each satellite. This will cause the ionospheric delay to be more observable. Second, the future code measurements will be more precise and resilient to multipath errors than the current C/A code and the reconstructed P2 code. Third, when a combined GPS and Galileo system used, the number of satellites is increased which greatly improves the positioning geometry. These three factors enable faster convergence of the ionospheric states.

4.2.1 Ionosphere Estimation Results with Future GNSS Measurements

Figure 4.7, Figure 4.8, and Figure 4.9 show the root-mean-square error of ionospheric delay estimation for the various processing scenarios using the fixed, float, and weighted ionosphere models. For all the positioning scenarios, a simulated 30 kilometre baseline in Calgary was processed in kinematic mode with float ambiguities. The observational

time span was one hour and the data sampling rate was five seconds. For the weighted ionosphere model, a sampling of values for the ionospheric pseudo-observation standard deviation was used, but in all cases, the actual pseudo-observation was set to zero.

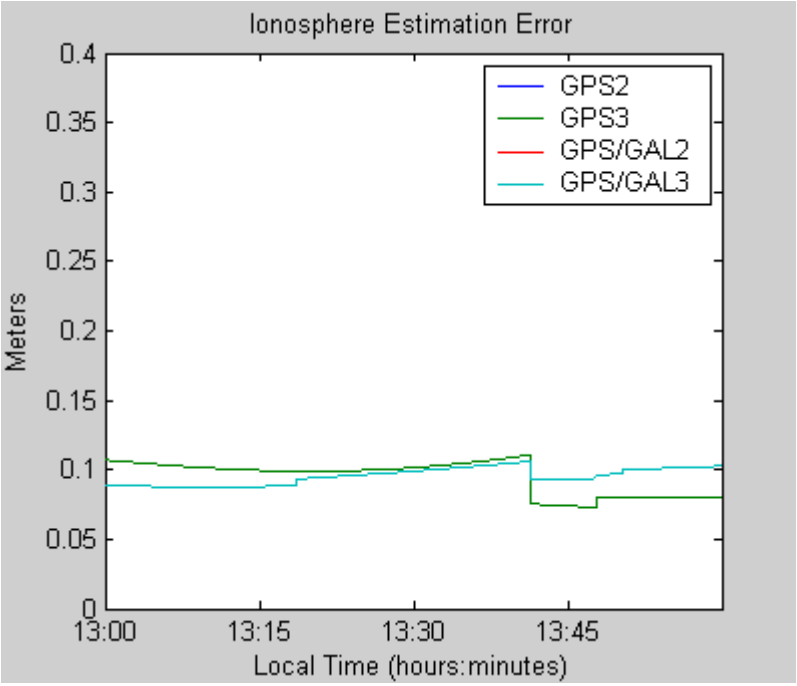

Figure 4.7: Ionospheric Delay Estimation Error with Various Processing Scenarios Using the Fixed Ionosphere Model

With the fixed ionosphere model, the error in ionospheric estimation is merely a function of the ionospheric error that has been applied to the simulated measurements. Thus, the error in ionospheric estimation depends only on the visible satellites. That is why the

GPS2 and GPS3 scenarios have exactly the same ionospheric estimation error and the GPS/GAL2 and GPS/GAL3 scenarios have exactly the same ionospheric estimation error. Therefore, Figure 4.7 does not convey anything about the ability of the future signals to estimate the ionospheric delay; it simply shows how the ionospheric delay deviates from zero.

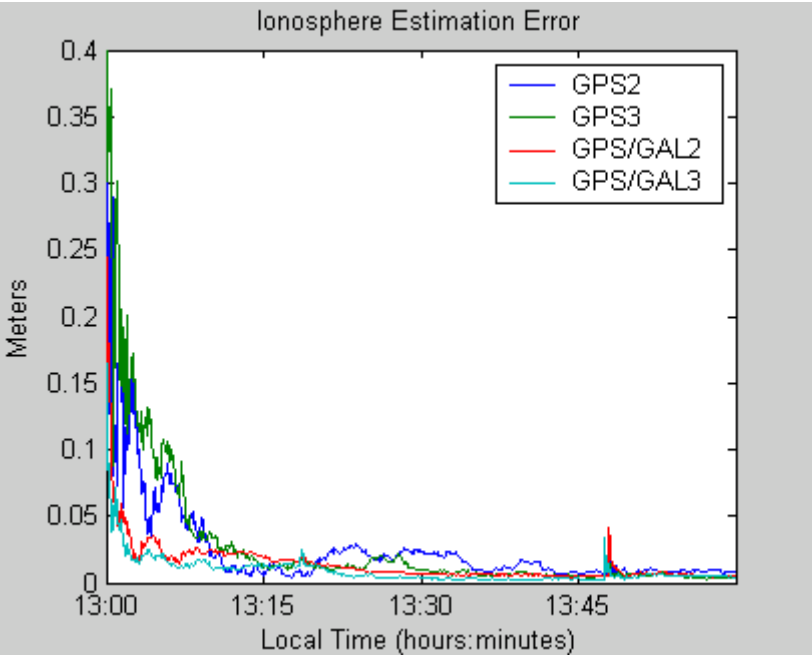

Figure 4.8: Ionospheric Delay Estimation Error with Various Processing Scenarios Using the Float Ionosphere Model

The float ionospheric estimation error shown in Figure 4.8 illustrates some important benefits of using future GNSS signals. It can be seen that the convergence of the dual and triple frequency GPS only scenarios (GPS2 and GPS3) is slower than that of the

combined GPS and Galileo scenarios. This is due to the improved geometry and the precise Galileo E5a code that is used in the GPS/GAL2 and GPS/GAL3 cases, but not in the GPS2 or GPS3 cases. This code is more precise than any of the GPS pseudorange codes and enables faster convergence of the ionospheric states. Another important observation from this plot is that after the 10 minute convergence period, the GPS2 scenario still has some significant variability in the ionospheric estimation error. The GPS2 scenario has the fewest carrier phase measurements and the least redundancy. This causes the ionospheric estimation to be less precise than in the other positioning scenarios. After complete convergence, all four of the scenarios appear to perform at the same level, indicating that the future signals will be of most benefit to those applications that demand fast convergence or fast ambiguity resolution.

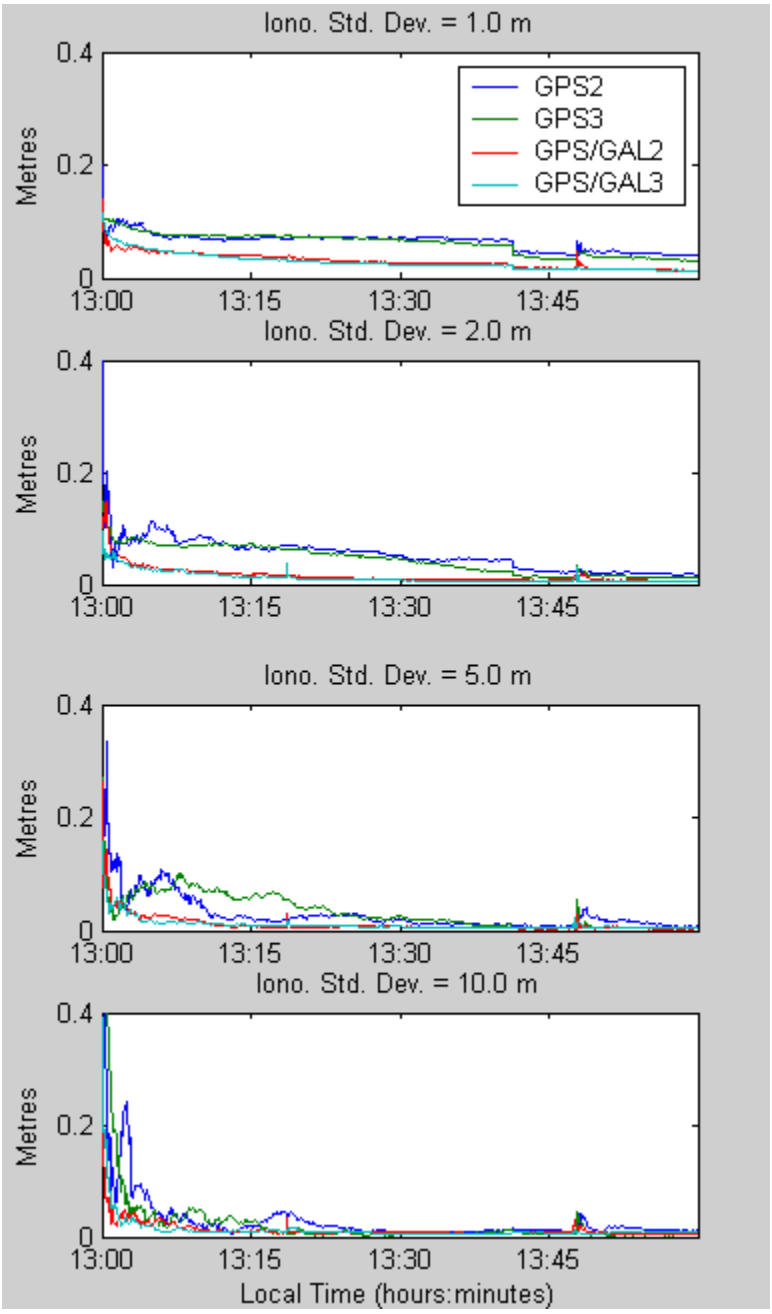

Figure 4.9: Ionospheric Delay Estimation Error with Various Processing Scenarios Using the Weighted Ionosphere Model

The weighted ionosphere model shows a marked difference in the positioning scenarios that do and the positioning scenarios that do not use Galileo measurements. This difference is most pronounced when the ionospheric pseudo-observation is more tightly constrained. Clearly, the increased number of satellites and the precise Galileo E5a code will have a significant impact in the ability to estimate the ionospheric delay quickly. As mentioned in the discussion in section 4.1.2, the steps at 13:41 are the result of a reference satellite switch and the small discontinuities seen at 13:47 are from an additional satellite becoming visible.

4.2.2 Ambiguity Estimation Results with Future GNSS Measurements

The primary reason for desiring precise estimates of the ionosphere is so that the float ambiguity values will also be precise. Intuitively, the more precise the float ambiguities are, the more reliable the integer ambiguity estimation will be. Reliable integer ambiguity estimation can provide precise estimates of the baseline components, which is ultimately the goal of any GNSS positioning application. Ionospheric estimation and ambiguity estimation are highly correlated, especially when short observation time spans are used. Figure 4.10, Figure 4.11, and Figure 4.12 show the root-mean-square error of the float ambiguity estimation for the same 30 km baseline as described above using the fixed, float and weighted ionosphere model.

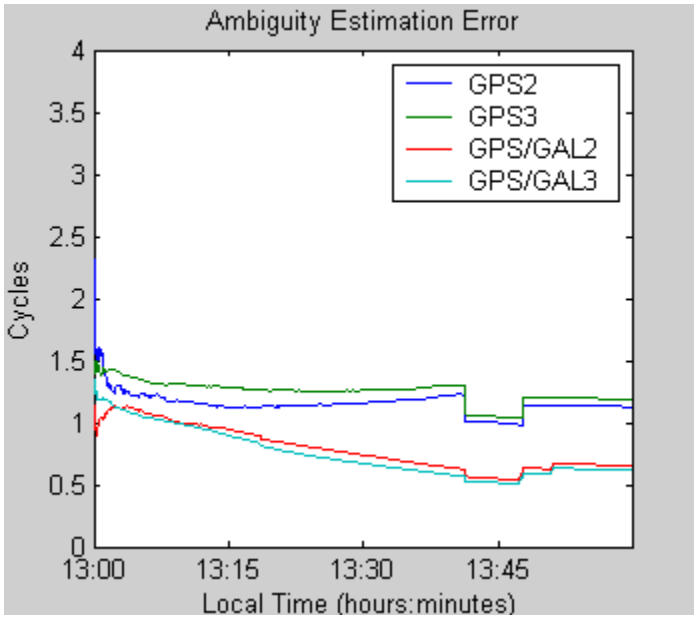

Figure 4.10: Ambiguity Estimation Error with Various Processing Scenarios Using the Fixed Ionosphere Model

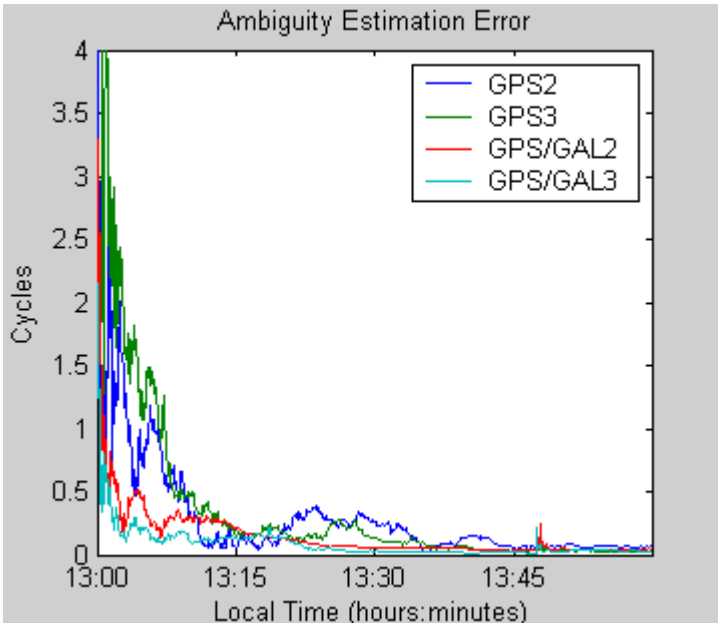

Figure 4.11: Ambiguity Estimation Error with Various Processing Scenarios Using the Float Ionosphere Model

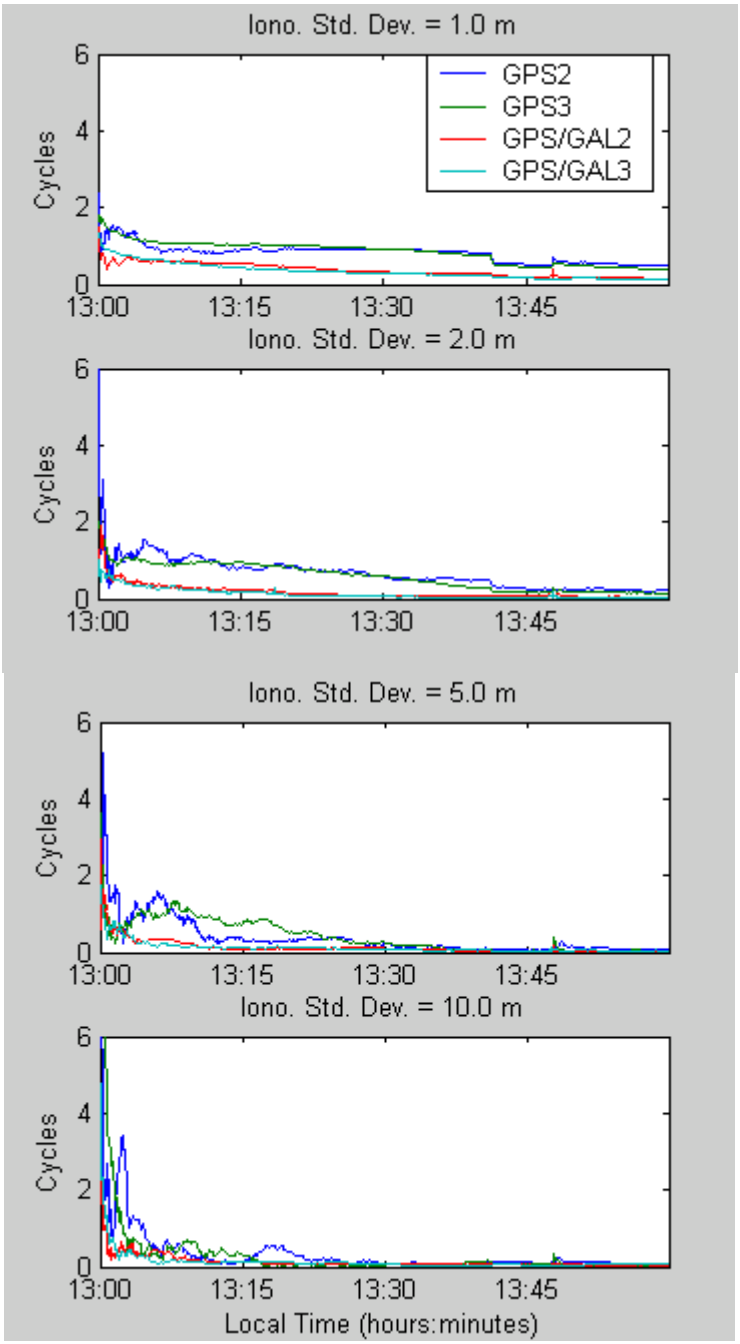

Figure 4.12: Ambiguity Estimation Error with Various Processing Scenarios Using the Weighted Ionosphere Model

The same trends that were seen in the plots of the ionospheric estimation error (Figure 4.7, Figure 4.8, and Figure 4.9) can also be seen in the preceding three plots of ambiguity estimation error. This is understandable because the ionosphere and ambiguity states are highly correlated. The more precisely the ionospheric delays can be estimated, the more precisely the ambiguities can be estimated. Once again, it is shown that the positioning scenarios that include Galileo satellites perform better than the scenarios using only GPS measurements.

4.2.3 Position Domain Results with Future GNSS Measurements

After showing how future GNSS measurements will affect the ionosphere and ambiguity state estimation, this section will illustrate how the future signals will impact the final baseline coordinate precision. Figure 4.13, Figure 4.14, and Figure 4.15 show the baseline coordinate errors for each positioning scenario using the fixed, float and weighted ionosphere model with a 30 kilometre baseline.

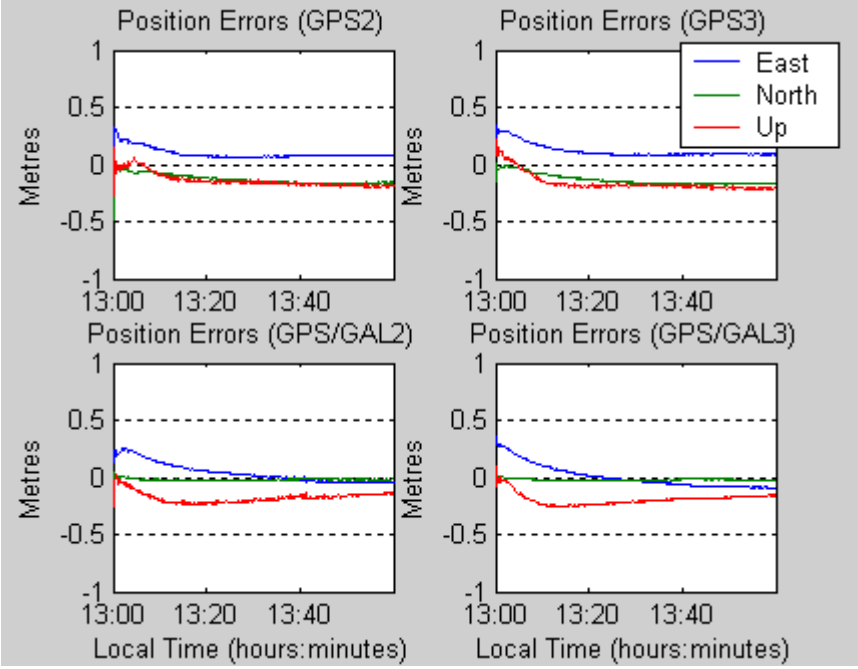

Figure 4.13: Position Errors with Various Processing Scenarios Using the Fixed Ionosphere Model

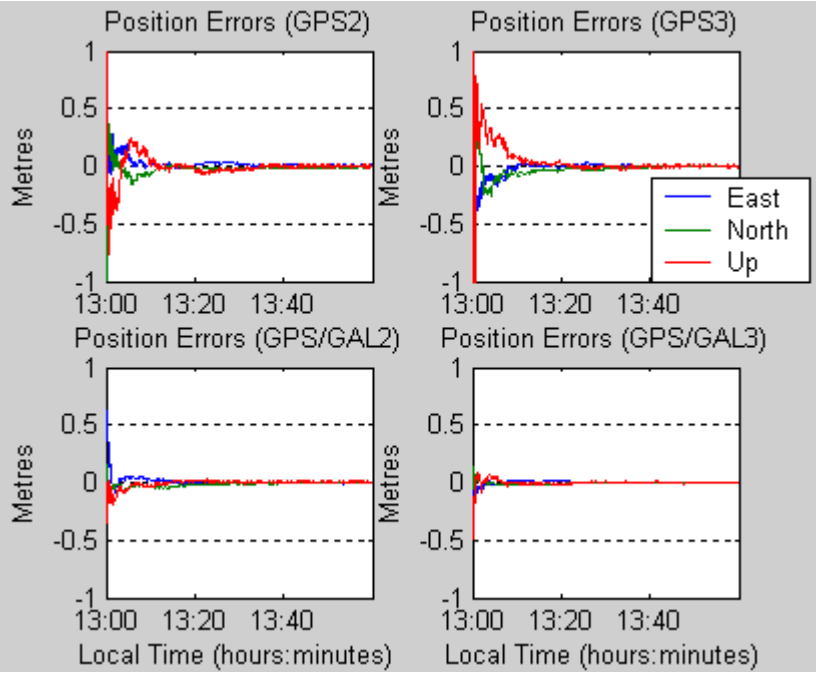

Figure 4.14: Position Errors with Various Processing Scenarios Using the Float Ionosphere Model

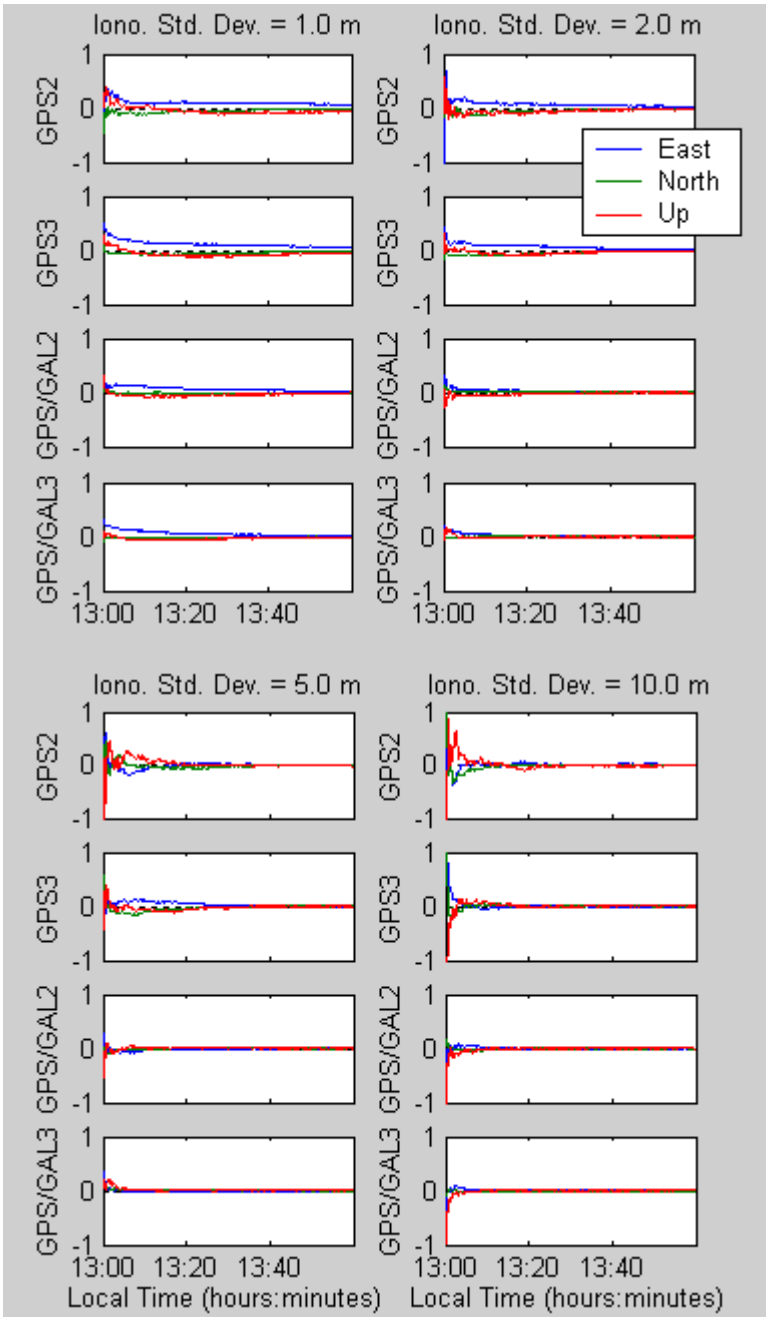

Figure 4.15: Position Errors with Various Processing Scenarios Using the Weighted Ionosphere Model

The preceding three plots again show similar trends that have been seen in the ionosphere and ambiguity states estimation error plots. For the fixed ionosphere model, all three positioning scenarios show significant biases resulting from the ionospheric errors. In all cases, the bias converges slightly at the beginning of the data set while the float ambiguities are converging, but the bias remains even after an hour of processing. The GPS/GAL2 and GPS/GAL3 scenarios perform marginally better than the GPS only scenarios because the ambiguity states are more precise as seen in Figure 4.10. Using the float ionosphere model, it can be seen that the scenarios using Galileo measurements converge much faster than the scenarios that do not employ the Galileo measurements. Again, this is due in large part to the more precise pseudorange code measurement and the increased number of visible satellites available when using Galileo satellites. The distinction between the GPS only scenarios and the combined GPS/Galileo scenarios is also seen in the plot of the position error using the weighted ionosphere model.

4.3 Summary

The underlying theory in estimating ionospheric delays as stochastic states has been introduced and the fixed, float, and weighted models for weighting the ionospheric delays have been described. Furthermore, tests were conducted to evaluate the impact of future signals on the ability to estimate ionospheric delays. It was found that the long-term accuracy (after convergence) of the baseline coordinates is improved only marginally

when using future GNSS signals. However, the speed with which this high accuracy can be achieved will be greatly improved. The most significant improvements in using future GNSS signals are the more precise pseudorange code measurements and the increased number of satellites when GPS and Galileo are used together. These improvements will enable faster ionospheric convergence when using the loosely weighted or float ionosphere models. This advantage allows the ambiguity states to converge faster and will greatly improve the ability to resolve integer ambiguities quickly over longer baselines.

It was also observed that there is very little difference between the GPS2 and GPS3 scenarios and between the GPS/GAL2 and GPS/GAL3 scenarios. This suggests that an additional third frequency will not greatly improve ionospheric estimation compared to dual-frequency systems when using the fixed, float or weighted ionosphere models. It will be seen in later chapters that the third frequency provides other benefits like improved ambiguity validation and additional choices for linear combinations of data.

This Chapter has scrutinized the impact of the future GNSS measurements on the ability to estimate ionospheric states. As a result, the second minor objective of the thesis has been accomplished. The ionospheric estimation techniques described in this chapter will be revisited again in the next chapter as it pertains to ambiguity resolution using future

GNSS signals. In Chapter Six, an alternative technique for dealing with ionospheric delays using linear combinations of data will be presented.

Chapter Five: The Effect of Future Signals on Ambiguity Resolution

In order to exploit the best accuracy possible from carrier phase measurements, the ambiguity parameters must be constrained to the correct integer value. This task has been widely discussed in the literature by numerous authors and has become standard practice in high-accuracy commercial GPS systems. There are two tasks involved in ambiguity resolution: integer searching, and ambiguity validation. Integer searching is the task of determining a set of integers that is most likely the correct one. Ambiguity validation is the procedure of determining whether or not the candidate set of integer values is actually the correct one. In principle, these two tasks are the same now as they will be when future GNSS signals become available. However, with future GNSS signals, the size of the ambiguity set will be increased and the quality of future pseudorange code measurements will be improved when compared to current GPS. These two factors will have an impact on the performance of ambiguity resolution and the techniques that will be employed for future GPS and Galileo systems.

While there is a common assumption that the future signals will improve the speed and reliability of ambiguity resolution, several researchers have noted that there are major difficulties when processing all three carrier phase measurements from both GPS and Galileo. Alves (2001) found that it was actually more difficult to correctly fix an ambiguity set with a triple-frequency combined GPS/Galileo system than with the GPS or

Galileo systems alone. This counterintuitive result is attributed to the large number of ambiguities to be estimated. A related problem was observed by Julien et al. (2004) who noted that the commonly used test for validating ambiguity sets is weakened as the number of ambiguities increases. In other words, it is more difficult to be sure about the correctness of a chosen ambiguity set when the dimension of the set increases. Using the mathematical concept of ambiguity success rate, Verhagen et al. (2003) shows that the probability of fixing all the ambiguities correctly decreases as the number of ambiguities to be fixed increases. This may or may not offset the improvement in ambiguity success rate that comes with the geometrical benefits of additional satellites.

This chapter will first give a review of some of the work that has already been done in the field of ambiguity resolution and then provide simulated test results using simulated future GNSS measurements.

5.1 Integer Ambiguity Search

Integer searching is the process of determining the best possible set of integer ambiguity values. The best set of ambiguities is generally defined as the set of integers that achieves the minimum sum of squared residuals. Numerous techniques have been developed for integer searching with currently available GPS data, and there have also been some developed for use with future GNSS data. The three most widespread

techniques for integer searching in the presence of future GNSS signals are the Cascade Integer Resolution (CIR) technique (Jung, 1999), the Triple Carrier Ambiguity Resolution (TCAR) technique (Vollath et al., 1998) and the Least-squares Ambiguity Decorrelation Adjustment (LAMBDA) technique (Teunissen, 1998).

Martin-Neira et al. (2003) and Teunissen et al. (2002) have published comparison studies that have evaluated the CIR, TCAR and LAMBDA methods for ambiguity resolution of future GNSS systems. These studies concluded that the LAMBDA method is superior to the other two and that in fact CIR and TCAR are special (usually suboptimal) cases of the more general LAMBDA technique. For this reason, the LAMBDA method has been chosen for implementation in this thesis. All three methods are discussed further in the next sections.

5.1.1 CIR and TCAR

CIR and TCAR are two techniques based on the same principles, but used for different systems; CIR was developed for triple frequency GPS ambiguity resolution and TCAR was developed for triple frequency Galileo ambiguity resolution. They both employ the concept of resolving ambiguities with successively smaller wavelengths until the ambiguity of the base frequency can be determined. First the *extra widelane* combination is solved using pseudorange data in a geometry-free model.

$$\hat{N}_{EWL} = \phi_{EWL} - \frac{P}{\lambda_{EWL}} \qquad (5.1)$$

where $\hat{N}_{EWL}$ is the estimated extra widelane ambiguity, ϕ_{EWL} is the extra widelane carrier phase measurement in cycles, P is a pseudorange measurement in metres, and λ_{EWL} is the wavelength of the extra widelane carrier signal. For GPS, the extra widelane combination is composed of the difference between the L2 and L5 carriers and has a wavelength of 5.86 metres; whereas, for Galileo, the extra widelane is composed of the difference between the E5a and E5b carriers and has a wavelength of 9.77 metres. There are different variations with regard to which pseudorange to use in Equation (5.1), but in general, the most precise pseudorange or blend of pseudoranges is chosen.

Presuming that the extra widelane ambiguity has been resolved with sufficient confidence, it is rounded to the nearest integer and used to resolve the next largest wavelength: the widelane (Jung, 1999).

$$\hat{N}_{WL} = \phi_{WL} - \frac{\lambda_{EWL}}{\lambda_{WL}}\left(\phi_{EWL} - \breve{N}_{EWL}\right) \qquad (5.2)$$

where *WL* stands for widelane and $\breve{N}_{EWL}$ is the resolved integer valued ambiguity for the extra widelane observable. For GPS, the widelane measurement is the difference of the L1 and L2 carrier phase measurements and has a wavelength of 0.86 metres; for Galileo, the widelane measurement is the difference between the E1 and E5b carrier phase measurements and has a wavelength of 0.81 metres. If the widelane ambiguity can be estimated with sufficient confidence, it can be rounded to the nearest integer and used to determine the next largest wavelength. This procedure is continued until the base frequency ambiguity is resolved. If one of the ambiguities cannot be resolved with sufficient confidence, more data is collected and averaged in order to improve the likelihood of finding the correct ambiguity. Table 5.1 summarizes the CIR and TCAR integer searching steps where the subscript, *ML*, stands for medium lane.

Table 5.1: CIR and TCAR Integer Searching Steps

	System	Carrier phase combination	Wavelength (metres)
$\hat{N}_{EWL} = \phi_{EWL} - \frac{P}{\lambda_{EWL}}$	GPS	$\phi_{EWL} = \phi_{L2} - \phi_{L5}$	$\lambda_{EWL} = 5.86$
	Galileo	$\phi_{EWL} = \phi_{E5b} - \phi_{E5a}$	$\lambda_{EWL} = 9.77$
$\hat{N}_{WL} = \phi_{WL} - \frac{\lambda_{EWL}}{\lambda_{WL}}\left(\phi_{EWL} - \breve{N}_{EWL}\right)$	GPS	$\phi_{WL} = \phi_{L1} - \phi_{L2}$	$\lambda_{WL} = 0.86$
	Galileo	$\phi_{WL} = \phi_{E1} - \phi_{E5b}$	$\lambda_{WL} = 0.81$
$\hat{N}_{ML} = \phi_{ML} - \frac{\lambda_{WL}}{\lambda_{ML}}\left(\phi_{WL} - \breve{N}_{WL}\right)$	GPS	$\phi_{ML} = \phi_{L1} - \phi_{L5}$	$\lambda_{ML} = 0.75$

	Galileo	$\phi_{ML} = \phi_{E1} - \phi_{E5a}$	$\lambda_{ML} = 0.75$
$\hat{N}_i = \phi_i - \frac{\lambda_{ML}}{\lambda_i}\left(\phi_{ML} - \breve{N}_{ML}\right)$	GPS	$\phi_i = \phi_{L1}$	$\lambda_i = 0.19$
	Galileo	$\phi_i = \phi_{E1}$	$\lambda_i = 0.19$

There can be many variations on this basic method with respect to which carrier phase measurements are used, what decision criterion is used before moving on to the next step and which type(s) of pseudoranges to use in the initial step. For more information on these methods, the reader is referred to Jung (1999), and Vollath et al. (1998) for original sources and to Jung et al. (2000), Liu et al. (2002), and Hatch et al. (2000) for variations and test results.

5.1.2 LAMBDA

The **L**east Squares **AMB**iguity **D**ecorrelation **A**djustment technique was originally developed by P. J. G. Teunissen (Delft University of Technology) for currently available single or dual-frequency GPS ambiguity resolution, but it has a flexible design that allows it to be used with future GNSS signals on numerous frequencies (Teunissen, 1998). This section will give a brief outline of the LAMBDA technique.

The basic premise of the LAMBDA technique is that the original set of ambiguities is transformed into a different set of ambiguities that are less correlated and more precise

than the original ambiguities. These transformed ambiguities are then fixed to integer values and the constraint is used to improve the precision of the other unknown parameters like the baseline components and ionospheric delay parameters.

The ambiguity vector and its associated covariance matrix are transformed with the decorrelating Z matrix through the following equations.

$$\hat{z} = Z\hat{a} \qquad \hat{z}, \hat{a} \in R \qquad (5.3)$$

and

$$Q_{\hat{z}} = Z^T Q_{\hat{a}} Z \qquad (5.4)$$

where $\hat{z}$ is the vector of transformed ambiguities, $\hat{a}$ is the vector of original ambiguities and Q_* are the associated variance covariance matrices.

The integer constraint is then applied through the following constraint equations:

$$\breve{x} = \hat{x} - Q_{\hat{x}\hat{z}} Q_{\hat{z}} \left(\hat{z} - \breve{z}\right) \qquad (5.5)$$

and

$$Q_{\breve{x}} = Q_{\hat{x}} - Q_{\hat{x}\hat{z}} Q_{\hat{z}}^{-1} Q_{\hat{z}\hat{x}} \qquad (5.6)$$

where $\breve{z}$ is the vector of transformed integer constrained ambiguities and $\breve{x}$ is the state vector conditioned on integer constrained ambiguities.

The transformation matrix, Z, is chosen as a matrix that will decorrelate the ambiguities. Ideally, one would like the ambiguities to be completely decorrelated, resulting in a diagonal covariance matrix. In this case, the real-valued ambiguities could simply be rounded to the nearest integer to obtain the most likely set of integer ambiguities. A perfect decorrelation transformation would be straightforward using well established eigen-value (or similar) decomposition techniques. However, when dealing with integer ambiguity estimation, there are restrictions on the set of possible decorrelating transformation matrices. The elements of the transformation matrix must be integer valued in order to retain the integer nature of the ambiguity states. In addition, the inverse of the matrix must also be composed of integer values to ensure that the constraint in the transformed domain corresponds to an integer constraint in the untransformed domain. In general, a perfect transformation matrix will contain non-integer values; consequently, a full decorrelation of the ambiguities is not possible. Even so, a partial decorrelation is still possible which drastically reduces the integer search space.

After decorrelating the ambiguities, the most likely set of integer values are obtained through an integer bootstrapping procedure. Integer bootstrapping is a sequential search technique that minimizes the number of potential integer ambiguity sets using the covariance information of the ambiguities. In the integer bootstrapping algorithm, each

ambiguity is given a search width based on its predicted variance. The first ambiguity in the vector of ambiguities is fixed to an integer value that is within the search width for that ambiguity. The fixing of this first ambiguity affects the float estimates and covariance information of all the remaining ambiguities. Consequently, the new covariance information can be computed assuming that the first ambiguity was fixed to the correct value. All the remaining ambiguities will have a slightly smaller search width on account of the first fixed ambiguity. Next, the second ambiguity is fixed to an integer value within its search width and the float estimates and covariance information of the remaining ambiguities are again recomputed. This procedure continues until one of two outcomes is reached:

1. There are no integers within the search width for the next ambiguity. In this case, an ambiguity must have been fixed to an incorrect integer in a prior step so the search will start over again or more data will have to be collected.
2. One or more complete set of integers is found.

More information on integer bootstrapping can be obtained in Teunissen (2001).

Upon completion of the integer bootstrapping procedure, there will be several potential integer ambiguity sets that will be subjected to a variety of validation tests before being chosen as the correct one. There is no specific validation procedure associated with the

LAMBDA technique, but various discrimination tests will be discussed in Section 5.2. For further details about LAMBDA including implementation issues, the reader is referred to Teunissen (1998), De Jonge et al. (1998), Teunissen et al. (1997), and Joosten et al. (2000).

5.2 Ambiguity Validation

The second task in integer ambiguity resolution is validation. Once a potential ambiguity set has been selected, this ambiguity set must be either accepted as the correct one, or rejected. In order to accept an ambiguity set with a reasonable degree of confidence, two criteria must be satisfied. First of all, a potential ambiguity set must fit the model and observations; and secondly, it must be shown that the best ambiguity set is significantly better than all other potential ambiguity sets. These two tasks are accomplished through an acceptance test and a discrimination test respectively.

5.2.1 Acceptance Test

To ensure that the best ambiguity set fits the model and observations with a sufficient degree of significance, a statistical acceptance test is performed. The hypothesis to be tested is

$$H_0 : E(\hat{a}) = K_i \text{ and } H_1 : E(\hat{a}) \neq K_i \qquad (5.7)$$

where $E(\cdot)$ is the mathematical expectation operator, $\hat{a}$ is the vector of estimated real-valued ambiguities and K_i is the i^{th} potential set of integer ambiguities.

Assuming that the real valued ambiguities have a Gaussian distribution, the following test statistic can be used.

$$T_i = \frac{n-m-t}{m} \cdot \frac{R_i}{\Omega_0} \qquad (5.8)$$

where

n is the number of observations;

m is the number of ambiguities;

t is the number of other parameters (position states, ionosphere states,

etc.);

Ω_0 is the weighted sum of squared residuals from the float ambiguities;

and R_i is given by,

$$R_i = (\hat{a} - K_i)^T Q_{\hat{a}}^{-1} (\hat{a} - K_i) \qquad (5.9)$$

where $Q_{\hat{a}}$ is the cofactor matrix of the float ambiguities.

The test statistic given by Equation (5.8) is compared to the Fisher distribution with the following inequality:

$$T > F_{\alpha}(m, n - m - t) \qquad (5.10)$$

Therefore, if the ambiguity set, *i*, satisfies the above inequality, that set of integer ambiguity values (K_i) should be rejected because it does not fit the model or the observations with the significance level, α. This test is described in more detail in most statistics text books (e.g. Walpole et al., 1998) and is applied to the GPS ambiguity resolution application in Wang et al. (1998).

5.2.2 Discrimination Test

After determining that the best potential ambiguity set fits the observations, it must be compared to the other potential ambiguity sets. A comparison is necessary because it is likely and even probable that two (or more) distinct ambiguity sets may fit the model and the observations with a high degree of confidence.

The standard practice is to compare the best ambiguity set to the second best ambiguity set. If the best ambiguity set is significantly "better" than the second best ambiguity set, it follows that the best set is significantly "better" than *all* other potential ambiguity sets and the best set can be accepted as the correct one. There are many different definitions and techniques for discriminating between correct and incorrect ambiguity sets. Verhagen (2004) gives a summary of many of the available ambiguity validation techniques and concludes that none of the proposed methods can be singled out as significantly better than the others. The reason is that none of the ambiguity validation procedures are based on correct statistical theory and different techniques are better suited to different applications.

The most common procedure for making a comparison between the two ambiguity sets is by considering a ratio test. Landau et al. (1992) proposed to compare the ratio of the weighted sum of squared residuals of the best ambiguity set to the weighted sum of squared residuals of the second best ambiguity set. If the ratio is above a certain

threshold, the best ambiguity set is accepted as the correct one. While there is no statistically quantifiable confidence associated with this test, it has been shown to perform well (Landau et al. 1992, Richert et al. 2004) and has gathered much widespread use in both commercial and academic applications. Symbolically, the ratio test is described by

$$\frac{\Omega_2}{\Omega_1} > k \qquad (5.11)$$

where k is an empirically chosen constant, and Ω_i are the weighted sum of squared residual values of the best ($i = 1$) and second best ($i = 2$) ambiguity sets.

Equation (5.11) has often been mistaken to follow a Fisher distribution, which is commonly used to test between the variances of two independent random variables. In the case of this application, the Fisher distribution cannot be used because the best and second best solutions are not independent. The choice of an optimal value for the threshold, k, depends on the degrees of freedom of the problem and the confidence level desired. A value of 2.0 has been suggested by Landau et al. and has been shown to work well in a variety of applications.

The test described by Equation (5.11) compares the two fixed solutions with one another. There is a more powerful test that can be used if there is already sufficient confidence in the float solution. This test is another ratio test but it is described as:

$$\frac{R_2}{R_1} = \frac{(\hat{a} - K_2)^T Q_{\hat{a}}^{-1} (\hat{a} - K_2)}{(\hat{a} - K_1)^T Q_{\hat{a}}^{-1} (\hat{a} - K_1)} = \frac{\Omega_2 - \Omega_\circ}{\Omega_1 - \Omega_\circ} > k \qquad (5.12)$$

Once again, there is a problem in choosing an appropriate value for the constant, *k*, because, like the aforementioned ratio test, this test is not based on sound statistical theories. The advantage of using the test described by Equation (5.12) over the test described by Equation (5.11) is that the variance in the float solution is removed so that the comparison is based on the distance between the float and the fixed solutions. This test has been found to perform better when estimating the ionospheric delays as states because the impact of the ionospheric states is removed, which causes the differences in the ambiguity sets to be emphasized. In other words, with Equation (5.12), it is assumed that the float ionosphere estimates are acceptable and the test focuses only on the ambiguity states; whereas, with Equation (5.11), the test attempts to test the ambiguities and the ionosphere states together, which often prevents the ratio from deviating sufficiently from 1.0. Therefore, Equation (5.12) has been chosen for implementation in this thesis.

5.3 Test Results Using Future GNSS Measurements

The following section provides some experimental ambiguity resolution test results using simulated future GNSS measurements. First, the ability to find the correct ambiguity set will be demonstrated. Clearly, the ability to find the correct ambiguity set will depend on numerous factors including the length of the baseline, the time of day, the positioning scenario used (i.e. GPS2, GPS3, GPS/GAL2, or GPS/GAL3), and the choice of ionospheric model. These factors will be discussed and tested in Section 5.3.1.

After quantifying the ability to find the correct ambiguity set, Section 5.3.2 will examine the degree to which the correct ambiguity set can be validated. The ratio values resulting from instantaneous ambiguity resolution tests will be shown for both short and long baselines using fixed and weighted ionosphere models for the four positioning scenarios. In addition, the impact of baseline length on ambiguity validation will be illustrated for each of the four positioning scenarios.

Finally, since the speed with which integer ambiguities can be resolved is of utmost importance in many precise kinematic applications, this performance measure will be compared for the four positioning scenarios. Results that describe the improvement in the time to fix ambiguities are shown in Section 5.3.3.

5.3.1 Integer Ambiguity Search Results with Future GNSS Signals

In order to evaluate the ability of each positioning scenario to find the correct set of integer ambiguities, instantaneous ambiguity resolution was attempted every 200 seconds between 7:00 and 22:00 local time in Calgary, Canada. In the context of this study, instantaneous ambiguity resolution is defined as ambiguity resolution after only two epochs of 1 Hertz data. Before each attempt at ambiguity resolution, the filter was completely reset so that no *a priori* information was used. Referring back to Figure 3.3 it can be seen that the time period for which this test was conducted is during the peak of the diurnal ionosphere cycle. Further discussion on the effect of the diurnal cycle of the ionosphere will be presented in Section 5.3.2. The baseline length was varied from 10 to 80 kilometres and was processed using all four of the positioning scenarios described in Table 1.1. The weighted ionosphere model was used to estimate the ionospheric delay states and the standard deviation of the ionospheric pseudo-observation was varied from 0.3 to 2.5 metres. As in all the tests in this thesis, the roving receiver was assumed kinematic and a medium level of ionospheric activity was applied to the simulated observations. Since simulated data was used, the correct integer values of the ambiguities are known and the percentage of trials that found this correct ambiguity set are plotted below in Figure 5.1.

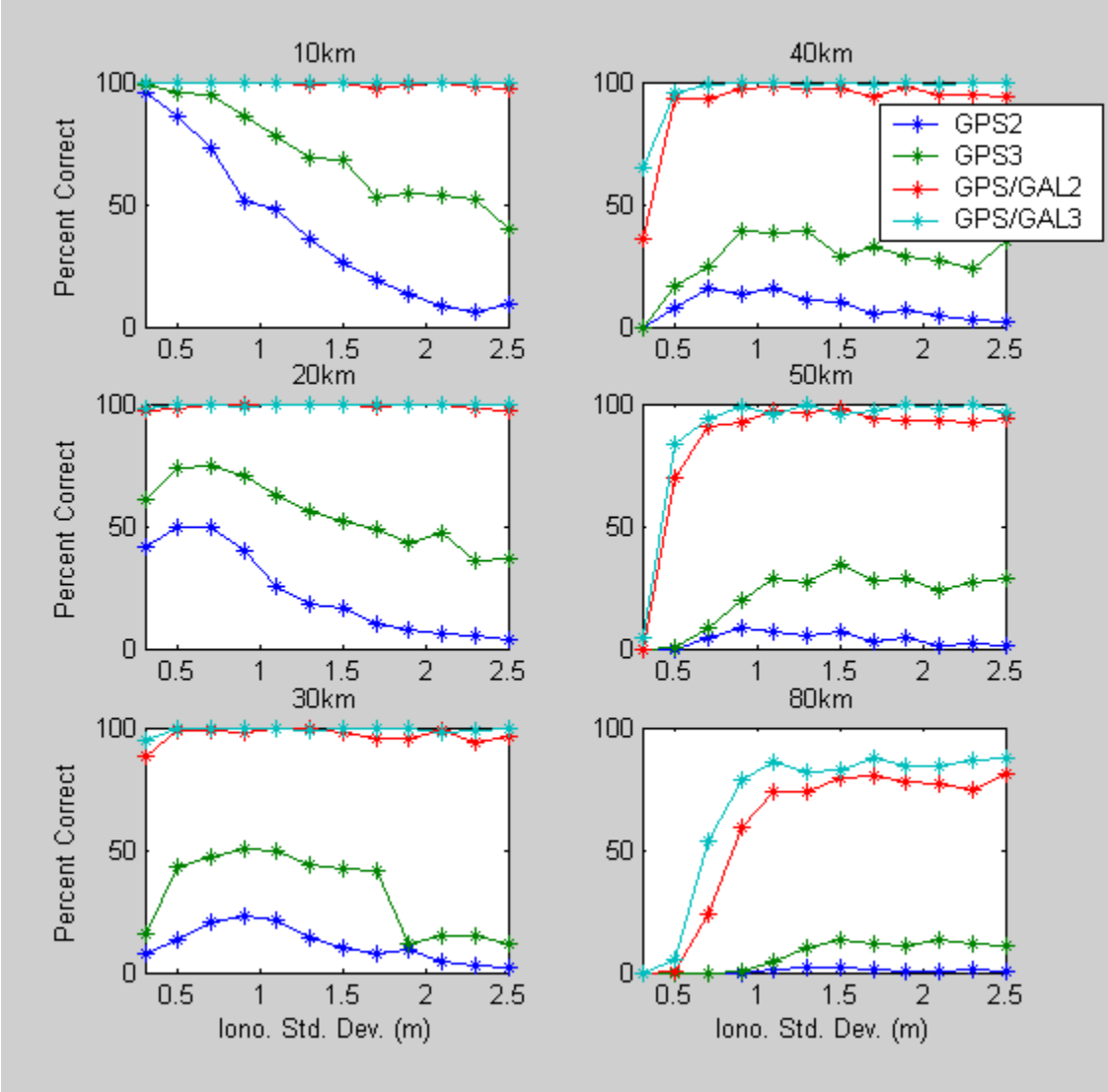

Figure 5.1: Percentage of Correct Ambiguity Sets Versus Ionospheric Pseudo-Observation Standard Deviation

The first deduction from Figure 5.1 is that the scenarios that include Galileo measurements find the correct ambiguity set more often than the GPS only scenarios

regardless of the value of the ionospheric pseudo-observation or the baseline length. This result corresponds to the findings of Chapter Four where it was found that the scenarios using combined GPS and Galileo signals provided more precise estimates of the ionospheric delays due to the higher precision of the Galileo E5a code measurement and the improved satellite geometry.

A second observation from Figure 5.1 is that the GPS2 and GPS3 scenarios appear to exhibit a distinct maximum in percent of correct ambiguity sets. The maximum is most pronounced for baseline lengths of 10, 20, and 30 kilometres where the maximum values occur at ionospheric pseudo-observation standard deviations of 0, 0.5, and 0.9 for GPS2 and 0, 0.7, and 0.9 for GPS3. A similar phenomenon was found using real dual-frequency GPS data in a study done by Alves et al. (2002). Interestingly, a distinct maximum value is not seen in the cases of GPS/GAL2 or GPS/GAL3. In these positioning scenarios, the percentage of correct ambiguity sets remains fairly constant for a wide range of ionospheric constraint standard deviations. This can be explained by discussing three categories of baseline lengths: short, long, and medium.

For short baselines (10 kilometres or less), the fixed ionosphere model performs best for all four positioning scenarios. This is expected because the ionospheric delays are tightly constrained to zero, which is very close to the true value. For long baselines (80 kilometres or more), the float ionosphere model performs best for all four positioning

scenarios. This is also expected because the true ionospheric values deviate from zero so much that the code measurements are able to provide a better estimate of the ionospheric delays than the zero value constraint. However, for the medium baselines (20 to 50 kilometres), the positioning scenarios that use Galileo measurements behave differently from the positioning scenarios that use only GPS measurements. The maximum in the plots for the GPS2 and GPS3 scenarios demonstrate the advantage of using the weighted model. Using an appropriately weighted ionospheric constraint gives a higher percentage of correct ambiguity sets than either the fixed or float models. This has been documented in previous studies on the benefits of using the ionosphere weighted model (Julien et. al., 2004; Odijk 2001). However, for the GPS/GAL2 and GPS/GAL3 scenarios with medium baselines, a clearly defined optimal standard deviation does not exist.

The reason for this is that in the GPS/GAL2 and GPS/GAL3 scenarios, the ionospheric delay states are estimated very well by the code observations. In fact, the ionospheric delay states are estimated so well, that the error in the ionospheric estimation is no longer the factor that limits the ability to find the correct ambiguity set. Consequently, any improvement in the ability to find the correct ambiguity set resulting from the ionospheric constraint is almost imperceptible. For the 80 kilometre baseline, when the percentage of correct ambiguity sets decreases, the cause is not the error in estimating the ionosphere, but rather, the other unmodeled error sources (i.e. residual tropospheric

effects). Therefore, the choice of ionospheric pseudo-observation standard deviation is inconsequential as long it does not constrain the ionospheric delays to an incorrect value too tightly.

With the GPS2 and GPS3 scenarios, the ionospheric delay states are not estimated as well by the code observations so the impact of the ionosphere constraints is far more noticeable and the choice of standard deviation for the constraint is more crucial for successful integer ambiguity searching.

The preceding test examined the ability to find the correct integer ambiguity set. However, the major issue in real GNSS positioning systems is not only whether or not the correct ambiguity set can be found, but also, whether or not a potential ambiguity set can be successfully validated as correct or incorrect. The next section examines ambiguity validation using future GNSS signals.

5.3.2 Ambiguity Validation Results Using Future GNSS Signals

Two of the most dominant factors affecting the ability to successfully validate integer ambiguity sets are the time of day, which is related to the level of ionospheric activity, and the baseline length, which is related to the decorrelation of spatially correlated error

sources. The impact of these two factors on instantaneous ambiguity validation using future GNSS signals is investigated in the following two sections.

5.3.2.1 Test Results for Varying Times of Day

In order to portray the impact that future GNSS signals will have on the ability to successfully validate integer ambiguity sets, instantaneous ambiguity resolution was performed every 10 minutes on a 5 kilometre baseline in Calgary, Canada using the four processing scenarios outlined in Table 1.1. The ionosphere fixed model was used because it has already been established that this is the optimal ionospheric model for short baselines. This test was used to demonstrate instantaneous ambiguity validation over the course of an entire day.

In Figure 5.2, the ratio test value is plotted - that is, the ratio of the distance between the float and the second best set of fixed ambiguities to the distance between the float and the best set of fixed ambiguities (Equation (5.12)). Since a discrimination threshold of 2.0 is typically chosen, any data points below 2.0 (shown in blue) would be rejected.

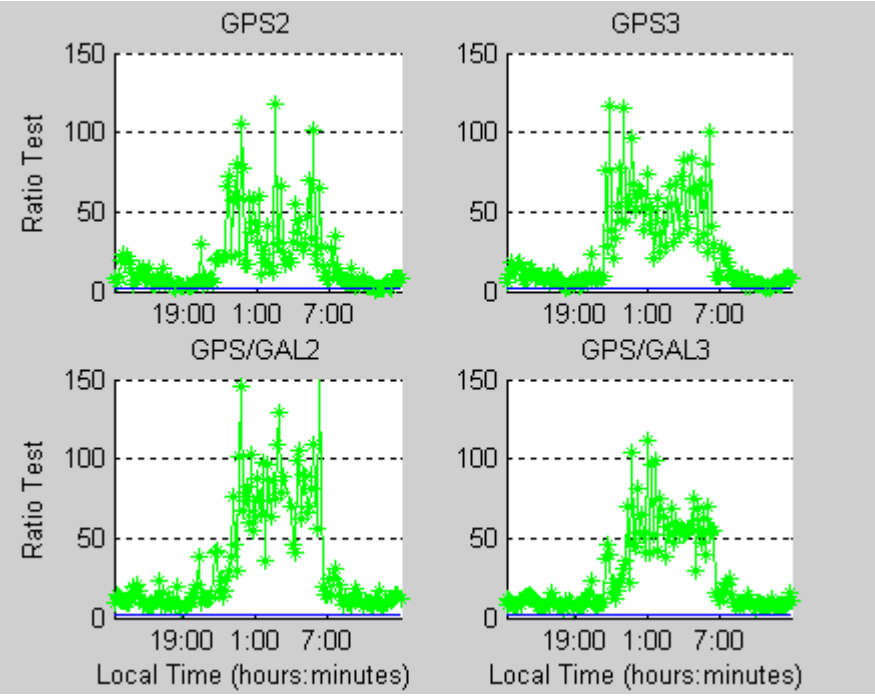

Figure 5.2: Ratio Test Values for a Five km Baseline

There is very little difference between the four scenarios for a short baseline. For all four scenarios, ambiguity resolution was successful at every epoch. Consequently, there are no cases where an incorrect solution was accepted. However, there were two cases in the GPS2 and GPS3 scenarios where a correct solution would have been rejected due to a ratio test value below the threshold of 2.0. In the GPS/GAL2 and GPS/GAL3 scenarios, none of the correct ambiguity sets were rejected, resulting in 100% successful ambiguity validation. The effect of the varying ionospheric delay over the course of the day can be clearly seen. Those time periods with low ionospheric activity (22:00 until 7:00 local time) have a higher ratio value, which indicates more confidence in the fixed ambiguity

solution. Since ambiguity resolution is already quite reliable for short baselines with the currently available GPS signals, the inclusion of future measurements does not significantly improve the situation.

The same instantaneous ambiguity resolution test was conducted again, but this time, the baseline length was 30 kilometres. Figure 5.3 shows the ratio test results for the four positioning scenarios when using the ionosphere fixed model. In the following plots, the red points indicate epochs where the best ambiguity set was incorrect and the green points represent those cases where the best ambiguity set was indeed the correct one.

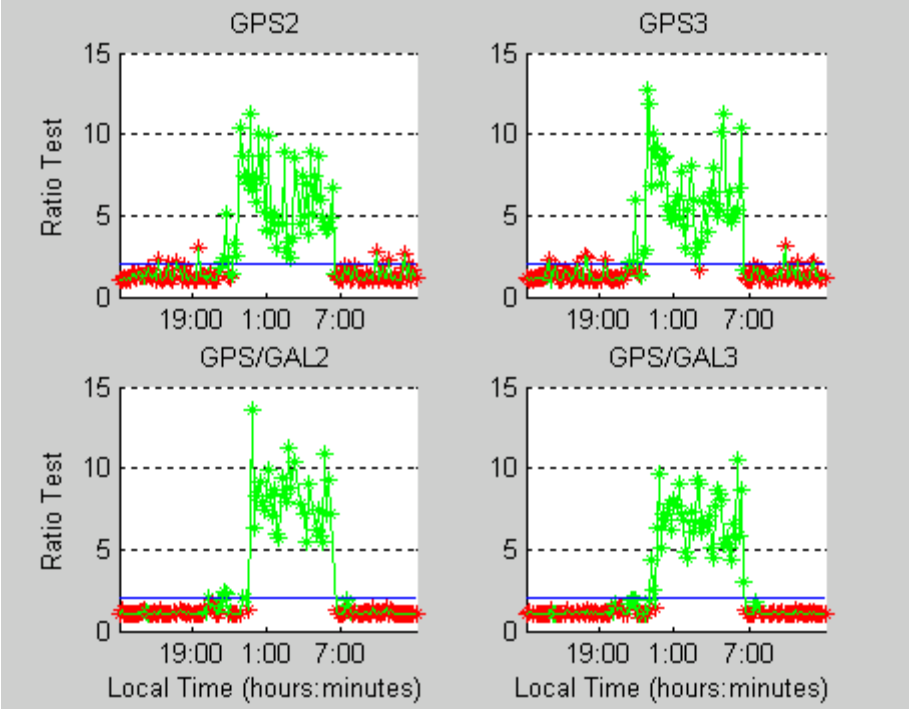

Figure 5.3: Ratio Test Values for a 30 km Baseline Using the Ionosphere Fixed Model

When using the ionosphere fixed model, the ionospheric interference clearly affects all four scenarios. For each positioning scenario, instantaneous ambiguity resolution was impossible between 7:00 and 22:00 local time, which is when the ionosphere was most active. The correct ambiguity sets occurring during periods of low ionospheric activity have a higher ratio value for the scenarios using Galileo measurements, which means that the confidence in the correct solution is higher. In addition, there are fewer incorrect ambiguity sets that have ratio values above the 2.0 threshold. This implies that

instantaneous ambiguity resolution with the fixed ionosphere model using combined GPS and Galileo measurements will be more reliable than using either dual or triple frequency GPS measurements alone. With reference back to Chapter Four, the reasons for this improvement are the improved geometry and the higher precision E5a pseudorange measurements that allow more precise initial estimation of the ionosphere and ambiguity states.

The same 30 kilometre baseline was again processed, but using the ionosphere weighted model instead of the ionosphere fixed model. For the standard deviations of the ionospheric pseudo-observation in the ionosphere weighted model, the optimal values according to Figure 5.1 were used. It should be noted, that the optimal values from Figure 5.1 were derived using only data from 7:00 till 22:00 local time. This is the period of peak ionospheric activity in the day and the optimal values of the ionospheric constraints can only be assumed relevant for the same time period.

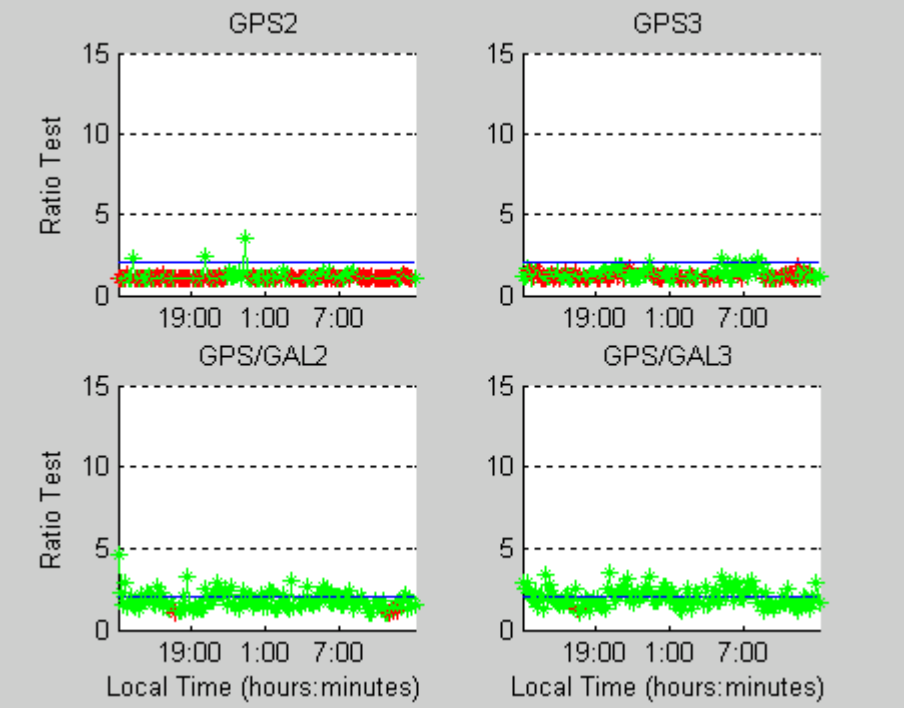

Figure 5.4: Ratio Test Values for a 30 km Baseline Using the Ionosphere Weighted Model

When using the ionosphere weighted model with ionospheric pseudo-observation standard deviations that are optimized for peak ionosphere times, the ambiguity resolution performance in times of peak ionospheric activity (7:00 till 22:00 local time) is greatly improved when compared to the ionosphere fixed model. The numerical ambiguity validation results for periods of peak ionospheric activity are shown in Table 5.2. In the table, the percentage of ambiguity resolution attempts from 7:00 till 22:00 that produced the desired result and the undesired result are shown. The desired result is a correct ambiguity set with a ratio value above 2.0; the undesired result is an incorrect

ambiguity set with a ratio value above 2.0. The improvement in using the weighted ionosphere model is most pronounced in the GPS/GAL2 and GPS/GAL3 scenarios where the number of correct ambiguity sets that would be accepted is greatly increased, while the number of incorrect ambiguity sets that would be accepted remains zero.

Table 5.2: Ambiguity Validation Results during Periods of Peak Ionospheric Activity

	% of Correct Ambiguity Sets Accepted		% of Incorrect Ambiguity Sets Accepted	
	Fixed Ionosphere	Weighted Ionosphere	Fixed Ionosphere	Weighted Ionosphere
GPS2	3	2	9	0
GPS3	3	1	10	0
GPS/GAL2	2	24	0	0
GPS/GAL3	0	39	0	0

Unfortunately, since the standard deviations of the ionosphere constraints are optimized for the peak ionosphere times, the ambiguity validation performance deteriorates for periods of low ionospheric activity when using the ionosphere weighted model with the same weights on the constraints. Table 5.3 shows the numerical ambiguity validation results for periods of low ionospheric activity.

Table 5.3: Ambiguity Validation Results during Periods of Low Ionospheric Activity

	% of Correct Ambiguity Sets Accepted		% of Incorrect Ambiguity Sets Accepted	
	Fixed Ionosphere	Weighted Ionosphere	Fixed Ionosphere	Weighted Ionosphere
GPS2	88	2	0	0
GPS3	87	6	0	0
GPS/GAL2	78	35	0	0
GPS/GAL3	81	52	0	0

The important conclusion from the above analysis is that when using the fixed ionosphere model, all the positioning scenarios perform similarly with the GPS/GAL2 and GPS/GAL3 scenarios giving marginally better ambiguity validation results. However, with the ionosphere weighted model, the scenarios with Galileo measurements perform notably better. Once again, this is due in large part to the more precise Galileo E5a code measurements and the improved geometry with the combined GPS and Galileo constellation. These advantages provide more accurate estimates of the ionospheric states almost instantaneously which enable more reliable ambiguity resolution. Only in the weighted (or float) ionosphere model are these precise ionosphere estimates fully exploited.

5.3.2.2 Test Results for Varying Baseline Length

In the previous section it was established that the time of day (or the level of ionospheric activity) drastically affects the ability to successfully validate ambiguity sets for all four positioning scenarios. The preceding analysis examined a 5 kilometre and a 30 kilometre baseline. This section examines the performance of ambiguity validation for the four different positioning scenarios as the baseline length is varied from short (5 km) to long (80 km) baselines.

A test was conducted in which instantaneous ambiguity resolution was performed every 200 seconds during the periods of the day that experienced peak ionospheric activity (7:00 till 22:00). For this test, the ionosphere weighted model was used to estimate the ionospheric states and the optimal ionospheric pseudo-observation standard deviations from Figure 5.1 were used. Figure 5.5 shows the percentage of trials that found the correct ambiguity set (dark blue bars), the percentage of trials that found the correct ambiguity set *and* generated a ratio value above the threshold of 2.0 (light green bars), and the percentage of trials that did not find the correct ambiguity set, but still had a ratio value above the threshold of 2.0 (burgundy bars).

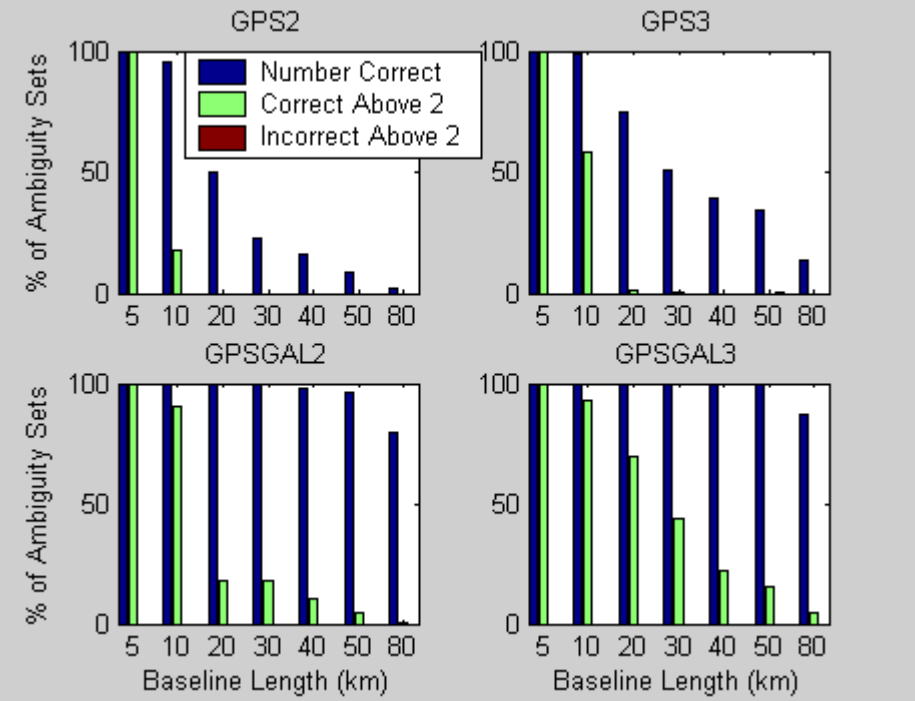

Figure 5.5: Instantaneous Ambiguity Validation as a Function of Baseline Length

The preceding figure shows an important feature of using triple frequency data versus dual frequency data. When looking at 10 kilometre baseline in the GPS2 and GPS3 scenarios, it can be seen that the percentage of correct ambiguity sets that were found is slightly more for the triple frequency case than for the dual frequency case. For the GPS3 scenario, 100% of the ambiguity sets were correct; whereas, for the GPS2 scenario, 95% of the ambiguity sets were correct. However, the percentage of correct ambiguity sets that were successfully validated in the triple frequency case is substantially more than in the dual frequency case. Only 17% of the correct ambiguity sets in the GPS2 scenario were successfully validated; whereas, 58% of the correct ambiguity sets in the

GPS3 scenario were successfully validated. The same phenomenon is witnessed when looking at the GPS/GAL2 and GPS/GAL3 scenarios. The triple frequency case provides more successful ambiguity validation despite having similar integer ambiguity search performance. The reason for this improvement in ambiguity validation is because the triple frequency scenarios have a higher redundancy than the dual-frequency cases. As a result, the correct ambiguity set stands out more clearly as the vector with the smallest distance between the float and fixed ambiguities.

5.3.3 The Impact of Future GNSS Measurements on the Speed of Ambiguity Resolution

In many applications, particularly real-time kinematic applications, the speed with which the integer ambiguity vector can be resolved is of utmost importance. A common performance measure for the speed of fixing ambiguities is the **m**ean **t**ime **t**o first **f**ix or MTTF, which is the amount of time required before the correct ambiguity set is found and validated. In this section, the mean time to first fix will be tested for the four positioning scenarios.

When investigating the mean time to first fix performance, the treatment of the ionospheric delays cannot be ignored because it has a large impact on the results. Referring back to Figure 4.12, it is clear that the standard deviation of the ionospheric pseudo-observation has a significant affect on the speed with which the ambiguities

converge. The speed of convergence of the ambiguities, in turn, has a direct impact on the mean time to first fix.

For the tests in this section, the filter was reset and ambiguity resolution was attempted every 200 seconds from 7:00 until 22:00 local time, which is the time of peak ionosphere activity. More data was accumulated until either an integer ambiguity set was found and validated, or more than 200 seconds had elapsed. The length of time required to obtain an ambiguity fix was then recorded. While it might be useful to vary the validation threshold, in the following tests, the threshold was kept at 2.0 to enable a meaningful comparison of the positioning scenarios and baseline lengths. The first test shows the time to first fix for a 10 kilometre baseline using the ionosphere weighted model. The standard deviations used for the ionospheric pseudo-observation are the optimal values determined from Figure 5.1. In the following figures, the green dots represent trials where the ambiguity set was fixed correctly, the blue dots represent trials that were unable fix to integer ambiguities within the 200 second trial period, and the red dots represent trials that fixed to an incorrect set of integer ambiguities.

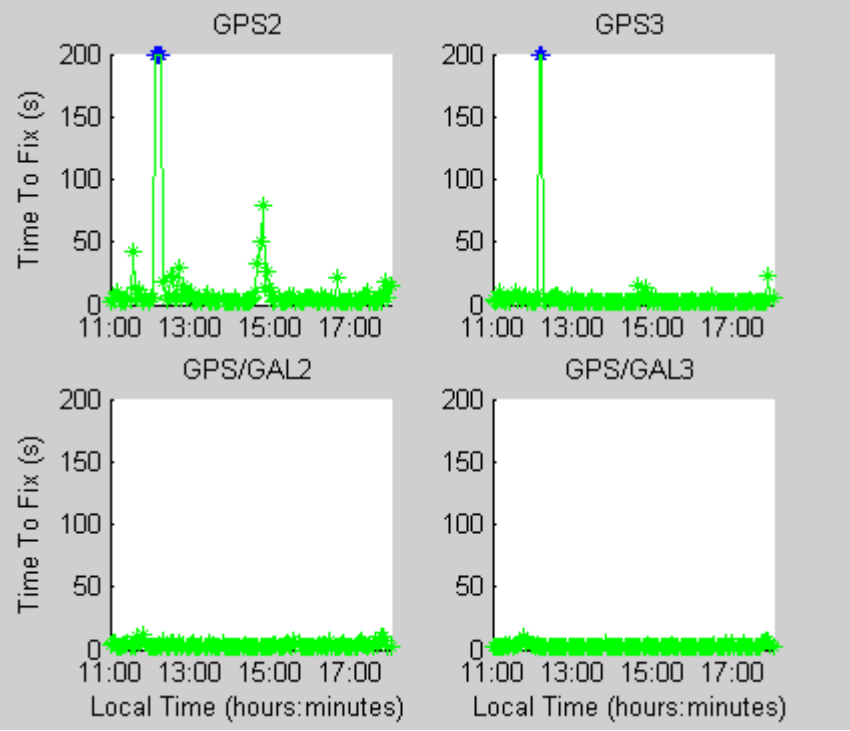

Figure 5.6: Time to First Fix for a 10 km Baseline Using the Ionosphere Weighted Model

The numerical results pertaining to Figure 5.6 are shown below in Table 5.4. The trials that were unable to fix the ambiguities to integer values were omitted from the calculation of the mean time to fix.

Table 5.4: Mean Time To First Fix Results for a 10 km Baseline Using the Ionosphere Weighted Model

	Mean Time To Fix (s)	Percentage of Failed Trials (%)	Percentage of Incorrectly Fixed Trials (%)
GPS2	7.7	3	0
GPS3	3.5	2	0
GPS/GAL2	3.8	0	0
GPS/GAL3	3.0	0	0

It is interesting to note that for the GPS2 scenario, there were no trials that fixed to integer ambiguities between 80 and 200 seconds and only 4 trials that fixed to integers after 30 seconds, but still, there were several trials that did not fix to integers at all. This implies that the filter either fixed to ambiguities very quickly, or not at all. This is understandable when one considers that the weights on the ionospheric constraints were optimized for instantaneous ambiguity resolution. In other words, the optimal values maximize the ability to find the correct ambiguity set instantaneously. As was noted in Chapter Four, a tightly constrained ionospheric model produces superior initial estimates of the ionospheric delays, but the tradeoff with a tight constraint is that the ionospheric estimate does not improve as much as time progresses. Of course, since the ionosphere and ambiguity states are highly correlated, the same behaviour is experienced by the

ambiguity states. This is why using an ionosphere weighted model that was optimized for instantaneous ambiguity resolution allows the ambiguities to be fixed either very quickly or not at all.

The fact that all the tests in this thesis assume a kinematic roving receiver also contributes to the issue of fixing ambiguities quickly or not at all. In a static surveying applications, the baseline states themselves are held fixed, which provides more information to the converging ambiguity states. This in turn improves the speed with which the ambiguities converge. However, in kinematic applications, the baseline states at each epoch are assumed to be largely unknown, which decreases the redundancy of the filter and slows the convergence of the ambiguity states.

With the above discussion in mind, it would be helpful to conduct the same test but using the ionosphere float model instead of the ionosphere weighted model. In this case, the accumulation of time will play a larger role in the ability to fix to integer ambiguities. Figure 5.7 and Table 5.5 show the time to first fix results for a 10 kilometre baseline using the ionosphere float model.

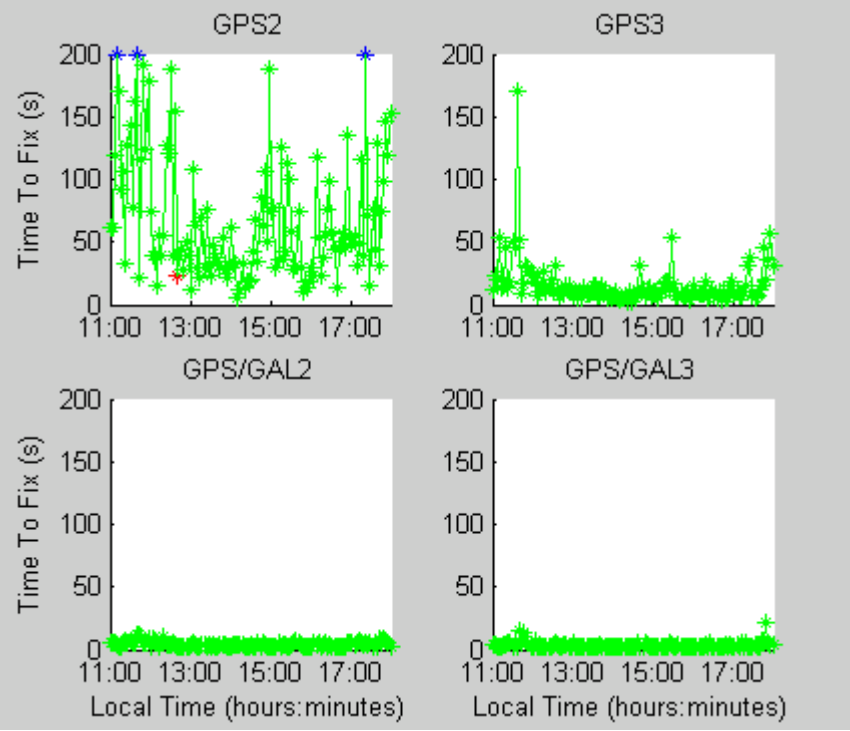

Figure 5.7: Time to First Fix for a 10 km Baseline Using the Ionosphere Float Model

Table 5.5: Mean Time To First Fix Results for a 10 km Baseline Using the Ionosphere Float Model

	Mean Time To Fix (s)	Percentage of Failed Trials (%)	Percentage of Incorrectly Fixed Trials (%)
GPS2	63.7	2	1
GPS3	16.0	0	0
GPS/GAL2	4.4	0	0
GPS/GAL3	3.6	0	0

When using the ionosphere float model, the advantage of including Galileo measurements becomes more evident. The more precise code measurements on the Galileo E5a band allow a faster and more precise convergence of the ionosphere and ambiguity states. Certainly, the GPS2 scenario, which must rely on the noisier GPS C/A code for initial estimation of the ionosphere and ambiguity states, performs the poorest with a mean time to fix of 64 seconds. Another observation from Figure 5.7 is that the inclusion of a third frequency appears to provide a significant improvement from the GPS2 to the GPS3 scenario. As mentioned in the discussion in Section 5.3.2.2, the inclusion of the third frequency improves the redundancy of the positioning problem, which predominantly assists in discriminating between correct and incorrect ambiguity sets. Since the ambiguity validation is improved, it follows that the mean time to first fix performance measure, which is dependent on the ambiguity validation, should also be improved. The improvement borne from adding a third frequency is not as noticeable with the GPS/GAL2 and GPS/GAL3 scenarios because both of these scenarios are already generating perfect ambiguity resolution nearly instantaneously for the 10 kilometre baseline.

Another test was conducted to illustrate the time to first fix results for a longer baseline. An 80 kilometre baseline was processed in the same manner as the 10 kilometre baseline. The ionosphere float model was used because it has already been established that the

float model is optimal for long baselines. Figure 5.8 and Table 5.6 show the results for the GPS/GAL2 and GPS/GAL3 positioning scenarios.

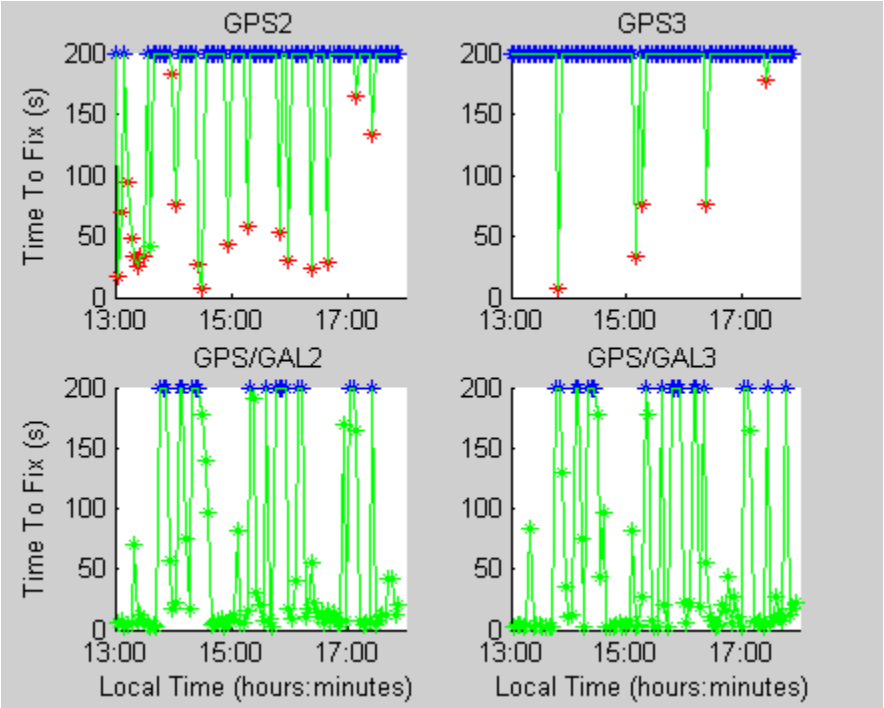

Figure 5.8: Time to First Fix for an 80 km Baseline Using the Ionosphere Float Model

Table 5.6: Mean Time To First Fix for an 80 km Baseline Using the Ionosphere Float Model

	Mean Time To Fix (s)	Percentage of Failed Trials (%)	Percentage of Incorrectly Fixed Trials (%)
GPS2	71.7	75	97
GPS3	80.3	95	100
GPS/GAL2	29.4	24	0
GPS/GAL3	23.8	25	0

For the 80 kilometre baseline the GPS2 and GPS3 scenarios are completely inadequate for resolving the integer vector of ambiguities. The GPS2 scenario finds the correct ambiguity set once; whereas the GPS3 scenario never finds the correct ambiguity set. Despite the absence of a single correct ambiguity set being found, it is still reasonable to conclude that the GPS3 scenario performs better than the GPS2 scenario in terms of ambiguity validation because of the fewer number of incorrect ambiguity sets that were accepted. Similarly, the GPS/GAL3 scenario performs better than the GPS/GAL2 scenario as seen in the improved mean time to first fix when the third frequency is included. It is also made clear that the GPS/GAL2 and GPS/GAL3 scenarios are far more successful than the GPS2 and GPS3 scenarios at finding and validating the correct ambiguity set. This is largely due to the increased number of visible satellites and the

more precise Galileo E5a pseudorange measurements which enables faster and more precise estimation of the ionospheric states.

5.4 Summary

After explaining the theory and current trends in integer ambiguity searching and ambiguity validation, experimental test results have been shown in both of these topics. It was found that the ability to find the correct integer set with the GPS2 and GPS3 scenarios was very sensitive to the choice of standard deviation of the ionospheric pseudo-observation. This dependence was less crucial for the GPS/GAL2 and GPS/GAL3 scenarios because the code precision and satellite geometry improvements associated with these scenarios enable very fast and precise estimates of the ionospheric delays, which makes an ionospheric constraint somewhat superfluous. Nevertheless, for the GPS2 and GPS3 scenarios, optimal values of the standard deviation of the ionospheric pseudo-observation were determined through trial-and-error. The optimal values displayed in Figure 5.1 are specific to periods of the diurnal ionosphere cycle where peak ionospheric activity is experienced. These optimal values are optimal in the context of instantaneous ambiguity resolution and are not necessarily optimal if longer observational time spans are available.

The ability to validate ambiguity sets for each positioning scenario was also scrutinized. It was found that the ability to successfully validate ambiguity sets was greatly affected by the level of ionospheric activity. In this analysis, the benefit of using triple frequency over dual frequency data was witnessed. Even though, the inclusion of a third frequency does not seem to significantly affect the ability to find the correct ambiguity set, the increased redundancy generated by the third frequency improves the ability to validate correct ambiguity sets.

Finally the speed with which integer ambiguity resolution could be accomplished was tested for a 10 kilometre baseline and an 80 km baseline. It was found that the GPS/GAL2 and GPS/GAL3 scenarios performed significantly better than the GPS2 or the GPS3 scenarios. This is largely due to the increased number of satellites and the presence of the more precise Galileo E5a pseudorange measurement which enable faster and more precise ionospheric estimation. In addition, the benefits of the third frequency were once again witnessed as the triple frequency scenarios both performed better than their dual frequency counterparts in terms of being able to successfully validate potential ambiguity sets.

This chapter has accomplished the third minor objective of this thesis which was to provide a realistic and quantitative analysis of the reliability of ambiguity resolution with future GNSS signals. The next chapter will draw on the conclusions of this chapter and

the preceding chapter to explore an alternative technique for processing future GNSS measurements.

Chapter Six: Linear Combinations of Future GNSS Signals

Linear combinations of GPS observations have been used for a variety of different reasons since the inception of GPS. A generic linear combination of data is described by

$$\phi_* = B\phi \qquad (3.2)$$

where ϕ_* is the *m-by-1* vector of transformed observations, ϕ is the *n-by-1* original vector of observations, and B is the transformation matrix. While linear combinations of data are already in widespread use today, the introduction of the third GPS frequency and Galileo will increase the number of choices of combination matrices that may be useful. This chapter discusses the motivation in using linear combinations of data and explains the characteristics of different categories of linear combinations. In addition, the criteria for choosing an *optimal* combination of data are explored and test results using some useful linear combinations of future data are shown.

6.1 Motivation for Using Linear Combinations of GNSS Data

There are three main motivations for using linear combinations of data. The first motivation is that linear combinations can eliminate or mitigate unwanted terms in the mathematical model that are correlated among the observations. If the functional model

was completely known and the stochastic model was perfectly accurate, using linear combinations of data would have no effect on the parameter estimation. Needless to say, this is not usually the case and using linear combinations of data allows one to ignore nuisance parameters without sacrificing the accuracy of the parameters of interest. For example, the double difference, which is a simple linear combination of the original undifferenced observations, eliminates the receiver and satellite clock biases and greatly mitigates spatially correlated error sources. Another example that will be discussed in more detail in this chapter is the ionosphere-free combination which combines double differences from different frequencies in order to eliminate any unmodeled ionospheric delays. From this perspective, linear combinations of data can be seen as an alternative processing strategy to the technique discussed so far in this thesis. In Chapter Two, Chapter Four and Chapter Five, the ionospheric delays were included in the state vector as additional states to be estimated. In this chapter, the ionospheric delays will not be included in the state vector because the effect of the ionospheric errors is reduced using an appropriately chosen linear combinations. This enables one to ignore the ionospheric delays as negligible sources of Gaussian random error that can be included in the measurement covariance model.

A second motivation for using linear combinations of data is to alleviate the computational burden of processing multi-frequency GNSS data. The LAMBDA technique for integer ambiguity searching (Teunissen, 1998) employs a linear

combination of the carrier phase ambiguities to transform the original correlated ambiguity set into a set of less correlated ambiguities. This reduces the integer search space, making the search process faster. Another example of using linear combinations of data to alleviate the computational burden is found in using the widelane combination of L1 and L2 GPS carrier phase observations. By combining the L1 and L2 observations into a single widelane observation, the computational load is improved because there is only one ambiguity to search for, rather than two, and only half the number of observations. The widelane combination also helps to decorrelate the ambiguities and reduce the necessary integer ambiguity search space.

The third motivation for using linear combinations of data is to reduce the communication bandwidth needed for the transmission of GNSS observations. This motivation is most applicable to GPS networks used for real-time positioning and cellular phone applications. By combining the observations from different frequencies into a single observation before transmission, dual-frequency information can be transmitted between sites using the same bandwidth that would be required for a single-frequency observation.

Using a linear combination of the carrier phase data effectively changes the measurement model from a model with the original measurements to one with the combined measurements. As a result, it is important to understand how linear combinations affect

the measurement model and how this in turn affects the final precision of the estimated states. The next section explains how the measurement covariance matrix is affected by linear combinations.

6.2 Transformation of the Measurement Covariance Matrix

In the case of modernized triple frequency GPS, there will be carrier phase measurements available on three frequencies: L1, L2, and L5. The following development also applies directly to triple frequency Galileo where the L1 subscripts are replaced with E1, the L2 subscripts are replaced with E5a, and the L5 subscripts are replaced with E5b.

The dominant source of correlation between GNSS observations is found between observations to the same satellite on different frequencies. Consequently, the most benefit will be realized when creating linear combinations out of signals from the same satellite on different frequencies. A single linear combination of the three carrier signals from one satellite is given as,

$$\phi_* = \begin{bmatrix} a & b & c \end{bmatrix} \begin{bmatrix} \phi_{L1} \\ \phi_{L2} \\ \phi_{L5} \end{bmatrix} \qquad (6.1)$$

where *a*, *b*, and *c*, are the combination coefficients, ϕ_* is the combined measurement in cycles and ϕ_{L1}, ϕ_{L2}, and ϕ_{L5} are the original measurements in cycles. The linear transformation described in Equation (6.1) differs from the transformations used in the LAMBDA technique because the LAMBDA transformation matrix transforms an *n*-dimensional vector of ambiguities into a different, less correlated set of *n* ambiguities. In that way, the ambiguities referring to the original observations can be resolved to integer values by reversing the transformation. In this analysis, however, all three of the observations from one satellite are combined into a single pseudo-observation. This technique prevents the resolution of the original L1, L2, and L5 ambiguities, but reparameterizes the problem so that the ambiguities of the combined observation can be fixed instead.

Applying the law of error propagation to Equation (6.1) yields the accuracy of the combined signal in units of cycles squared.

$$\sigma_*^2 = \begin{bmatrix} a & b & c \end{bmatrix} \begin{bmatrix} \sigma_{L1}^2 & \sigma_{L1,L2} & \sigma_{L1,L5} \\ \sigma_{L2,L1} & \sigma_{L2}^2 & \sigma_{L2,L5} \\ \sigma_{L5,L1} & \sigma_{L5,L2} & \sigma_{L5}^2 \end{bmatrix} \begin{bmatrix} a \\ b \\ c \end{bmatrix} \qquad (6.2)$$

where σ_*^2 is the variance of the combined observation in squared cycles, and σ_{Li}^2 and $\sigma_{Li,Lj}$ are the variances and covariances of the original measurements in squared cycles.

The middle term on the right hand side of Equation (6.2) is the measurement covariance matrix in units of cycles. This measurement covariance matrix was developed in units of metres in Chapter Two as Equation (2.34). Scaling Equation (2.34) to cycles yields,

$$\begin{bmatrix} \sigma_{L1}^2 & \sigma_{L1,L2} & \sigma_{L1,L5} \\ \sigma_{L2,L1} & \sigma_{L2}^2 & \sigma_{L2,L5} \\ \sigma_{L5,L1} & \sigma_{L5,L2} & \sigma_{L5}^2 \end{bmatrix} = \frac{\sigma_{I_{L1}}^2}{\lambda_{L1}^2} \cdot \begin{bmatrix} 1 \\ f_{L1}/f_{L2} \\ f_{L1}/f_{L5} \end{bmatrix} \begin{bmatrix} 1 & f_{L1}/f_{L2} & f_{L1}/f_{L5} \end{bmatrix} + \sigma_T^2 \begin{bmatrix} 1/\lambda_{L1} \\ 1/\lambda_{L2} \\ 1/\lambda_{L5} \end{bmatrix} \begin{bmatrix} 1/\lambda_{L1} & 1/\lambda_{L2} & 1/\lambda_{L5} \end{bmatrix} + \frac{\sigma_{n_{L1}}^2}{\lambda_{L1}^2} \cdot I_3 \qquad (6.3)$$

where $\sigma_{I_{L1}}^2$, σ_T^2, $\sigma_{n_{L1}}^2$ are the variances of the ionosphere, troposphere, and noise/multipath on the L1 frequency in units of square metres and I_3 is a three-dimensional identity matrix. Substituting Equation (6.3) into Equation (6.2) gives the variance of the combined signal in units of squared cycles.

$$\sigma_*^2 \left[cyc^2 \right] = \begin{bmatrix} \sigma_{I_{L1}}^2 & \sigma_T^2 & \sigma_{n_{L1}}^2 \end{bmatrix} \begin{pmatrix} \frac{f_{L1}^2}{\lambda_{L1}^2} \left(\frac{a}{f_{L1}} + \frac{b}{f_{L2}} + \frac{c}{f_{L5}} \right)^2 \\ \frac{1}{\lambda_*^2} \\ \frac{1}{\lambda_{L1}^2} \left(a^2 + b^2 + c^2 \right) \end{pmatrix} \qquad (6.4)$$

where f_{Li} is the frequency in Hz and $\left[cyc^2\right]$ has been added to clarify the units of squared cycles. To scale this to the measurement error in units of metres squared, it is multiplied by the squared wavelength of the combined signal.

$$\sigma_*^2\left[m^2\right] = \lambda_*^2\sigma_*^2\left[cyc^2\right] = \left(\frac{c}{af_{L1} + bf_{L2} + cf_{L5}}\right)^2 \sigma_*^2\left[cyc^2\right] = \left(\frac{\lambda_{L1}\lambda_{L2}\lambda_{L5}}{a\lambda_{L2}\lambda_{L5} + b\lambda_{L1}\lambda_{L5} + c\lambda_{L2}\lambda_{L5}}\right)^2 \sigma_*^2\left[cyc^2\right] \tag{6.5}$$

Therefore the variance of the combined signal in units of meters squared is given by:

$$\sigma_*^2\left[m^2\right] = \begin{bmatrix}\sigma_{I_{L1}}^2 & \sigma_T^2 & \sigma_{n_{L1}}^2\end{bmatrix} \begin{pmatrix} \frac{f_{L1}^4}{f_*^2}\left(\frac{a}{f_{L1}} + \frac{b}{f_{L2}} + \frac{c}{f_{L5}}\right)^2 \\ 1 \\ \frac{\lambda_*^2}{\lambda_{L1}^2}\left(a^2 + b^2 + c^2\right) \end{pmatrix} \tag{6.6}$$

These equations show that the accuracy of the combined signal is essentially a weighted sum of the ionospheric, tropospheric, and noise/multipath errors. The individual error components, $\begin{bmatrix}\sigma_{I_{L1}}^2 & \sigma_T^2 & \sigma_{n_{L1}}^2\end{bmatrix}$, are very difficult to model well because they depend on many factors in the physical environment. For example, the ionospheric error variance depends on the existing ionospheric activity and the baseline length; the tropospheric error variance depends on the accuracy of the tropospheric model, the height difference

between the receivers, and the baseline length; and the noise/multipath error variance depends on the quality and bandwidth of the receivers, the location and angle of any nearby reflectors, and the gain pattern of the antenna. And all the error variances are a function of the elevation angle to the satellites. Not only are these terms difficult to model for a single epoch in time, but they also change with time as the satellite geometry, the atmospheric conditions, and the receiver location changes.

The weights applied to these error sources depend only on the choice of coefficients (*a*, *b*, and *c*) used in creating the combination and the constant nominal frequencies of the carrier signals, which are given in Table 6.1. These weights are often referred to as amplification factors since they amplify (or reduce) the errors that would apply to an untransformed signal. For a given GPS positioning campaign, different choices of *a*, *b*, and *c* will yield vastly different accuracies. The next three sections discuss combination coefficients that cause the greatest reduction of the three categories of error sources.

Table 6.1: GPS and Galileo Nominal Frequencies (from Navstar GPS Space Segment / Navigation User Interfaces (ICD) (1997) and Galileo Mission Requirements Document Issue 5.0 – Draft (2000))

GNSS Type	Frequency	Fundamental Frequency (MHz)	Integer Multiplier	Nominal Frequency (MHz)
GPS	L1	10.23	154	1575.42
	L2	10.23	120	1227.60
	L5	10.23	115	1176.45
Galileo	E1	10.23	154	1575.42
	E5a	10.23	115	1176.45
	E5b	10.23	118	1207.14

6.3 Combinations that Eliminate the Effect of the Ionosphere

Since the ionosphere is a dispersive medium, the ionospheric delays experienced by each carrier phase measurement have a known relationship between them, which was given in Equation (2.26). Therefore, it is possible to choose combination coefficients that completely eliminate the effect of the ionosphere. Only two frequencies are needed to eliminate the ionospheric error to the first order, so any two of three frequencies in a

given satellite system can be used to generate an ionosphere-free combination. For an example, the ionosphere-free combination of Galileo E1 and E5a frequencies will be developed. Starting with Equation (6.1), the carrier phase measurement can be expanded into

$$\phi_* = \frac{\rho}{\lambda_*} + \left(a + b\frac{f_{E1}}{f_{E5a}} + c\frac{f_{E1}}{f_{E5b}} \right) \delta I_{E1}^{cyc} + N_* \qquad (6.7)$$

where ϕ_* is the carrier phase observation in cycles, ρ is the geometric range, δI_{E1}^{cyc} is the residual ionospheric delay on the E1 frequency in units of cycles, $N_* = aN_{E1} + bN_{E5a} + cN_{E5b}$ is the combined integer ambiguity term and the remaining sources of error are considered negligible. In order to eliminate the effect of the ionosphere, the following condition must be satisfied.

$$a + b\frac{f_{E1}}{f_{E5a}} + c\frac{f_{E1}}{f_{E5b}} = 0 \qquad (6.8)$$

This equation describes a plane so it has infinite solutions. Any values of *a*, *b*, and *c* that lie on this plane represent an ionosphere-free combination and the closer a combination is to the plane, the smaller the ionosphere amplification factor will be. Only two frequencies are required to eliminate the effect of the ionosphere so one of the coefficients can be set to zero. For the example using only the Galileo E1 and E5a

frequencies, c is set to zero and the solution lies along the line $a = -b\frac{f_{E1}}{f_{E5a}} = -b\frac{154}{115}$. In order to maintain the integer nature of the combination coefficients and an effective wavelength greater than zero, the solution with the lowest values of b and c is $\begin{bmatrix} a & b & c \end{bmatrix} = \begin{bmatrix} 154 & -115 & 0 \end{bmatrix}$. It is desirable to use the smallest possible coefficients (in an absolute sense) because larger coefficients amplify the noise and multipath errors. This will be discussed further in Section 6.4. Substituting the values for a, b, and c into Equation (6.4) or Equation (6.6) reveals that the ionospheric amplification factor becomes equal to zero, which proves that this combination removes the effect of the ionosphere. Table 6.2 shows all the dual-frequency ionosphere-free combinations for modernized GPS and Galileo signals along with the associated effective wavelengths. These coefficients were found in the same manner as just outlined for the case of the E1 and E5a frequencies.

Table 6.2: Modernized GPS and Galileo Ionosphere-Free Combinations

	a	*b*	*c*	λ (m)	Noise Amplification Factor (length units)
GPS	77	-60	0	0.0063	10.4
$\phi_* = [a \quad b \quad c]\begin{bmatrix}\phi_{L1}\\ \phi_{L2}\\ \phi_{L5}\end{bmatrix}$	154	0	-115	0.0028	8.0
	0	24	-23	0.1247	474.5
Galileo	154	-115	0	0.0028	8.0
$\phi_* = [a \quad b \quad c]\begin{bmatrix}\phi_{E1}\\ \phi_{E5a}\\ \phi_{E5b}\end{bmatrix}$	77	0	-59	0.0060	9.3
	0	-115	118	0.0419	1317.8

Even though each of the ionosphere-free combinations will completely eliminate the effects of the ionosphere, it is clear that they will not all provide the same results. The ionosphere-free combinations using L2 and L5 frequencies for GPS and E5a and E5b for Galileo have larger wavelengths, which makes integer ambiguity resolution easier with these combined signals. However, these same ionosphere-free combinations will provide the worst final position results because of the amplification of the noise and multipath. To demonstrate this phenomenon with simulated processing results, five minutes of data from a 50 kilometre baseline was processed using the software described in Chapter Three. First, the data was processed in float ambiguity mode and the ambiguity estimation error and three-dimensional position error of the float solution are plotted in

the upper two panes of Figure 6.1 for GPS and Figure 6.2 for Galileo. Next, the same data was processed again, but fixing the ambiguities to the correct integer values. In this case, the three dimensional position errors are plotted in the lower panes of the same figures. The standard deviation of the position errors are also shown for the fixed position error plots.

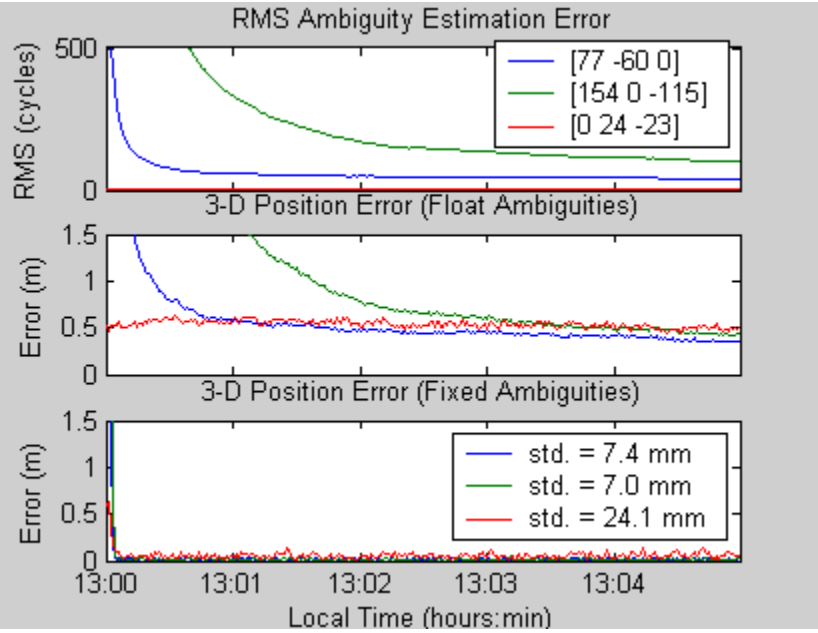

Figure 6.1: Ambiguity Estimation Error and Fixed Position Error for GPS Ionosphere-Free Combinations

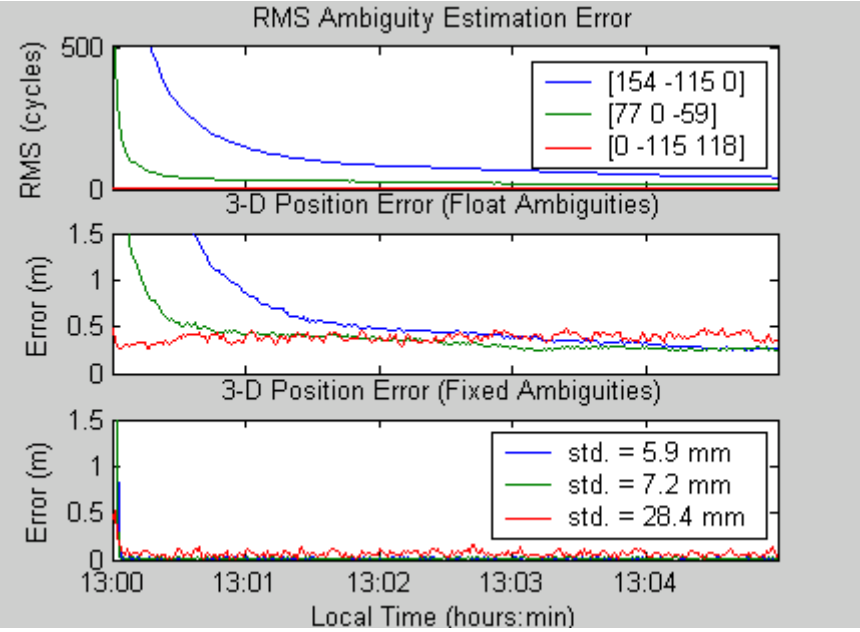

Figure 6.2: Ambiguity Estimation Error and Fixed Position Error for Galileo Ionosphere-Free Combinations

From the processing results, it is clear that the L2/L5 and E5a/E5b ionosphere-free combinations provide the best float ambiguity estimation error, which would make fixing integer ambiguities easier with these combinations. However, the same combinations also display far worse final position accuracy when they are used in fixed ambiguity mode as evidenced by the significantly worse fixed position error standard deviations.

6.4 Combinations that Reduce the Effect of Thermal Noise and Multipath

According to Equation (6.4), any combination of data will amplify the effect of thermal noise and multipath in units of cycles since the following inequality is always true for any set of integer combination coefficients (except the null set).

$$\frac{1}{\lambda_{L1}^2}\left(a^2 + b^2 + c^2\right) \geq 1 \qquad (6.9)$$

The only way to minimize the amplification of noise in units of cycles is to use the original untransformed observations. However, there are some combinations of data that greatly reduce the effect of noise and multipath when parameterized in length units. The following equation shows the amplification factor in length units for the noise and multipath components for a combined signal.

$$\sigma_*^2\left[m^2\right] = \left\{\frac{\lambda_*^2}{\lambda_{L1}^2}\left(a^2 + b^2 + c^2\right)\right\}\sigma_{L1}^2\left[m^2\right] \qquad (6.10)$$

Many commercial dual-frequency GPS processing software packages use the narrowlane combination ($\begin{bmatrix} a & b \end{bmatrix} = \begin{bmatrix} 1 & 1 \end{bmatrix}$) to provide an observable that is less affected by noise and multipath. The wavelength of the narrowlane combination is only 10.7 cm so in order to

use a fixed integer narrowlane observable, long observation time spans, short baselines or previously fixed L1 and L2 ambiguities are required. The noise and multipath amplification factor for the narrowlane combined observation is 0.63, which means that the noise and multipath error is improved by 37% over the L1 only carrier phase observation. In addition to the short wavelength, another one of the tradeoffs for having improved noise and multipath characteristics is that the narrowlane observation amplifies the ionospheric error in length units by a factor of 1.65. For this reason, the narrowlane observation should only be used on short baselines where the ionospheric delay is mostly eliminated through double differencing.

There are many other combinations that reduce the effect of the noise and multipath as much as the narrowlane combination and also amplify the effect of the ionosphere less than the narrowlane observable. Table 6.3 shows the GPS combinations with the largest wavelengths that reduce the effects of noise and multipath at least as much as the GPS narrowlane combination. To find these combinations, the noise amplification factors of all the combinations with integer coefficients in the set, $a,b,c \in [-20,20]$**, were computed and compared to the noise amplification factor of the traditional narrowlane observable. Those combinations that had a noise amplification factor less than or equal to the traditional narrowlane observation were sorted according to wavelength and the combinations with the five longest wavelengths are listed in Table 6.3.**

Table 6.4 shows the same thing for Galileo combinations, but instead of comparing to the GPS narrowlane combination, the Galileo narrowlane combination ($\phi_* = \phi_{E1} + \phi_{E5a}$) has been used.

Table 6.3: Noise and Multipath Reducing Combinations for Triple Frequency GPS

a	*b*	*c*	Noise Amplification Factor (length units)	Ionosphere Amplification Factor (length units)	Wavelength (m)
1	1	0	0.63	1.65	0.107
1	1	1	0.47	2.06	0.075
1	1	2	0.56	2.30	0.058
1	2	1	0.55	2.20	0.058
2	1	1	0.48	1.72	0.054

Table 6.4: Noise and Multipath Reducing Combinations for Triple Frequency Galileo

a	*b*	*c*	Noise Amplification Factor (length units)	Ionosphere Amplification Factor (length units)	Wavelength (m)
1	1	0	0.66	1.79	0.109
1	0	1	0.64	1.70	0.108
1	1	1	0.48	2.10	0.076
2	0	1	0.65	1.43	0.069
1	2	1	0.56	2.34	0.058

To test these combinations in a processing scenario, five minutes of data over a five kilometre baseline was processed in kinematic mode with fixed integers using the software described in Chapter Three. To emphasize the reduction of the thermal noise and multipath errors, these error sources were increased to simulate a lower quality receiver and a slightly higher multipath environment. The resulting variance and mean of the three-dimensional position errors are plotted in Figure 6.3 for each GPS and Galileo combination. The x-axis labels on the figure represent the combination where each integer is a combination coefficient; for example [211] means that *a*, *b*, and *c* were set to 2, 1, and 1 respectively).

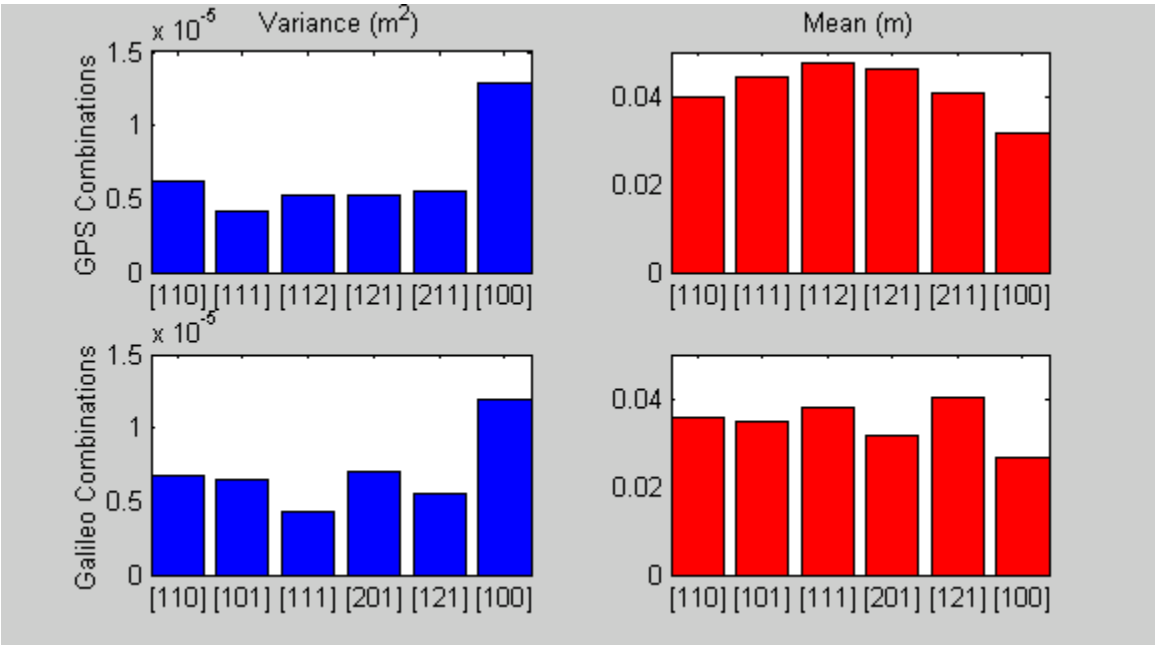

Figure 6.3: Variance and Mean of the Three-Dimensional Position Error Using Noise and Multipath Reducing Combinations

As expected from the calculated amplification factors, each of the noise reducing combinations produce position errors with variances around half the magnitude of the L1 only position error variance. It is also interesting to notice that the L1 only processing results have a mean that is closer to zero than any of the combinations of data. This is because each of the noise reducing combinations has the disadvantage of amplifying the effect of the ionosphere, which causes a greater bias than if L1 only data were used. None of the combinations listed in the preceding tables stands out as being appreciably more useful than the traditional narrowlane combination. This implies that in situations where dual-frequency ambiguities could already be resolved to integer values, the

additional third frequency will not significantly help in improving the final positioning accuracy.

6.4.1 The Noise Reduction Limit

It is nearly impossible to directly resolve integer ambiguities for any of the noise and multipath reducing combinations. The primary use of noise and multipath reducing combinations is when the untransformed ambiguities (e.g. L1, L2, and L5) have already been resolved to integer values. If the untransformed ambiguities are already known, it is not necessary to constrain the choice of combinations to those combinations that have the largest wavelengths. Instead, one can focus on combinations that provide the largest reduction in the noise and multipath errors.

The noise and multipath errors cannot be completely eliminated like the ionospheric effect can, but there is an absolute minimum for the noise and multipath amplification factor in length units. The remainder of this section proves that there is a limit and shows the combination coefficients that generate this limit. The following proof begins by using only GPS frequencies, but will be generalized for GPS or Galileo in the ensuing discussion.

Starting with Equation (2.33), we first apply the assumption that the variance of each carrier signal is equal in units of cycles.

$$\begin{bmatrix} \sigma_{n_{L1}}^2 & 0 & 0 \\ 0 & \sigma_{n_{L2}}^2 & 0 \\ 0 & 0 & \sigma_{n_{L5}}^2 \end{bmatrix} = \frac{\sigma_{n_{L1}}^2}{\lambda_{L1}^2} \begin{bmatrix} \lambda_{L1}^2 & 0 & 0 \\ 0 & \lambda_{L2}^2 & 0 \\ 0 & 0 & \lambda_{L5}^2 \end{bmatrix} \qquad (2.33)$$

where $\sigma_{n_{L1}}^2$ is the variance due to noise and multipath on the L1 signal in units of metres.

Next the linear combination coefficients are applied vis-à-vis Equation (6.1), but with length units instead of units of cycles.

$$\Phi_* = \begin{bmatrix} \alpha & \beta & \gamma \end{bmatrix} \begin{bmatrix} \Phi_{L1} \\ \Phi_{L2} \\ \Phi_{L5} \end{bmatrix} \qquad (6.11)$$

where Φ is the carrier phase measurement scaled to metres and

$$\alpha = a \frac{\lambda_*}{\lambda_{L1}} \qquad (6.12)$$

$$\beta = b \frac{\lambda_*}{\lambda_{L2}} \qquad (6.13)$$

$$\gamma = c\frac{\lambda_*}{\lambda_{L5}} \qquad (6.14)$$

Based on these equations, it is true that,

$$\alpha + \beta + \gamma = 1 \qquad (6.15)$$

Applying the law of propagation of variance to Equation (6.11) and only including the noise and multipath components of the error model, yields

$$\sigma_*^2[m^2] = \left\{\frac{1}{\lambda_{L1}^2}\left(\alpha^2\lambda_{L1}^2 + \beta^2\lambda_{L2}^2 + \gamma^2\lambda_{L5}^2\right)\right\}\sigma_{L1}^2[m^2] \qquad (6.16)$$

The term in curly brackets is the amplification factor to be minimized. Therefore, the problem is to find values of α, β, and γ subject to the following conditions:

$$\alpha + \beta + \gamma = 1 \qquad (6.15)$$

and

$$\alpha^2\lambda_{L1}^2 + \beta^2\lambda_{L2}^2 + \gamma^2\lambda_{L5}^2 \rightarrow \min \qquad (6.17)$$

This problem can be understood geometrically as finding the point on an ellipsoid described by Equation (6.17) that is tangent to the plane described by Equation (6.15). A two-dimensional representation of this situation is illustrated in Figure 6.4.

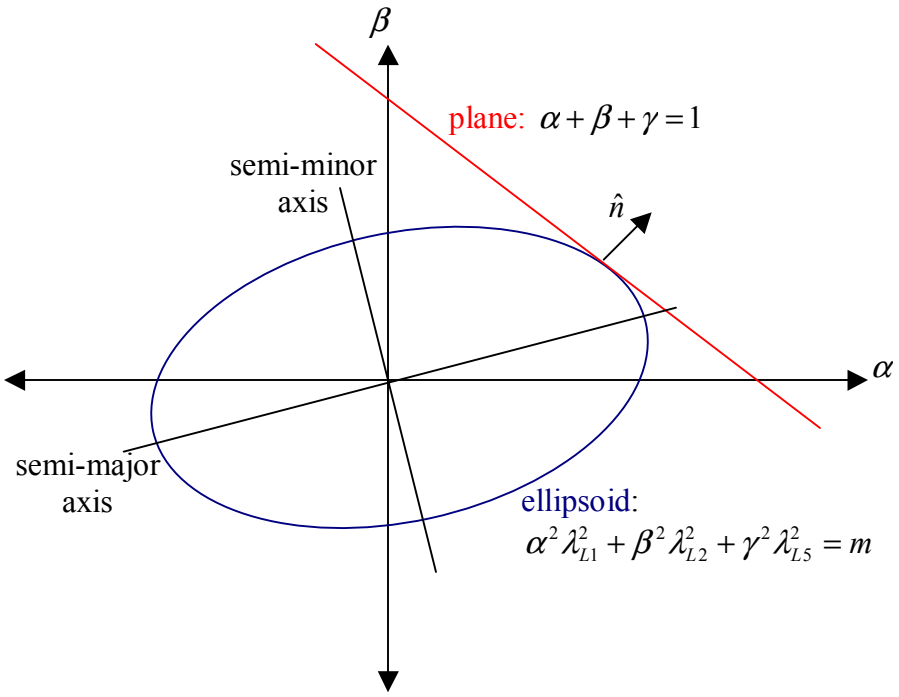

Figure 6.4: Geometrical Representation of a Plane and Ellipsoid (Not to Scale)

One solution to this problem is to find the point on the surface of the ellipsoid where the unit normal vector is parallel to the unit normal vector of the plane. The problem is complicated by the fact that the exact dimensions of the ellipsoid are unknown. The shape of the ellipsoid is known, but the scale of the axes is not. To begin the solution, the

scale of the ellipsoid is set to an unknown variable, *m*, giving the following equation for the ellipsoid.

$$f(\alpha,\beta,\gamma)=\alpha^2\lambda_{L1}^2+\beta^2\lambda_{L2}^2+\gamma^2\lambda_{L5}^2=m \qquad (6.18)$$

The unit normal vector can then be found by computing the gradient of Equation (6.18) and dividing by the magnitude of the gradient.

$$\hat{n}=\frac{\nabla f(\alpha,\beta,\gamma)}{\left|\nabla f(\alpha,\beta,\gamma)\right|} \qquad (6.19)$$

where $\hat{n}$ is the unit normal vector and the ∇ symbolizes the gradient operation.

Substituting Equation (6.18) into Equation (6.19) yields,

$$\hat{n}_{ellipsoid}=\left(\left(\alpha\lambda_{L1}^2\right)^2+\left(\beta\lambda_{L2}^2\right)^2+\left(\gamma\lambda_{L5}^2\right)^2\right)^{-1/2}\cdot\left\langle\alpha\lambda_{L1}^2,\beta\lambda_{L2}^2,\gamma\lambda_{L5}^2\right\rangle \qquad (6.20)$$

It should be noted that the unknown scale of the ellipsoid, *m*, is not present in Equation (6.20). This is understandable intuitively because the unit normal at a given point on the surface of an ellipsoid is constant regardless of the scale of the ellipsoid. This is pictured

in Figure 6.5 for the case of a two-dimensional ellipse. The same principle applies to a three dimensional ellipsoid.

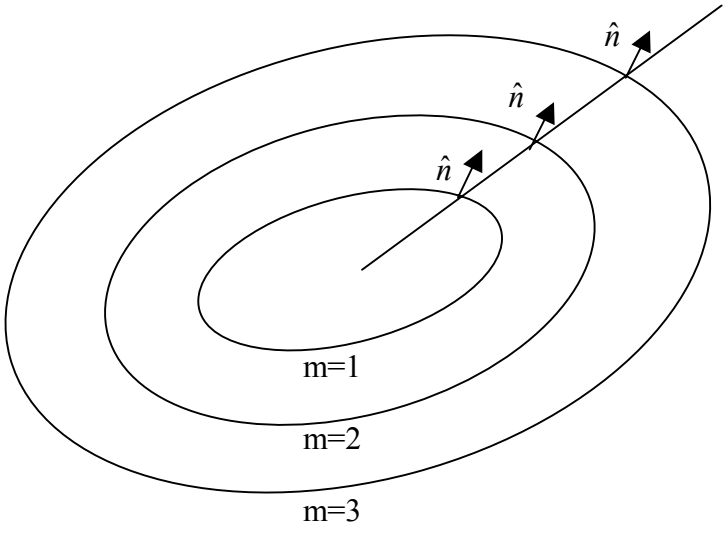

Figure 6.5: Equivalent Unit Normal Vectors for a Family of Ellipses (Not to Scale)

At the point where the ellipsoid is tangent to the plane, the unit normal vector of the ellipsoid is equal to the unit normal vector of the plane. The unit normal vector at any point on the plane is given by:

$$\hat{n}_{plane} = \left\langle \frac{1}{\sqrt{3}}, \frac{1}{\sqrt{3}}, \frac{1}{\sqrt{3}} \right\rangle \qquad (6.21)$$

Equating the unit normal vectors of the plane and the ellipsoid yields a system of three equations and three unknowns:

$$\frac{\alpha\lambda_{L1}^2}{\sqrt{\left(\alpha\lambda_{L1}^2\right)^2+\left(\beta\lambda_{L2}^2\right)^2+\left(\gamma\lambda_{L5}^2\right)^2}}=\frac{1}{\sqrt{3}} \qquad (6.22)$$

$$\frac{\beta\lambda_{L1}^2}{\sqrt{\left(\alpha\lambda_{L1}^2\right)^2+\left(\beta\lambda_{L2}^2\right)^2+\left(\gamma\lambda_{L5}^2\right)^2}}=\frac{1}{\sqrt{3}} \qquad (6.23)$$

$$\frac{\gamma\lambda_{L1}^2}{\sqrt{\left(\alpha\lambda_{L1}^2\right)^2+\left(\beta\lambda_{L2}^2\right)^2+\left(\gamma\lambda_{L5}^2\right)^2}}=\frac{1}{\sqrt{3}} \qquad (6.24)$$

Rearranging the system of equations yields

$$\begin{bmatrix} 2\left(\lambda_{L1}^2\right)^2 & -\left(\lambda_{L2}^2\right)^2 & -\left(\lambda_{L5}^2\right)^2 \\ -\left(\lambda_{L1}^2\right)^2 & 2\left(\lambda_{L2}^2\right)^2 & -\left(\lambda_{L5}^2\right)^2 \\ -\left(\lambda_{L1}^2\right)^2 & -\left(\lambda_{L2}^2\right)^2 & 2\left(\lambda_{L5}^2\right)^2 \end{bmatrix}\begin{bmatrix}\alpha\\ \beta\\ \gamma\end{bmatrix}=\begin{bmatrix}0\\0\\0\end{bmatrix} \qquad (6.25)$$

The solution to this system is given by:

$$\begin{bmatrix}\alpha\\ \beta\\ \gamma\end{bmatrix}=t\cdot\begin{bmatrix}\lambda_{L1}^{-2}\\ \lambda_{L2}^{-2}\\ \lambda_{L5}^{-2}\end{bmatrix} \qquad (6.26)$$

where t is an arbitrary scalar. Equation (6.26) is the equation of the line in Figure 6.5. Therefore, the final task is to find the point at which this line intersects the plane of Equation (6.15). The point is:

$$\begin{bmatrix}\alpha\\ \beta\\ \gamma\end{bmatrix} = \frac{1}{\lambda_{L1}^{-2}+\lambda_{L2}^{-2}+\lambda_{L5}^{-2}}\cdot\begin{bmatrix}\lambda_{L1}^{-2}\\ \lambda_{L2}^{-2}\\ \lambda_{L5}^{-2}\end{bmatrix} = \frac{1}{f_{L1}^{2}+f_{L2}^{2}+f_{L5}^{2}}\cdot\begin{bmatrix}f_{L1}^{2}\\ f_{L2}^{2}\\ f_{L5}^{2}\end{bmatrix} \qquad (6.27)$$

$$= \frac{1}{154^2+120^2+115^2}\cdot\begin{bmatrix}154^2\\ 120^2\\ 115^2\end{bmatrix} \quad \text{for GPS}$$

$$= \frac{1}{154^2+115^2+118^2}\cdot\begin{bmatrix}154^2\\ 115^2\\ 118^2\end{bmatrix} \quad \text{for Galileo}$$

Geometrically, this point describes the point where the ellipsoid with a minimum size is tangent to the plane, $\alpha+\beta+\gamma=1$. In terms of noise and multipath reduction, these combination coefficients (in length units) provide the absolute minimum amplification factor for noise and multipath variance that is possible. In order to convert these combination coefficients in length units into cyclic combination coefficients a, b, and c, Equations (6.12) to (6.14) can be used as a system of three equations with three unknowns. The solution to this system is given by:

$$\begin{bmatrix} a \\ b \\ c \end{bmatrix} = t \cdot \begin{bmatrix} f_{L1} \\ f_{L2} \\ f_{L5} \end{bmatrix} = t \cdot \begin{bmatrix} 154 \\ 120 \\ 115 \end{bmatrix} \text{ for GPS} \qquad (6.28)$$

$$= t \cdot \begin{bmatrix} 154 \\ 115 \\ 118 \end{bmatrix} \text{ for Galileo}$$

where t is an arbitrary scalar.

Therefore, the closer a given combination is to the lines described Equation (6.28), the better the noise and multipath reducing properties would be. Substituting the solution for α, β, and γ into Equation (6.16), or equivalently, substituting the solution for a, b, and c into Equation (6.10), yields the minimum amplification factor of 0.462 for GPS, which corresponds to a reduction in the noise and multipath error variance of 54% relative the original L1 signal. For Galileo combinations, the minimum amplification factor is 0.466, which corresponds to a reduction in the noise and multipath error variance of 53% relative to the E1 signal.

Using exactly the same methodology to find the minimum amplification factor that is possible with combinations of only two frequencies reveals that the minimum noise and amplification factor with two frequencies is 0.622 for GPS L1/L2 and 0.642 for Galileo E1/E5a.

The results of this proof are summarized in Table 6.5 where the *Richert Limit of Noise Reduction* is the absolute greatest reduction in noise and multipath variance relative to the L1 (GPS) or E1 (Galileo) signal that is possible using linear combinations of data.

Table 6.5: Richert Limit of Noise Reduction

GNSS Type	Freq. Used	Combination Coefficients		*Richert Limit of Noise Reduction*
		Length Units: $\Phi_* = [\alpha \quad \beta \quad \gamma]\begin{bmatrix}\Phi_{L1}\\ \Phi_{L2}\\ \Phi_{L5}\end{bmatrix}$	Cycle Units: $\phi_* = [a \quad b \quad c]\begin{bmatrix}\phi_{L1}\\ \phi_{L2}\\ \phi_{L5}\end{bmatrix}$	
GPS	L1 L2 L5	$\begin{bmatrix}\alpha\\ \beta\\ \gamma\end{bmatrix} = \frac{1}{154^2+120^2+115^2}\cdot\begin{bmatrix}154^2\\ 120^2\\ 115^2\end{bmatrix}$	$\begin{bmatrix}a\\ b\\ c\end{bmatrix} = t\cdot\begin{bmatrix}154\\ 120\\ 115\end{bmatrix}$	54%
	L1 L2	$\begin{bmatrix}\alpha\\ \beta\end{bmatrix} = \frac{1}{77^2+60^2}\cdot\begin{bmatrix}77^2\\ 60^2\end{bmatrix}$	$\begin{bmatrix}a\\ b\end{bmatrix} = t\cdot\begin{bmatrix}154\\ 120\end{bmatrix}$	48%
GAL	E1 E5a E5b	$\begin{bmatrix}\alpha\\ \beta\\ \gamma\end{bmatrix} = \frac{1}{154^2+115^2+118^2}\cdot\begin{bmatrix}154^2\\ 115^2\\ 118^2\end{bmatrix}$	$\begin{bmatrix}a\\ b\\ c\end{bmatrix} = t\cdot\begin{bmatrix}154\\ 115\\ 118\end{bmatrix}$	53%
	E1 E5a	$\begin{bmatrix}\alpha\\ \beta\end{bmatrix} = \frac{1}{154^2+115^2}\cdot\begin{bmatrix}154^2\\ 115^2\end{bmatrix}$	$\begin{bmatrix}a\\ b\end{bmatrix} = t\cdot\begin{bmatrix}154\\ 115\end{bmatrix}$	46%

It should be reiterated that the results in Table 6.5 rely on the assumption that the noise and multipath variances are equivalent in units of cycles for each carrier signal. For most

GNSS receivers, this assumption is valid. However, for a unique receiver for which this assumption is may not be true, the proof is still applicable, but the shape of the ellipsoid would be different to reflect the different covariance matrix of the observations.

The interesting conclusion from this section is that the availability of a third frequency will allow for combinations that can reduce the effect of noise and multipath better than the reduction that is currently available with only two frequencies; albeit, this improvement is marginal.

6.5 Combinations that Reduce the Effect of the Troposphere

In units of length, the choice of combination coefficients does not affect how the combined signal is delayed due to the troposphere. This is understandable intuitively because the troposphere is not a dispersive medium for signals in the L-band, which means that it biases all GNSS signals by the same amount. Mathematically, the amplification factor for the tropospheric variance in metres is equal to one as shown in the following proof.

$$\sigma_*^2\left[m^2\right] = \lambda_*^2\sigma_*^2\left[cyc^2\right] = \lambda_*^2\left(\frac{1}{\lambda_*^2}\sigma_{L1}^2\left[m^2\right]\right) = \sigma_{L1}^2\left[m^2\right] \qquad (6.29)$$

However, in units of cycles, the choice of combination coefficients does impact the effect of the tropospheric error on the combined observation. Simply put, the longer the effective wavelength of the combined signal, the less the tropospheric error will bias the measurement in units of cycles. This same rule of thumb also applies for orbital errors or any other error source that changes all carrier phase measurements by the same amount in length units. As a matter of interest, it is possible to have a troposphere-free combination when the wavelength of the combined signal approaches infinity. However, such combinations have no use in practice since the wavelength is undefined. Combinations that eliminate the effect of the troposphere cause the denominator of Equation (6.5) to be equal to zero.

$$af_{L1} + bf_{L2} + cf_{L5} = 0 \qquad \text{GPS} \tag{6.30}$$
$$af_{E1} + bf_{E5a} + cf_{E5b} = 0 \qquad \text{Galileo}$$

Like Equation (6.8), which describes the plane of ionosphere-free combinations, Equation (6.30) describes a plane of troposphere-free combinations. Some of the choices of *a*, *b*, and *c* that satisfy Equation (6.30) are listed in Table 6.6.

Table 6.6: Theoretical Troposphere-Free Combinations

	a	*b*	*c*	λ (m)	Noise Amplification Factor (length units)
GPS	60	-77	0	∞	∞
$\phi_* = [a \quad b \quad c]\begin{bmatrix}\phi_{L1}\\ \phi_{L2}\\ \phi_{L5}\end{bmatrix}$	115	0	-154	∞	∞
	0	23	-24	∞	∞
Galileo	115	-154	0	∞	∞
$\phi_* = [a \quad b \quad c]\begin{bmatrix}\phi_{E1}\\ \phi_{E5a}\\ \phi_{E5b}\end{bmatrix}$	59	0	-77	∞	∞
	0	-118	115	∞	∞

It is interesting to note that the plane of troposphere-free combinations given by Equation (6.30) is orthogonal to the line of maximum noise reduction given by Equation (6.28). This geometrical fact confirms the well established notion that combinations with larger wavelengths cause greater amplification of the noise and multipath in units of metres.

6.6 Optimal Combinations of Future GNSS Data

The previous three sections have outlined how the negative effects of individual error sources can be mitigated based on the choice of the combination coefficients used. It was

found that no error source could be eliminated without surrendering a degradation of the other error sources. Table 6.7 summarizes the advantages and disadvantages of the combinations that were detailed in Sections 6.3 through 6.5.

Table 6.7: Advantages and Disadvantages of Various Types of Linear Combinations

Combination Type	Advantages	Disadvantages
Ionosphere-free	• Ionospheric error is eliminated	• Difficult or impossible to resolve integer ambiguities in most applications due to short wavelengths • Effect of noise and multipath is amplified
Noise and Multipath reducing	• Effects of noise and multipath are reduced	• Difficult to resolve integer ambiguities due to short wavelength • Effect of ionosphere is amplified
Troposphere reducing	• Effect of the troposphere errors are mitigated • Easier to resolve integer ambiguities due to long wavelength	• Effects of noise and multipath are amplified

In real GNSS positioning scenarios, all the individual sources of error exist to some extent so it is conceivable that there is an optimal set of combination coefficients for each

positioning campaign. The ultimate goal is to choose a combination that allows for successful integer ambiguity resolution and gives the best possible position accuracy. A definition of optimality was given in Radovanovic et al. (2001) where it was stated that "*an optimal combination is one that minimizes the total error variance in meters², while maintaining an error variance in cycles² that is at least equal to that of the L1 observable.*" According to this definition, the optimal choice of combination coefficients will be different for different baseline lengths, different proportions of the various error sources, and different user requirements.

Referring back to Section 6.2, the variance of a triple frequency GPS combined signal in units of cycles is given by Equation (6.4). In units of cycles, the variance will be minimized if the combination coefficients represent a point in integer space that is close to:

1. the plane of ionosphere-free combinations, $a + b\frac{f_{L1}}{f_{L2}} + c\frac{f_{L1}}{f_{L5}} = 0$
2. the plane of troposphere-free combinations, $af_{L1} + bf_{L2} + cf_{L5} = 0$
3. the origin (0,0,0)

This minimization problem is illustrated in Figure 6.6.

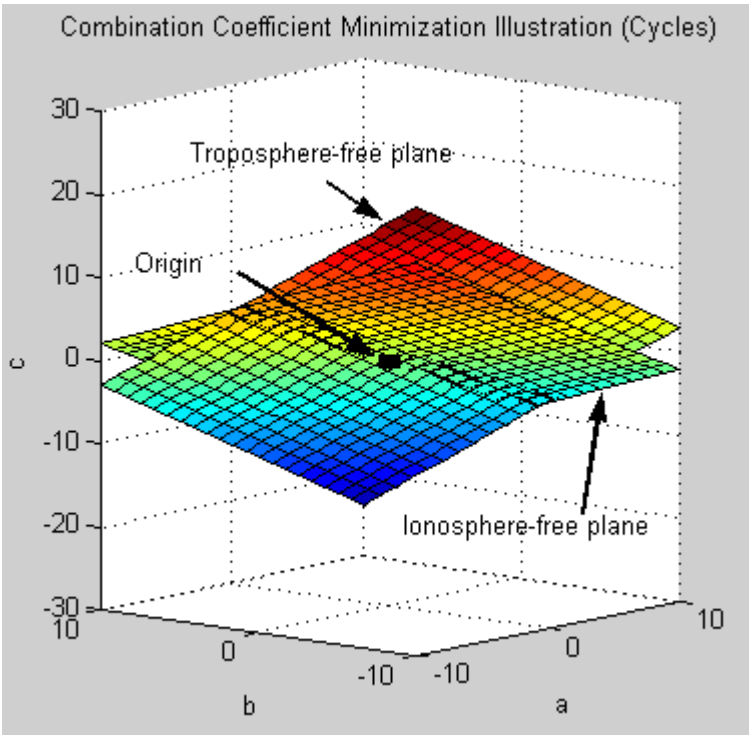

Figure 6.6: Equations Minimizing the Combined Signal Variance in Units of Cycles

The angle between the troposphere-free plane and the ionosphere-free plane is given by:

$$\theta = \cos^{-1}\left(\frac{\mathbf{n}_{tropo} \bullet \mathbf{n}_{iono}}{|\mathbf{n}_{tropo}||\mathbf{n}_{iono}|}\right) = 14.6^{\circ} \quad \text{for GPS} \qquad (6.31)$$

$$= 15.0^{\circ} \quad \text{for Galileo}$$

where $\mathbf{n}_{tropo}$ and $\mathbf{n}_{iono}$ are the normal vectors of the two planes.

An optimal combination in terms of minimizing the variance in units of cycles depends on the magnitude of each individual error source. For example, for a long baseline, the ionosphere and troposphere might be the dominant error sources. In this case, it is more important that the optimal combination be close to the ionosphere-free and troposphere-free planes than to the origin. However, for a short baseline, the ionosphere and troposphere would be almost completely eliminated through double differencing. In this case, the dominant source of error would likely be the thermal noise and multipath, hence, the optimal combination would be very close to the origin.

In length units, the variance of the combined signal is given by Equation (6.6). The variance will be minimized for a triple frequency combined GPS signal if the combination coefficients represent a point in integer space that is close to

1. the ionosphere-free plane $a + b\frac{f_{L1}}{f_{L2}} + c\frac{f_{L1}}{f_{L5}} = 0$
2. the line of maximum noise reduction $\begin{bmatrix} a \\ b \\ c \end{bmatrix} = t \cdot \begin{bmatrix} 154 \\ 120 \\ 115 \end{bmatrix}$

This minimization problem is illustrated in Figure 6.7.

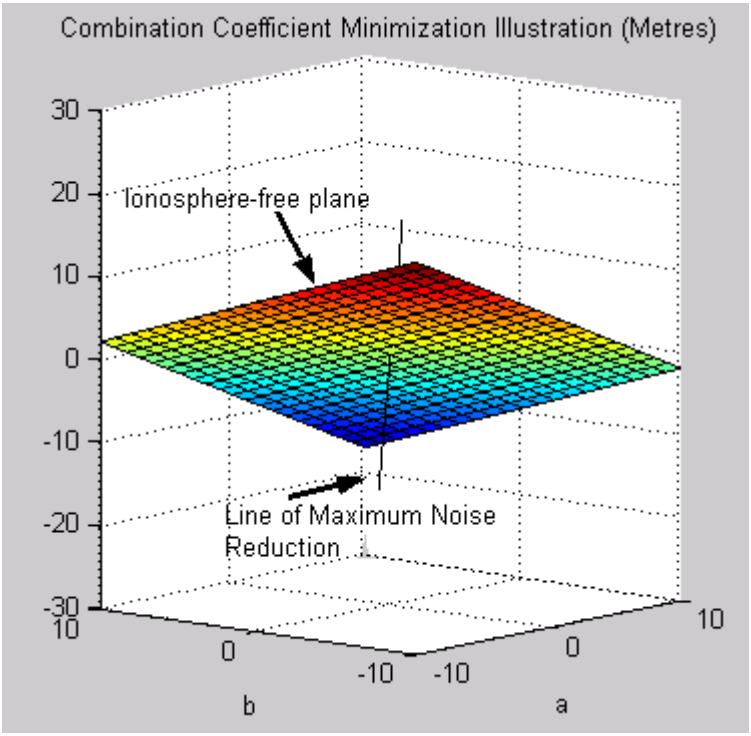

Figure 6.7: Equations Minimizing the Combined Signal Variance in Units of Metres

The angle between the line and the plane for GPS and Galileo frequencies is

$$\theta = 90^\circ - \cos^{-1}\left(\frac{\mathbf{v}_{noise} \bullet \mathbf{n}_{iono}}{|\mathbf{v}_{noise}||\mathbf{n}_{iono}|}\right) = 75.4^\circ \ (GPS) \\ = 75.0^\circ \ (Galileo) \qquad (6.32)$$

where $\mathbf{v}_{noise}$ is the noise reduction line. Since the angle between the ionosphere-free plane and the noise reduction line is large, the two conditions given above are rather contradictory. If a combination is very close to the ionosphere-free plane, it will be far

away from the line of maximum noise reduction. Alternatively, if a combination is close to the line of maximum noise reduction, it will be further away from the ionosphere-free plane. This is supported by the well known fact that ionosphere-free combinations are characterized by increased noise.

6.7 Test Results using Optimal Combinations of Future GNSS Data

A test was conducted to find combinations that were optimal for varying baseline lengths. The average root-mean-square float ambiguity estimation error was computed for all combinations with positive effective wavelengths using integer coefficients in the range of $a,b,c \in [-20,20]$. Combination coefficients with an absolute value greater than 20 were not considered because combinations using such large magnitude coefficients result in large noise amplification factors in units of cycles, causing integer ambiguity resolution to become impossible. Of all the combinations that were tested, the subset of combinations with a float ambiguity estimation error equal to or less than that of the L1 (or E1) untransformed signal were selected. Each combination in the subset was then used to process 100 seconds of kinematic data for baseline lengths of 10, 30 and 60 kilometres in fixed integer mode. The processing was accomplished using the software described in Chapter Three. The combinations that provided the best average position accuracy in fixed ambiguity mode are shown below in Table 6.8 for GPS and Table 6.9

for Galileo. The corresponding noise and ionosphere amplification factors are also shown in the tables.

Table 6.8: Optimal Combinations for GPS

Baseline Length	Combination	Wavelength	Noise Amplification Factor (length units)	Ionosphere Amplification Factor (length units)
10	[4 -3 0]	0.1145	9.0469	0.0081
	[4 -2 -1]	0.1123	7.3110	0.0031
	[3 1 -3]	0.1237	8.0223	0.0299
	[4 0 -3]	0.1081	8.0731	0.0001
	[5 -2 -2]	0.0977	8.6959	0.0158
30	[3 4 -6]	0.1163	22.7809	0.0036
	[5 -8 4]	0.1085	34.1588	0.0026
	[3 5 -7]	0.1140	29.8025	0.0007
	[4 3 -6]	0.1025	17.6864	0.0099
	[3 2 -4]	0.1211	11.7438	0.0179
60	[4 -1 -2]	0.1102	7.0388	0.0005
	[3 6 -8]	0.1119	37.6587	0.0001
	[4 1 -4]	0.1062	10.2739	0.0017
	[2 11 -12]	0.1182	103.7267	0.0009
	[1 16 -16]	0.1252	222.1913	0.0050

Table 6.9: Optimal Combinations for Galileo

Baseline Length	Combination	Wavelength	Noise Amplification Factor (length units)	Ionosphere Amplification Factor (length units)
10	[4 -2 -1]	0.1093	6.9341	0.0001
	[4 0 -3]	0.1119	8.6373	0.0025
	[4 -3 0]	0.1081	8.0731	0.0001
	[7 -7 2]	0.0576	9.3370	0.0051
	[3 -3 1]	0.1247	8.1594	0.0355
30	[4 -1 -2]	0.1106	7.0920	0.0009
	[4 -4 1]	0.1070	10.4245	0.0008
	[4 -3 0]	0.1081	8.0731	0.0001
	[4 -5 2]	0.1058	13.9090	0.0023
	[5 6 -10]	0.1047	48.7025	0.0001
60	[4 0 -3]	0.1119	8.6373	0.0025
	[4 -2 -1]	0.1093	6.9341	0.0001
	[4 -3 0]	0.1081	8.0731	0.0001
	[4 1 -4]	0.1131	11.6669	0.0050
	[4 -4 1]	0.1070	10.4245	0.0008

From the tables it is revealed that the optimal choice of combinations changes as the baseline length varies. However, despite the changing combination coefficients, the optimal combinations in the above tables have similar performance in terms of ambiguity estimation accuracy and position estimation accuracy. Figure 6.8 shows the ambiguity estimation accuracy for the optimal combinations that provide the best position accuracy for each baseline length. The data shown in the following figure corresponds to the shaded rows in Table 6.8 and Table 6.9.

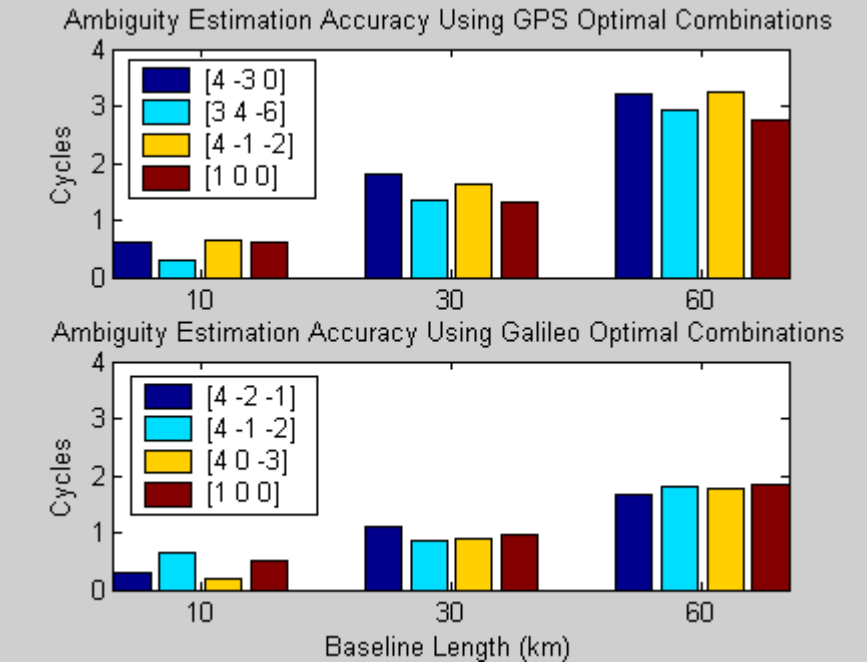

Figure 6.8: Ambiguity Estimation Accuracy Using Optimal Combinations

Figure 6.8 demonstrates that the combined float ambiguities can be estimated with approximately the same precision as the single frequency L1 (or E1) ambiguities, which

are shown as burgundy bars. The benefit of using the combined signals is seen in Figure 6.9 and Figure 6.11 where the fixed position accuracy of the combined signals is shown along with the single frequency precision for both GPS and Galileo. Below each of the position accuracy figures is a set of bar charts illustrating the mean and standard deviation of the position errors. Figure 6.10 gives the mean and standard deviation of the data in Figure 6.9 and Figure 6.12 gives the mean and standard deviation of the data in Figure 6.11.

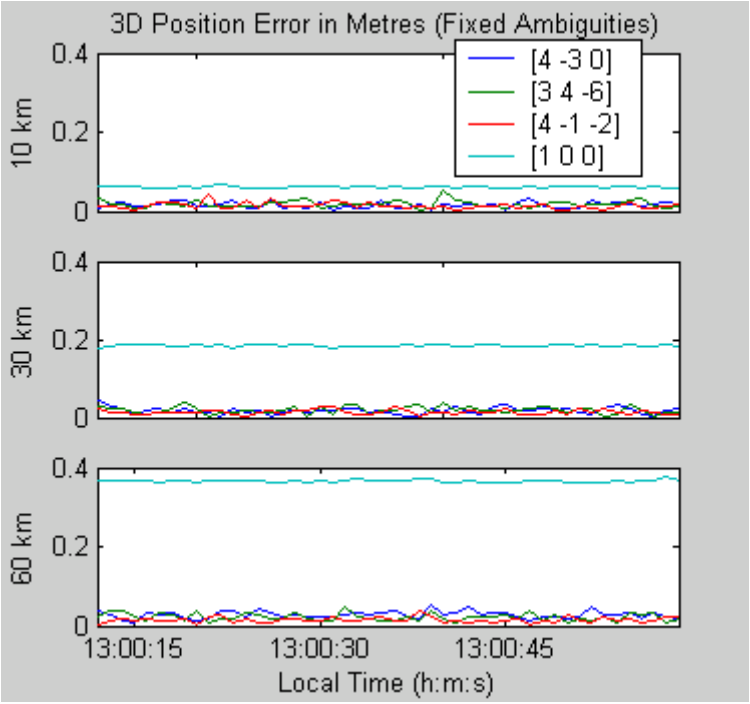

Figure 6.9: Position Error for Optimal GPS Combinations for 10, 30, and 60 km Baseline Lengths

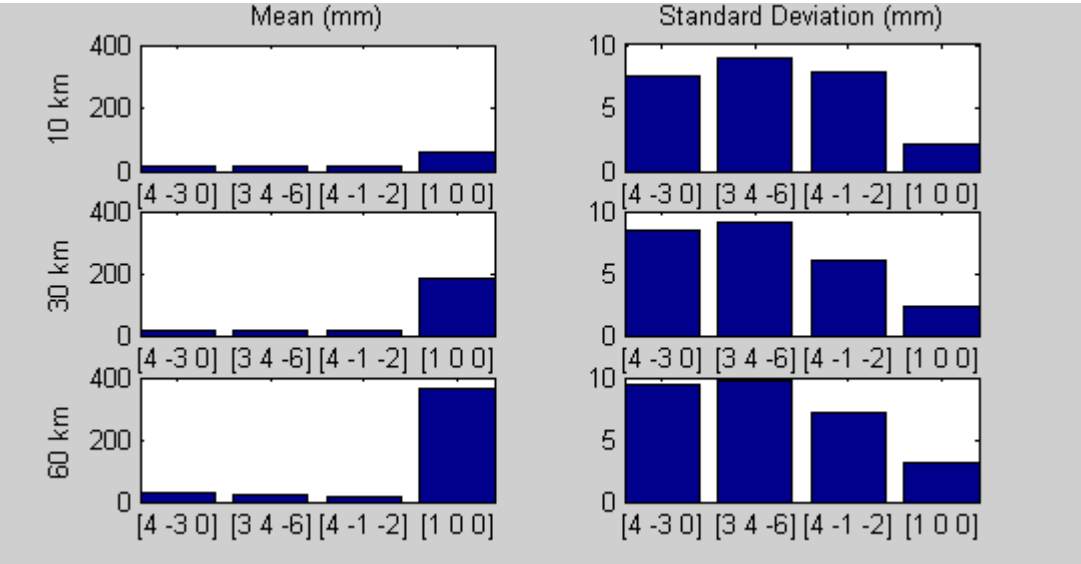

Figure 6.10: Position Error Statistics for Optimal GPS Combinations

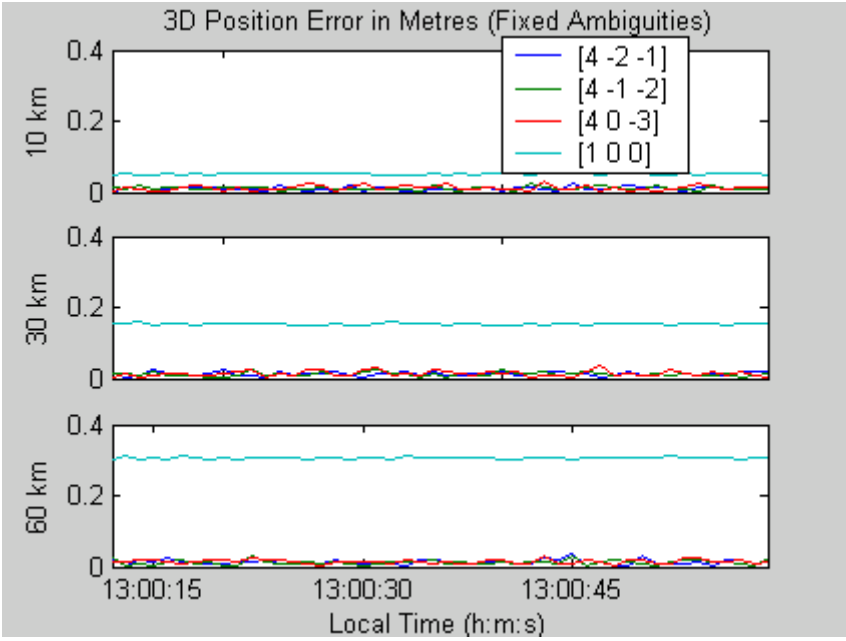

Figure 6.11: Position Error for Optimal Galileo Combinations for 10, 30, and 60 km Baseline Lengths

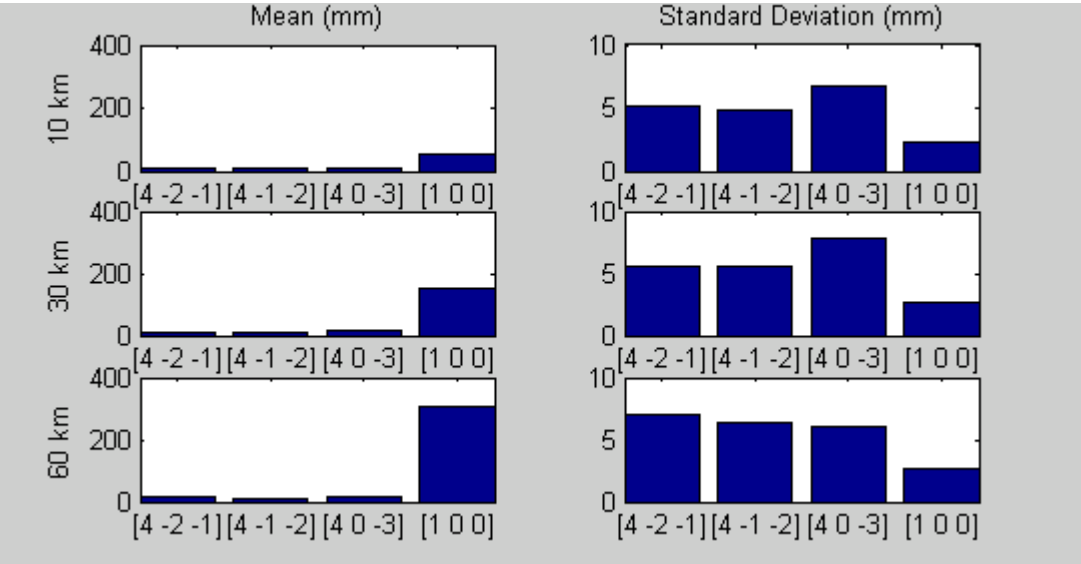

Figure 6.12: Position Error Statistics for Optimal Galileo Combinations

Clearly, the optimally combined signals provide far better position accuracy than the pure L1 and E1 signals – especially for longer baselines. This is because the ionospheric amplification factors for the combined signals are all significantly less than one (see Table 6.8 and Table 6.9). As a result, the impact of the ionosphere is largely eliminated. For the L1 and E1 single frequency measurements, the ionospheric errors directly affect the position solution and cause a bias that increases with increased baseline length. This bias is evident in the mean of the position errors for GPS (Figure 6.10) and Galileo (Figure 6.12). On the other hand, each of the combined signals has a noise amplification factor greater than one. Consequently, the pure L1 and E1 measurements provide the most precise position results in the sense that the standard deviation of the position errors is smaller.

The preceding analysis shows that there are indeed certain combinations of carrier phase measurements that fit the definition of optimality; that is, the combined signals provide better position results when the ambiguities are fixed and the ambiguities are no more difficult to fix than the L1 (or E1) observable. Unfortunately, for longer baselines, successful ambiguity resolution with the optimally combined signals will still be impossible without longer observational time spans. Referring back to Figure 6.8, it is seen that the RMS ambiguity estimation error is approximately one cycle for a 30 km baseline and even greater for a 60 km baseline. This imprecision will prevent successful ambiguity resolution.

6.8 Summary

In this chapter, the mathematical background in using linear combinations was provided and it was shown how to choose combination coefficients in order to mitigate the effects of each individual error source. The concept of optimal linear combinations of carrier phase measurements was introduced and it was established that the choice of an optimal combination depends on the baseline length, the physical error environment and the requirements of the given mission. Test results using optimal combinations were presented and it was shown that combinations exist that allow for ambiguity estimation that is at least as precise as the pure L1 or E1 signals, but that give far better accuracy in

the position domain. However, despite enabling ambiguity estimation that is as precise as the single frequency signals, ambiguity resolution with these optimal combinations is still impossible for long baselines and short observational time spans. This chapter has fulfilled the last minor objective of this thesis which was to explore the benefits of using linear combinations of GNSS data and to test various optimally chosen combinations

Chapter Seven: Conclusions and Recommendations for Future Work

The objectives of this thesis have been met. The techniques and mathematical background for processing GNSS data from multiple systems and on multiple frequencies were explained. The impact that future GNSS measurements will have on the ability to estimate ionospheric delays was shown. A realistic and quantitative analysis of the reliability of ambiguity resolution with future GNSS signals was provided. And the benefits of using linear combinations of GNSS data were elucidated through mathematical theory and experimental testing.

7.1 Key Findings by Chapter

In Chapter One, the current status of the existing Global Navigation Satellite Systems was conveyed. The future plans for GPS modernization and Galileo were explained and some of the integration issues that will arise from using independent systems in an integrated manner were elucidated. A description of the coordinate and time reference frames for GPS and Galileo was provided along with a summary of some research that has already been undertaken to study the benefits of using GPS and Galileo together. Finally, the objectives of the thesis were outlined.

Chapter Two presented mathematical formulae and techniques for processing future GNSS measurements. It was found that there are various ways to deal with the GPS/Galileo Time Offset in the mathematical model and that using homogeneous double differences is a viable option when processing GPS and Galileo measurements together. It was also shown how the stochastic component of the measurement model can be developed when combining different types of measurements from GPS and Galileo together in a single filter. The complete measurement model and dynamic model used throughout this thesis was developed and the Kalman filtering technique was identified as the optimal estimation tool.

Chapter Three presented the GNSS simulation and processing software that has been used to generate and process realistic measurements from modernized GPS and Galileo. The commercially available simulator was explained and the various error sources applied to the simulated measurements were illustrated. The simulator and processor were shown to provide the level of realism required to make experimental tests meaningful.

In Chapter Four, the impact of future signals on ionospheric delay estimation was evaluated. It was found that the ionospheric delays converged more quickly when GPS and Galileo measurements were used together than when GPS was used alone. This result is owing to the fact that the number of visible satellites is increased and the code

pseudorange measurement on the Galileo E5a frequency is more precise than the other code measurements. The faster ionospheric estimation translated directly into faster float ambiguity convergence and faster position state convergence. After convergence, the final position accuracy was approximately the same for all the scenarios tested. This led to the conclusion that the use of triple frequency data will not significantly improve long-term position accuracy when compared with dual-frequency results.

In Chapter Five, the effect of future GNSS signals on ambiguity resolution was assessed. First, it was found that the scenarios that included Galileo measurements were more likely to find the correct ambiguity set. This is again attributed to the more precise Galileo E5a code and the improved satellite geometry which provides fast convergence of the states. Next, the ability to successfully validate potential ambiguity sets was considered. It was discovered that triple frequency scenarios performed better than the corresponding dual frequency scenarios due to the improved redundancy. Finally, the speed of ambiguity resolution was analysed by comparing the various scenarios on a 10 kilometre and an 80 kilometre baseline. It was again observed that the increased number of satellites and the precise Galileo E5a code pseudorange measurement had a great impact and that the scenarios that included Galileo satellites had improved “time to first fix” results.

Chapter Six explored the use of linear combinations of future GNSS data. The benefits and drawbacks of using linear combinations of data were explained from a mathematical standpoint. It was shown that the ionospheric delays could be completely eliminated; whereas, the tropospheric and noise/multipath errors could only be reduced through the use of linear combinations of data. It was also shown that when the effect of one source of error is reduced, the other sources of error are generally amplified. Finally, test results were shown using optimally chosen combinations of future GNSS data. The optimal choice of combination coefficients is highly dependent on the baseline length and the proportion of the various error sources. Selected linear combinations of carrier phase data were shown to provide similar ambiguity estimation precision as the pure L1 or E1 measurements. These same combinations produced far better results in the position domain. However, despite having a similar ambiguity precision as the L1 or E1 signals, the ambiguities of the optimally chosen combinations cannot be reliably fixed to integers for long baselines with short observational time spans.

7.2 Recommendations for Future Work

While this thesis has shed considerable light on what one should expect when future GNSS measurements become available, there are still many unanswered questions around this issue. The following is a list of several topics that the author considers to be of great importance and will require further investigation.

- At the time of writing, the future of the Russian Global Navigation Satellite System (GLONASS) was uncertain. However, recent events have demonstrated that the Russian Federation may be devoting more resources to the afflicted system in an effort to remain in the satellite navigation market. In December 2004, three new satellites were launched to augment the existing constellation. Unfortunately, two of these three satellites have since become unusable leaving a total of 11 operating satellites (GLONASS Website: http://www.glonass-center.ru/frame_e.html). Even with only 11 active satellites, studies have shown that the augmentation of GPS with GLONASS satellites can improve the speed and reliability of ambiguity resolution (Habrich, 1999 and Dai, 2000). If the trend of adding more satellites to the GLONASS constellation continues, there may be motivation to develop systems that integrate GPS, Galileo, and GLONASS. An investigation into the benefits of such a combined system would be very beneficial to developers and users of future GNSS.

- There has been no mention made of the impact that the future GNSS measurements will have on the volume of the integer search space. Particularly when triple frequency measurements from both GPS and Galileo are used, the search volume – or the number of potential ambiguity sets that must be searched – can become very large. This is of particular concern in real-time systems that are limited by processing speed and communication bandwidth. An investigation into the increase of the search space must

be undertaken and innovative strategies to mitigate the processing time should be proposed.

- As a corollary to the first recommendation, the impact of future GNSS signals on partial fixing of the ambiguity set could be investigated. It is likely that the increased size of the ambiguity set when using triple frequency data from both GPS and Galileo will enhance the usefulness of partial fixing. Future work should include an investigation into how the baseline estimates are improved by fixing only a subset of ambiguities with future signals.

- The work undertaken in this thesis is applicable for the new age of GNSS: when GPS has been modernized and Galileo is fully operational. There will be a large period of time in between now and when these systems are fully operational. This transitional phase will be characterized by an incomplete constellation of Galileo satellites and a mixed constellation of GPS satellites that will include satellite vehicles from Blocks II-R, II-RM, and IIF. The length of this transitional time period could extend for over a decade and therefore it merits a focussed investigation to show the transition in performance that will be available as the constellations grow and change. A study of this nature would shed light on when it might become worthwhile investing in receivers that are able to exploit all the future measurements.

- With regard to linear combinations of data, there is an open problem relating to how to choose an optimal combination in a simple and automated way. In general, users of GNSS technology do not know and do not want to be burdened with knowledge about the error environment in which they are receiving signals. Therefore, a major challenge is to determine with a minimum of effort what error sources are affecting the range measurements in a given positioning campaign. This information can then be used to choose an optimal combination of data that will provide the highest accuracy and utmost reliability in any situation.

- Because of the prognostic nature of the work contained in this thesis, future studies should aim to validate the results and provide a more accurate prediction of what the future of GNSS processing will entail. The next step in validation would be to use simulated data that has been generated in a hardware simulator and actually received by a functioning multiple GNSS receiver. This type of investigation is already within reach as commercial receivers that are capable of receiving GPS L5 and Galileo signals have already been developed by NovAtel Inc. Of course the final step in the evolution of this research will be a validation study using signals in space in real positioning environments.

References

Alves, P. (2001) "The Effect of Galileo on Carrier Phase Ambiguity Resolution" Proceedings of the Institute of Navigation GPS 2001, Salt Lake City, UT, September 11 – 14, 2001, pp. 2086 – 2095.

Alves, P., G. Lachapelle, M.E. Cannon, J. Park, P. Park (2002) "Use of Self-Contained Ionospheric Modeling to Enhance Long Baseline Multiple Reference Station RTK Positioning" In Proceedings of the Institute of Navigation GPS 2002, Portland, OR, September 24-27, pp. 1388-1399.

Brown, R.G. and P.Y.C. Hwang (1992) "Introduction to Random Signals and Applied Kalman Filtering Second Edition" Published by John Wiley and Sons, Copyright 1992.

Cannon, M. E. (2002) "ENGO 561 Satellite Positioning" Course Notes from Department of Geomatics Engineering, University of Calgary.

Collins, J.P. (1999) "An Overview of GPS Inter-Frequency Carrier Phase Combinations" Unpublished paper accessed on March 5, 2005: http://gauss.gge.unb.ca/papers.pdf/L1L2combinations.collins.pdf.

Collins, J. P., R.B. Langley, J. LaMance (1996) "Limiting Factors in Tropospheric Propagation Delay Error Modelling for GPS Airborne Navigation" Proceedings of the Institute of Navigation 52nd Annual Meeting, Cambridge, Mass., June 19-21. pp. 519-528.

Cross, P. (2003) "Recent and Future Developments in Global Navigation Satellite Systems and their Impact of National Geoinformation Infrastructures" In Proceedings of Geoinformation and Surveying Conference 2003, the Malaysia Institute of Surveyors Congress, Kuching, Sarawak, April 9-10 2003.

Dai, L. (2000) "Dual-Frequency GPS/GLONASS Real-Time Ambiguity Resolution for Medium-Range Kinematic Positioning" In Proceedings of the Institute of Navigation GPS 2000, Salt Lake City, Utah, September 19-22, 2000.

De Jonge, P. and C. Tiberius (1996) "The LAMBDA Method for Integer Ambiguity Estimation: Implementation Aspects" *Delft Geodetic Computing Centre LGR Series No. 12.*

Directorate-General for Energy and Transport (2003) "Business in Satellite Navigation" Brochure from the Galileo Joint Undertaking, the European Commission, and the European Space Agency, Published May 2003, Accessed Nov. 27, 2004. http://europa.eu.int/comm/dgs/energy_transport/galileo/doc/business_in_satnav.pdf

Ehm, H. (2004) "Galileo: the new European Satellite Navigation System" Presentation for the Institute of Electronics Engineering, Friedrich-Alexander University Erlangen-Nuremberg.

El-Rabbany, A. E-S. (1994) "The Effect of Physical Correlations on the Ambiguity Resolution and Accuracy Estimation in GPS Differential Positioning" Ph.D. dissertation, Department of Geodesy and Geomatics Engineering Technical Report No. 170, University of New Brunswick, Fredericton, New Brunswick, Canada, 161 pp.

European Commission (2004) "GALILEO and GPS will navigate side by side: EU and US sign final agreement" European Commission Website: External Relations, June 28, 2004. http://europa.eu.int/comm/external_relations/us/news/ip04_805.htm.

European Space Agency (2004) "Galileo Moves Forward" European Space Agency Internet news article, July 19, 2004, accessed Nov. 19, 2004 http://www.esa.int/esaNA/SEMW86M26WD_galileo_0.html.

Fontana, R., W. Cheung, T. Stansell (2001) "The Modernized L2 Civil Signal – Leaping Forward in the 21st Century" GPS World Magazine, September 2001.

Global Positioning System (2001) by Pratap Misra and Per Enge, Published by Ganga-Jamuna Press.

Goad, C. C. and L. Goodman (1974) "A modified Hopfield tropospheric refraction correction model" Presented at the Fall Annual Meeting of the American Geophysical Union, San Francisco, December 1974.

"Galileo Mission High Level Document Issue 3.0" Prepared by the Galileo Interim Support Structure (GISS), Sept. 23, 2002.

"Galileo Mission Requirements Document Issue 5.0 - Draft" (2002) Prepared by the European Commission and the European Space Agency, July 25, 2002.

Habrich, H. (1999) "Geodetic Applications of the Global Navigation Satellite System (GLONASS) and of GLONASS/GPS Combinations" Ph.D. Dissertation, University of Bern.

Hatch, R., J. Jung, P. Enge, B. Pervan (2000) "Civilian GPS: The Benefits of Three Frequencies" GPS Solutions 3(4), pp. 1-9.

Han, S., C. Rizos (1995) "Standardization of the Variance-Covariance Matrix for GPS Rapid Static Positioning" Geomatics Research Australasia, No. 62, June 1995, pp. 37-54.

Hein, G., J. Godet, J.-L. Issler, J.-C. Martin, P. Erhard, R. Lucas-Rodriguez, T. Pratt (2002) "Status of Galileo Frequency and Signal Design" Proceedings of the Institute of Navigation GPS 2002, Portland Oregon, September 24 – 27, 2002.

Hofmann-Wellenhof, B., H. Lichtenegger, J. Collins, "GPS Theory and Practice Fifth Edition", Published by Springer Wien, New York, 2000.

Hothem, L. (2004) "GNSS Modernization Program and GPS Policies" Presentation at the Antarctic Remote Observatory Meeting, Boulder, CO, September 19-20, 2004.

Ifadis, I.M. (2000) "A new approach to mapping the atmospheric effects for GPS observations" *Earth Planets and Space*, 52(10), 703-708.

Joosten, P. and C. Tiberius (2000) Fixing the Ambiguities: Are You Sure They're Right?, *GPS World,* May Vol. 11, No. 5, pp. 46-51.

Julien, O., P. Alves, M. E. Cannon, G. Lachapelle (2004) "Improved Triple-Frequency GPS/GALILEO Carrier Phase Ambiguity Resolution Using a Stochastic Ionosphere Modeling" Proceedings of the Institute of Navigation National Technical Meeting, San Diego, CA, January 26 – 28, 2004.

Julien, O., P. Alves, M. E. Cannon, W. Zhang (2003) "A Tightly Coupled GPS/Galileo Combination for Improved Ambiguity Resolution" In Proceedings of the European Navigation Conference GNSS2003, Graz, Austria, April 22-25.

Jung, J. (1999) "High Integrity Carrier Phase Navigation for Future LAAS Using Multiple Civilian GPS Signals." In Proceedings of the Institute of Navigation GPS 1999 Conference. Nashville, Tennessee, September 14-17.

Jung, J., P. Enge, B. Pervan (2000) "Optimization of Cascade Integer Resolution with Three Civil GPS Frequencies" In Proceedings of the Institute of Navigation GPS 2000 Conference, Salt Lake City, Utah, September 19-22.

Kaplan, E. D. (1996) Editor "Understanding GPS: Principles and Applications", Artech House Publishers, Boston, 1996.

Klobuchar, J. A. (1996) "Ionospheric Effects on GPS" Chapter 12 in *Global Positioning System: Theory and Applications Volume 1*. Edited by Parkinson, B. and J. Spilker Jr. American Institute of Aeronautics and Astronautics, Washington, D.C., 1996.

Lacahapelle G., M. E. Cannon, K. O'Keefe, P. Alves (2001) "Report on the Technical Benefit Analysis of GALILEO for Canada" Report prepared for the Canadian Space Agency by the Department of Geomatics Engineering, University of Calgary.

Landau H., H. J. Euler (1992) On-the-fly ambiguity resolution for precision differential positioning. In Proceedings of the Institute of Navigation GPS Conference, Albuquerque, NM, September 22-24, 1992 pp. 607 – 613.

Lanyi, G. (1984) "Tropospheric Delay Effects in Radio Interferometry" In TDA Progress Report, Volume April-June, pp. 152-159, Pasadena, CA, Jet Propulsion Laboratory.

Liu, G. C. (2001) "Ionosphere Weighted Global Positioning System Carrier Phase Ambiguity Resolution" M.Sc. Thesis, Department of Geomatics Engineering, University of Calgary, Report No. 20155.

Liu, J., P. Alves, M. G. Petovello, G. Macgougan, L. deGroot, M.E. Cannon, G. Lachapelle (2002) "Development and Testing of an Optimal Cascading Scheme to Resolve Multi Frequency Carrier Phase Ambiguities" In Proceedings of the Institute of Navigation GPS 2002 Conference, Portland, Oregon, September 24-27.

McDonald, K. D. (2002) "The Modernization of GPS: Plans, New Capabilities and the Future Relationship to Galileo" Journal of Global Positioning Systems, Vol. 1, No. 1: 1-17.

Niell, A. E. (1996) "Global mapping functions for the atmospheric delay at radio wavelengths" *Journal of Geophysical Research,* 101, pp. 3227–3246.

O'Keefe, K. (2001) "Availability and Reliability Advantages of GPS/Galileo Integration" in Proceedings of the Institute of Navigation GPS 2001, Salt Lake City, UT, Sept. 11 – 14.

Odijk, D. (2002) "Fast precise GPS positioning in the presence of ionospheric delays" PhD Thesis, Mathematical Geodesy and Positioning, Delft University Press, Delft.

Office of Science and Technology Policy (OSTP) (2004) "U.S. Space-Based Positioning, Navigation, and Timing Policy" Policy Released on Dec. 15, 2004 by the Executive Office of the President, USA. http://www.ostp.gov/html/FactSheetSPACE-BASEDPOSITIONINGNAVIGATIONTIMING.pdf.

Parkinson, B. W. and Enge, P. K. (1995) "Differential GPS" Chapter 1 in *Global Positioning System: Theory and Applications Volume II*. Edited by Parkinson, B. and J. Spilker Jr. American Institute of Aeronautics and Astronautics, Washington, D.C., 1996.

Radovanovic, R., G. Fotopoulos, N. El-Sheimy (2001) "On Optimizing GNSS Multi-Frequency Carrier Phase Combinations for Precise Positioning" Presented at the International Association of Geodesy 2001 Scientific Assembly, Budapest, Hungary. Sept. 2-7, 2001.

Radovanovic, R. (2002) "Adjustment of Satellite-Based Ranging Observations for Precise Positioning and Deformation Monitoring" Geomatics Engineering Department, University of Calgary, Ph.D. thesis, UCGE Report No. 20166.

Radovanovic, R. N. El-Sheimy, W.F. Teskey (2004) “Variance-Covariance Modeling of Atmospheric Errors for Satellite-Based Network Positioning” in Navigation: Journal of The Institute of Navigation, Vol. 51, No. 2, Summer 2004.

Richert, T., R. Radovanovic, N. El-Sheimy (2003) “Application of Optimal GNSS Multi-Frequency Carrier Phase Combinations to Kinematic Positioning” In Proceedings of the European Navigation Conference GNSS 2003, Graz, Austria, April 22-25, 2003.

Richert, T. and N. El-Sheimy (2004) “The Impact of Future GNSS on Precise Carrier Phase Positioning” In Proceedings of the Institute of Navigation GNSS 2004. Sept. 21-24, Long Beach, CA.

GLONASS “Global Navigation Satellite System” Russian Federation Ministry of Defence Coordinational Scientific Information Center Website. Accessed March 8, 2005: http://www.glonass-center.ru/frame_e.html.

Saastamoinen, J. (1972) “Atmospheric Correction for the Troposphere and Stratosphere in Radio Ranging of Satellites", AGU monograph 15, 3rd Int. Symp. Use of Artificial Satellites for Geodesy, Washington DC, pp 247-251.

Teunissen, P.J.G., P.J. de Jonge, C. C. J. M. Tiberius (1997) "The least-squares ambiguity decorrelation adjustment: its performance on short GPS baselines and short observation spans." *Journal of Geodesy* Volume 71 pp. 589 – 602.

Teunissen, P.J.G (1998) "GPS Carrier Phase Ambiguity Fixing Concepts" Chapter 8, *GPS for Geodesy 2nd Edition* published by Springer Verlag, pp. 319 – 388.

Teunissen, P. J. G., P. Joosten, C. C. J. M. Tiberius (1999) "Geometry-free Ambiguity Success Rates in Case of Partial Fixing" Proceedings of the Institute of Navigation National Technical Meeting , San Diego, CA, January 25–27, 1999.

Teunissen, P. J. G. (2001) "GNSS Ambiguity Bootstrapping: Theory and Application" Proceedings of the International Symposium on Kinematic Systems in Geodesy, Geomatics, and Navigation (KIS2001), Banff, Canada, June 5-8, 2001, pp. 246-254.

"The AIUB IGS Page" Webpage of the Astronomisches Intitut der Universität Bern. Maintained by Pierre Fridez. Accessed on November 2 ,2004. http://www.cx.unibe.ch/aiub/igs.html.

Tiberius, C., T. Pany, B. Eissfeller, K. de Jong, P. Joosten, S. Verhagen (2002) "Integral GPS-Galileo Ambiguity Resolution" In Proceedings of the European Navigation Conference, GNSS2002, Copenhagen, May 2002.

"Navstar GPS Space Segment / Navigation User Interfaces" Interface Control Document (ICD), Revision 200c, prepared by the United States Coast Guard Navigation Center, revised September, 1997.

Verhagen, S. (2002) "Performance Analysis of GPS, Galileo and Integrated GPS-Galileo" Proceedings of the Institute of Navigation GPS 2002, Portland, OR, September 24-27.

Verhagen, S. (2004) "Integer ambiguity validation: an open problem?" GPS Solutions Volume 8(1) pp. 36 – 43.

Verhagen, S., and P. Joosten (2003) "Algorithms for Design Computations for Integrated GPS – GALILEO" In Proceedings of the European Navigation Conference GNSS2003, Graz, Austria, April 22-25.

Vollath, U., S. Birnbach, H.Landau, J.M. Fraile-Ordoñez, M. Martin-Neira (1998) "Analysis of Three-Carrier Ambiguity Resolution (TCAR) Technique for Precise Relative Positioning in GNSS-2" In Proceedings of the Institute of Navigation GPS 1998 Conference, Nashville, Tennessee, September 15-17.

Wang J., C. Satirapod, C. Rizos (2002) "Stochastic assessment of GPS carrier phase measurements for precise static relative positioning" Journal of Geodesy, Vol. 76, No. 2, February 2002, pp. 95-104.

Wibberley, P. (2004) "An Overview of the Galileo Programme and Galileo's Future Timing Services" Presented at the Time and Frequency User Club Meeting, National Physics Laboratory, Teddington, Middlesex, September 28, 2004.